Review

Rheology of Non-Dilute Emulsions: A Comprehensive Review

Rajinder Pal *

Posted Date: 10 March 2026

doi: 10.20944/preprints202603.0830.v1

Keywords: emulsions; droplets; suspensions; rheology; non-Newtonian; dynamic rheology; viscoelasticity; viscosity; shear-thinning

 doi:10.20944/preprints202603.0830.v1

Review

Rheology of Non-Dilute Emulsions: A Comprehensive Review

Rajinder Pal

Department of Chemical Engineering, University of Waterloo, Waterloo, ON N2L 3G1, Canada; rpal@uwaterloo.ca

Abstract

Non-dilute emulsions are emulsions where the concentration of the droplets is high enough for the neighboring droplets to interact with each other hydrodynamically but is still smaller than the packed bed concentration where the droplets are packed and deformed against each other. Thus, they cover a broad range of droplet concentration. Many emulsions encountered in industrial applications fall under this category. Non-dilute emulsions exhibit rich rheological behavior from a simple Newtonian fluid to a highly non-Newtonian fluid reflecting shear-thinning, shear-thickening, yield stress, viscoelasticity, etc. In this article, the rheology of non-dilute emulsions is reviewed comprehensively. Emulsions of hard-sphere type droplets and deformable droplets, with and without surfactants, are covered. The mathematical models describing the rheological behavior of non-dilute emulsions are discussed. The influences of electric charge and interfacial rheology on the rheological behavior of emulsions are covered in detail. The flocculation of droplets caused by different mechanisms such as depletion and bridging induced by additives and their effect on emulsion rheology are investigated thoroughly. Finally, the dynamic rheology of non-dilute emulsions is discussed covering both pure oil-water interfaces and additive-laden interfaces. The mathematical models describing the dynamic rheological behavior of non-dilute emulsions are described. Based on the existing theoretical and empirical models, it is possible to a priori predict the rheology of non-dilute emulsions. However, serious gaps in the existing knowledge on non-dilute emulsion rheology remain. This review identifies the gaps in existing knowledge and points out future directions in research related to non-dilute emulsion rheology.

Keywords: emulsions; droplets; suspensions; rheology; non-Newtonian; dynamic rheology; viscoelasticity; viscosity; shear-thinning

1. Introduction

In dilute emulsions, the separation between the droplets is large, large enough such that the droplets do not interact with each other. Provided that the deformation of droplets is small (capillary number $\rightarrow 0$), dilute emulsions exhibit Newtonian rheology. The concentration of droplets in dilute emulsions is very small (volume fraction, $\varphi \leq 0.02$). Every droplet could be considered as if it is suspended alone in an infinite body of matrix phase. Consequently, only single-droplet mechanics is needed to develop constitutive rheological laws for dilute emulsions.

Non-dilute emulsions are emulsions where the concentration of the droplets is large enough for the neighboring droplets to experience hydrodynamic interactions with each other. Yet the concentration of droplets in non-dilute emulsions is not high enough to approach or even exceed the maximum packing concentration (φ_{max}) where the droplets just begin to touch each other. When $\varphi > \varphi_{max}$, emulsions are called high internal phase ratio emulsions (HIPREs) [1]. The rheological behavior of HIPREs is controlled by the network of interfacial films rather than by individual droplets. Thus, the concentration of droplets in non-dilute emulsions covers the broad range of $\varphi_o < \varphi < \varphi_{max}$. At $\varphi = \varphi_o$ (typically less than 0.05), the interaction between the neighboring droplets just begins and at φ_{max}, the droplets are jam packed without significant deformation, that

 doi:10.20944/preprints202603.0830.v1

is, the undeformed droplets just touch each other (see Figure 1). In emulsions with $\varphi > \varphi_{max}$, the droplets are no longer spherical (see Figure 1). They are deformed as they are pressed against each other, and the emulsion rheology is controlled by interfacial films. The φ_{max} of undeformed uniform spheres is 0.637 if the packing is random close packing type. For hexagonal close packing of uniform spheres, $\varphi_{max} = 0.7405$. Thus, φ_{max} depends on the microstructure of the emulsion.

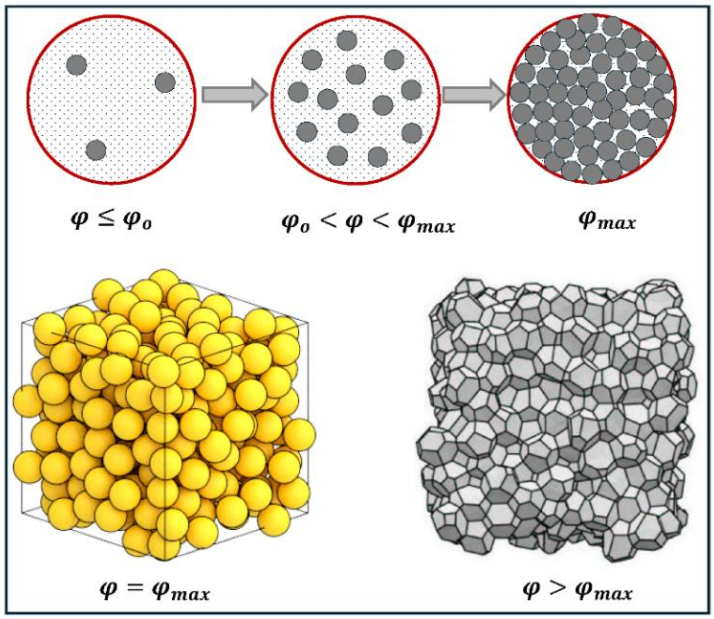

Figure 1. Variation of microstructure of emulsion with increase in φ.

2. Rheology of Non-Dilute Emulsions of Hard-Sphere Type Droplets

In this section, we assume that the droplets of emulsions undergo only hydrodynamic interactions. The non-hydrodynamic interactions are absent. Also, the capillary number is small. Thus, the droplets are more like hard spheres. However, the fluid within the droplets is not stationary as it undergoes internal circulation caused by the transfer of viscous stresses from the external phase to the droplet. Such emulsions are purely viscous in nature without any elastic effects. For dilute non-interacting emulsions, the relative viscosity η_r is given by the celebrated Taylor's equation [2]:

$$\eta_r = 1 + \left(\frac{5\lambda+2}{2\lambda+2}\right)\varphi = 1 + [\eta]\varphi \qquad (1)$$

where $[\eta]$ is intrinsic viscosity which depends on viscosity ratio λ. Note that η_r is defined as the ratio of emulsion viscosity η to matrix viscosity η_c. According to Equation (1), the relative viscosity increases linearly with concentration of droplets for dilute emulsions. However, the non-dilute emulsions exhibit exponential rise in relative viscosity, and they also exhibit non-Newtonian pseudoplastic rheology due to interactions between the droplets.

2.1. Dimensional Considerations

Neglecting any Coulombic and van der Waals interactions, the viscosity of emulsion is expected to be a function of following variables: shear rate ($\dot{\gamma}$), time (t), continuous-phase or matrix viscosity (η_c), dispersed-phase viscosity (η_d), continuous-phase density (ρ_c), dispersed-phase density (ρ_d), droplet radius (R), concentration of particles, that is, number density (n), thermal energy (kT), and interfacial tension (γ). Thus,

$$\eta = f(\dot{\gamma}, t, \eta_c, \eta_d, \rho_c, \rho_d, R, n, kT, \gamma) \qquad (2)$$

As there are 3 basic dimensions involved in expressing all these variables, that is, mass, length, and time, and there are 11 variables, the total number of independent dimensionless groups that can be formed is 11-3=8. The dimensionless groups are: relative viscosity η_r $(= \eta/\eta_c)$, reduced time t_r

 doi:10.20944/preprints202603.0830.v1

$(= t/(\eta_c R^3/kT)$, reduced density ρ_r $(= \rho_d/\rho_c)$, viscosity ratio λ $(= \eta_d/\eta_c)$, volume fraction φ $(= 4\pi nR^3/3)$, Peclet number $N_{Pe} = (\eta_c R^3\dot{\gamma}/kT)$, Capillary number $N_{Ca}(= \eta_c R\dot{\gamma}/\gamma)$, and particle Reynolds number $N_{Re,p}(= \rho_c R^2\dot{\gamma}/\eta_c)$. Thus, the dimensionless form of Equation (2) is:

$$\eta_r = f(t_r, \rho_r, \lambda, \varphi, N_{Pe}, N_{Ca}, N_{Re,p}) \quad (3)$$

Assuming that the droplets are large non-Brownian $(R > 1\ \mu m)$ such that $N_{Pe} \to 0$. The density ratio ρ_r is close to 1. Assuming negligible deformation of droplets, $N_{Ca} \to 0$, and there is steady state $t_r \to \infty$. Thus, Equation (3) simplifies to:

$$\eta_r = f(\lambda, \varphi, N_{Re,p}) \quad (4)$$

2.2. Zero-Shear Viscosity of Emulsions

The zero-shear η_r of emulsions is a function of just two variables: λ and φ as $N_{Re,p} \to 0$.

$$\eta_r = f(\lambda, \varphi) \quad (5)$$

Several authors have derived theoretical models for the viscosity function $f(\lambda, \varphi)$ for non-dilute emulsions. Oldroyd [3] derived the following expression for $f(\lambda, \varphi)$ using the effective medium approach:

$$f(\lambda, \varphi) = \frac{1+\frac{3}{2}\left[\frac{5\lambda+2}{5\lambda+5}\right]\varphi}{1-\left[\frac{5\lambda+2}{5\lambda+5}\right]\varphi} \quad (6)$$

In the Oldroyd approach [3], emulsion is initially considered as a homogeneous effective medium. The unknown rheology of the effective medium is then determined by replacing a small portion of the effective homogeneous medium by the actual components of the emulsion and demanding that if a tiny portion of the effective medium is replaced by the real components of the emulsion, there could be no difference observed in the rheology of emulsion. The Oldroyd model can be expanded as follows:

$$f(\lambda, \varphi) = 1 + \left(\frac{2+5\lambda}{2+2\lambda}\right)\varphi + \frac{(2+5\lambda)^2}{10(1+\lambda)^2}\varphi^2 + \cdots \quad (7)$$

The Oldroyd equation simplifies to the Taylor equation, Equation (1), in the limit $\varphi \to 0$. The Oldroyd model is clearly an improvement over the Taylor model. However, it still severely underestimates the η_r of emulsions when φ is larger than 0.1.

Yaron and Gal-Or [4] and Choi and Schowalter [5] applied the cell model approach to develop the expressions for $f(\lambda, \varphi)$. In the cell model approach, it is envisioned that the droplets of emulsion reside in unit cells of same size subjected to the same flow field. The size of the unit cell is determined from the size (radius) of droplets and their concentration (volume fraction). The Stokes equations are solved determine the velocity, rate of strain, and stress fields within and external to droplets. Yaron and Gal-Or [4] and Choi and Schowalter [5] utilized different boundary conditions at the cell boundary and hence their expressions for $f(\lambda, \varphi)$ are different. Their expressions are as follows:

Yaron and Gal-Or:

$$f(\lambda, \varphi) = 1 + \varphi\left[\frac{5.5\{4\varphi^{7/3}+10-(84/11)\varphi^{2/3}+(4/\lambda)(1-\varphi^{7/3})\}}{10(1-\varphi^{10/3})-25\varphi(1-\varphi^{4/3})+(10/\lambda)(1-\varphi)(1-\varphi^{7/3})}\right] \quad (8)$$

Choi and Schowalter:

$$f(\lambda, \varphi) = 1 + \varphi\left[\frac{2\{(5\lambda+2)-5(\lambda-1)\varphi^{7/3}\}}{4(\lambda+1)-5(5\lambda+2)\varphi+42\lambda\varphi^{5/3}-5(5\lambda-2)\varphi^{7/3}+4(\lambda-1)\varphi^{10/3}}\right] \quad (9)$$

The Choi and Schowalter equation simplifies to Equation (1) in the limit $\varphi \to 0$ whereas the Yaron and Gal-Or equation gives the following erroneous result in the limit $\varphi \to 0$:

$$f(\lambda, \varphi) = 1 + 2.2\left(\frac{2+5\lambda}{2+2\lambda}\right)\varphi \quad (10)$$

Phan-Thien and Pham [6] also developed an equation for non-dilute emulsions by applying the effective medium technique. Their equation is given as:

$$f^{2/5}\left[\frac{2f+5\lambda}{2+5\lambda}\right]^{3/5} = (1-\varphi)^{-1} \quad (11)$$

Unlike the other equations for relative viscosity $f(\lambda, \varphi)$, Equation (11) is not explicit in $f(\lambda, \varphi)$.

 doi:10.20944/preprints202603.0830.v1

2.2.1. Predictions of Zero-Shear Viscosity of Emulsions

Figure 2 compares the η_r versus volume fraction (φ) plots generated from different models at $\lambda = 1$. The η_r increases nonlinearly with the increase in φ. The Oldroyd model, Equation (6), predicts the lowest viscosity whereas the Choi and Schowalter model, Equation (9), predicts the highest viscosity. The order of viscosity prediction from different models is Choi and Schowalter > Yaron and Gal-Or > Phan-Thien and Pham > Oldroyd. The Oldroyd model predicts a finite value even at $\varphi = 1$ whereas other models diverge at $\varphi = 1$. This is unusual as divergence of viscosity is expected at $\varphi = \varphi_{max}$ where $\varphi_{max} \ll 1$. For example, when $\lambda \to \infty$ so that the inclusions are rigid (solid) particles, the viscosity is well known to diverge at the packed bed concentration φ close to 0.64.

Figure 3 compares the model predictions of relative viscosity versus viscosity ratio (λ) at a fixed volume fraction of droplets $\varphi = 0.6$. Interestingly, we see three distinct regions in relative viscosity versus viscosity ratio plots, namely: low viscosity regime for $\lambda < 0.1$ where the viscosity is constant, transition regime for $0.1 < \lambda < 20$ where η_r increases with the increase in λ, and high viscosity regime for $\lambda > 20$ where the η_r becomes constant. Once again, the model predictions are in the following order: Choi and Schowalter > Yaron and Gal-Or > Phan-Thien and Pham > Oldroyd.

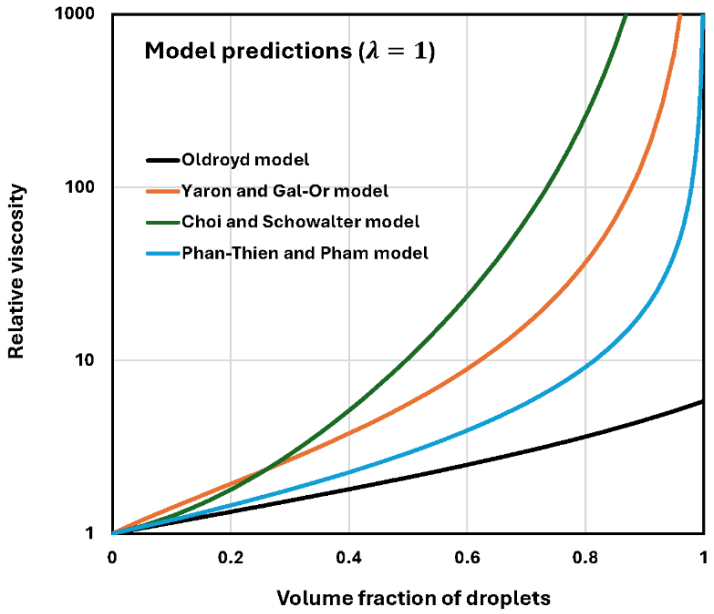

Figure 2. Comparison of relative viscosity versus volume fraction (φ) plots predicted from different models when the viscosity ratio is unity.

 doi:10.20944/preprints202603.0830.v1

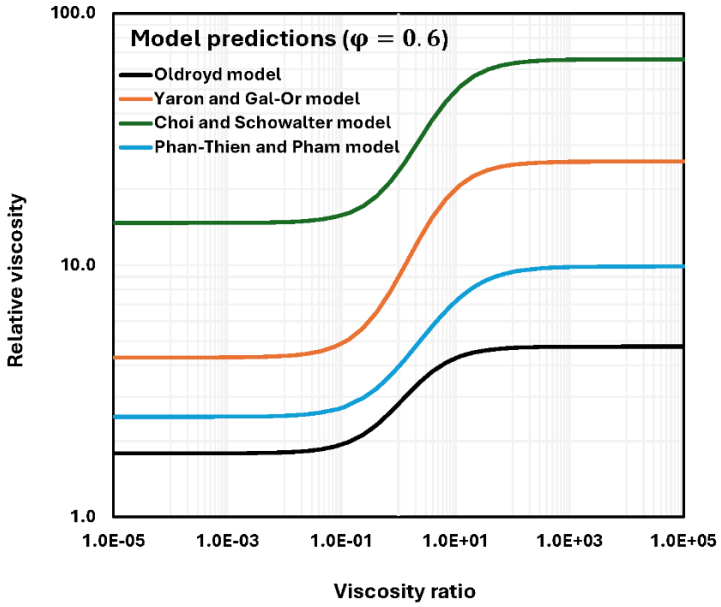

Figure 3. Comparison of η_r versus λ plots predicted from different models ($\varphi = 0.6$).

2.2.2. Comparisons with Experimental Data

Figure 4 compares the flow curves for four different sets of O/W emulsions with different droplet diameters but same φ [7]. The average droplet diameters of emulsions are as follows: Set 1(21.4μm), Set 2 (9.12μm), Set 3 (8.1μm), and Set 4 (4.6μm). The viscosity ratio of all emulsions is also the same, that is, $\lambda \approx 6.2$. Clearly, the droplet size has a large effect on the viscosity of non-dilute emulsions, especially at high value of φ where crowding and jamming of droplets is important.

The zero-shear (low stress of 0.1137 Pa) viscosity data for emulsions is shown in Figure 5 [7]. The data are shown separately for emulsions covering the different ranges of φ, that is, $0.15 \leq \varphi \leq 0.60$ and $0.60 \leq \varphi \leq 0.72$. Interestingly, the data for all emulsions with different average droplet sizes fall on the same curve indicating that the viscosity is independent of droplet size in the volume fraction range of $0 \leq \varphi \leq 0.60$. However, the droplet size effect becomes important in the high φ range of $0.60 \leq \varphi \leq 0.72$ where the viscosity decreases substantially when the average droplet size is increased.

Figure 6 compares the experimental η_r data with theoretical predictions [7]. Although the Oldroyd model (Equation (6)) predictions are not shown, it predicts relative viscosities only slightly larger than the Taylor model (Equation (1)). Clearly, the Taylor and Oldroyd (not shown) models severely underpredict the relative viscosities of emulsions. The model of Yaron and Gal-Or overpredicts the viscosities but the predicted values are close to the experimental data. The Choi and Schowalter model overpredict the η_r substantially within the φ range of $0.30 \leq \varphi \leq 0.60$.

 doi:10.20944/preprints202603.0830.v1

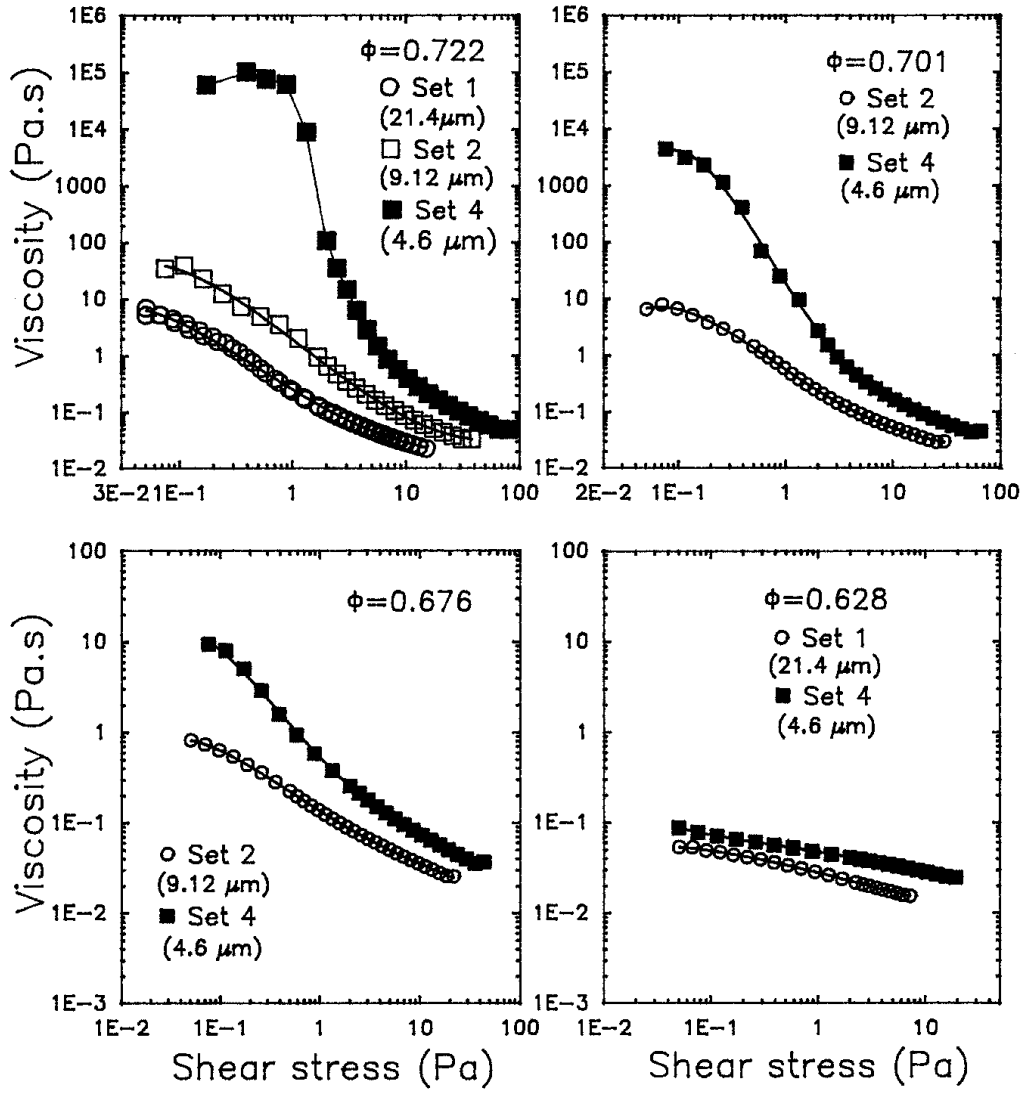

Figure 4. Comparison of flow curves of emulsions of different sets with different droplet diameters at the same φ.

 doi:10.20944/preprints202603.0830.v1

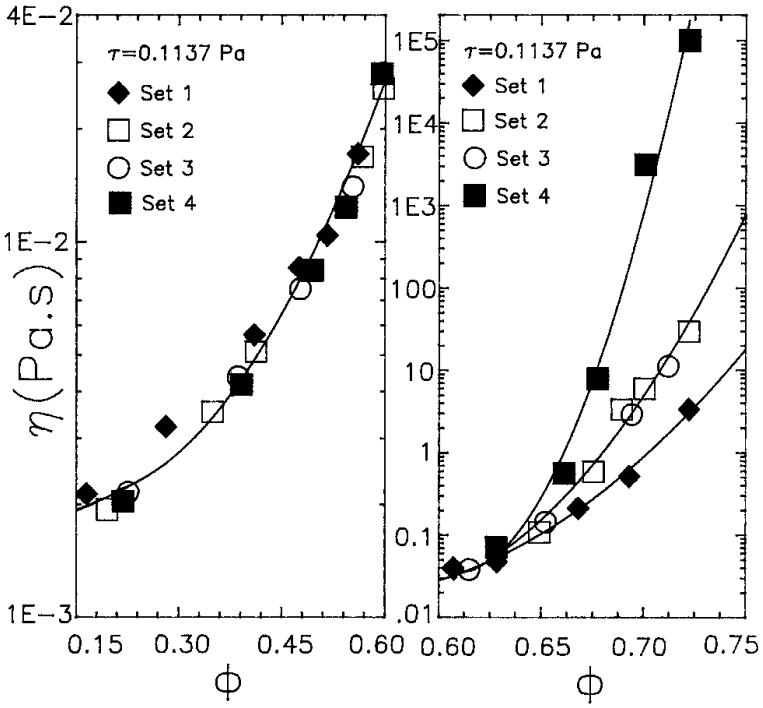

Figure 5. Zero-shear (low shear stress) viscosity versus φ for different sets with different droplet diameters.

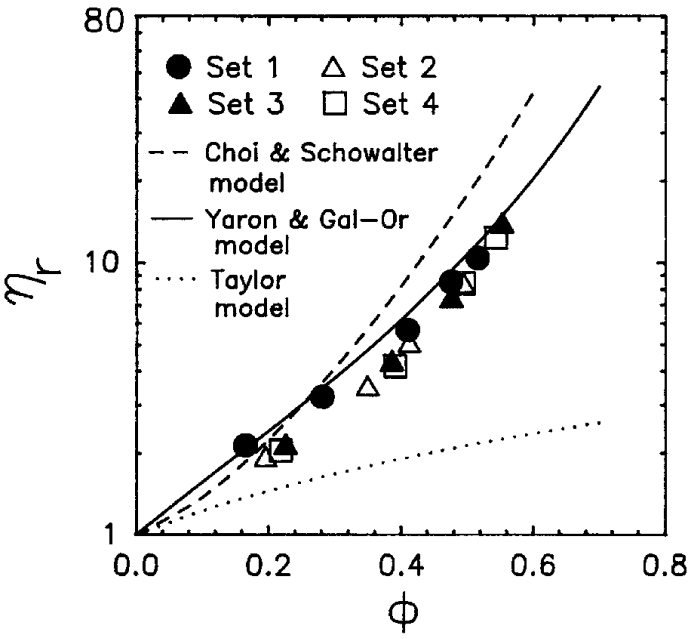

Figure 6. Comparison of experimental η_r data with the predictions of theoretical models.

Figure 7 compares experimental data with the predictions of Equation (11) [8]. The experimental viscosity data for nine sets on O/W and W/O emulsions covering viscosity ratio λ over a broad range of $4 \times 10^{-3} \leq \lambda \leq 1.17 \times 10^{3}$ are compared with the model predictions. Clearly, Equation (11) severely underpredicts the emulsion viscosities.

 doi:10.20944/preprints202603.0830.v1

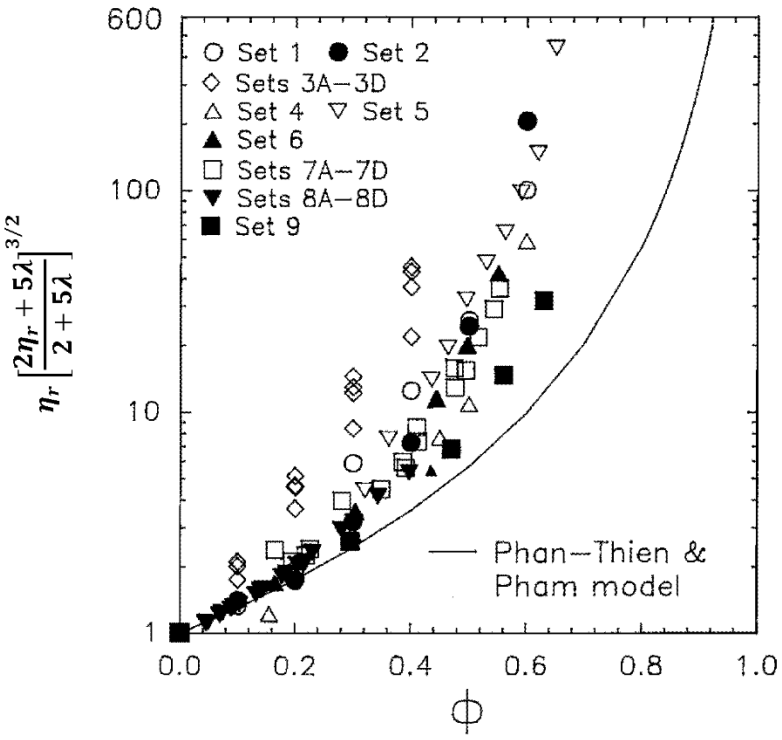

Figure 7. Comparison of experimental viscosity data on emulsions with the predictions of Equation (11).

One serious drawback of the theoretical models is that they do not consider the effects of size and size distribution of droplets on the zero-shear η_r. Also, the models assume that φ of droplets can reach as high as 1 without any divergence in η_r at $\varphi < 1$. This disagrees with experimental observations especially in the case of droplets with $\lambda \to \infty$ where the droplets are rigid (solid) particles. In this case the viscosity is well known to diverge at the packed bed concentration φ close to 0.64. Furthermore, the rate of increase of η_r with φ is predicted to be much lower by the models in comparison with the experimental data. The data shows that the rate of increase in viscosity increases sharply at high φ due to crowding and jamming of droplets. The models of Oldroyd (Equation (6)) and Phan-Thien and Pham (Equation (11)) severely underpredict the viscosities. The Yaron and Gal-Or model (8) describes the experimental data reasonably well only as long as φ is way below φ_{max}, that is, $\varphi < 0.60$. However, at φ values larger than 0.6, both Yaron and Gal-Or model, Equation (8), and Choi and Schowalter model, Equation (9), severely underpredict zero-shear viscosities of emulsions.

Pal [8] reasoned that to overcome the limitations of the literature models which severely underpredict the η_r values especially at high φ, we must incorporate φ_{max} in the models (see Figure 1) to consider the crowding and jamming of droplets at high φ. At $\varphi = \varphi_{max}$, the emulsions develop a significant yield stress and therefore the zero-shear viscosity diverges at $\varphi = \varphi_{max}$. As φ_{max} varies with the droplet size distribution, its incorporation in the models also takes care of the dependence of viscosity on droplet size distribution.

2.2.3. Improved Models for Zero-Shear Viscosity of Non-Dilute Emulsions

Pal [8] has proposed several improved models for the η_r of non-dilute emulsions. He utilized the effective medium technique to derive the following equation for non-dilute emulsions:

$$\frac{d\eta}{d\varphi} = \frac{K_o\eta}{1-K_o\varphi}\left[\frac{\eta+2.5\eta_d}{\eta+\eta_d}\right] \qquad (12)$$

where $K_o = 1/\varphi_{max}$. Upon integration using the condition $\eta = \eta_c$ at $\varphi = 0$, yields the η_r equation for non-dilute emulsions as:

$$\eta_r\left[\frac{2\eta_r+5\lambda}{2+5\lambda}\right]^{3/2} = (1-K_o\varphi)^{-2.5} = \left(1-\frac{\varphi}{\varphi_{max}}\right)^{-2.5} \qquad (13)$$

 doi:10.20944/preprints202603.0830.v1

In the special case of $\lambda \to \infty$ and $K_o = 1/\varphi_{max} = 1$, Equation (13) reduces to the Roscoe-Brinkman [9,10] equation for suspensions of solid particles given as:

$$\eta_r = (1-\phi)^{-2.5} \tag{14}$$

In another development, Pal [11] developed an equation for non-dilute emulsions beginning with Equation (1) and using the effective medium technique along with the crowding of droplets:

$$d\eta = 2.5\eta\left[\frac{0.4\eta+\eta_d}{\eta+\eta_d}\right] d\left(\frac{\varphi}{1-\frac{\phi}{\phi_{max}}}\right) \tag{15}$$

Integration of Equation (16), using the condition $\eta = \eta_c$ at $\varphi = 0$, yields the viscosity equation of non-dilute emulsions as:

$$\eta_r\left[\frac{2\eta_r+5\lambda}{2+5\lambda}\right]^{3/2} = exp\left(\frac{2.5}{1-\frac{\phi}{\phi_{max}}}\right) \tag{16}$$

In the special case of $\lambda \to \infty$ and $\phi_{max} = 1$, Equation (16) reduces to the well-known Mooney [12] equation for suspensions of solid particles given as:

$$\eta_r = exp\left(\frac{2.5}{1-\frac{\phi}{\phi_{max}}}\right) \tag{17}$$

Pal [11] also argued that the differential equation, Equation (15), tends to overcorrect the jamming effect of droplets and proposed the following modified equation:

$$d\eta = 2.5\eta\left[\frac{0.4\eta+\eta_d}{\eta+\eta_d}\right]\frac{d\varphi}{\left(1-\frac{\phi}{\phi_{max}}\right)} \tag{18}$$

Integration of Equation (18), using the condition $\eta = \eta_m$ at $\varphi = 0$, yields the equation for η_r of non-dilute emulsions:

$$\eta_r\left[\frac{2\eta_r+5\lambda}{2+5\lambda}\right]^{3/2} = \left(1-\frac{\phi}{\phi_{max}}\right)^{-2.5\varphi_{max}} \tag{19}$$

In the special case of $\lambda \to \infty$ and $\phi_{max} = 1$, Equation (19) gives the following celebrated Krieger-Dougherty [13] equation for suspensions of solid particles:

$$\eta_r = \left(1-\frac{\phi}{\phi_{max}}\right)^{-2.5\varphi_{max}} \tag{20}$$

Pal [14] further contended that the η_r equations originally developed and proposed for suspensions could also be converted into η_r equations for emulsions if η_r in the suspension equation is replaced with the term $\eta_r[(2\eta_r+5\lambda)/(2+5\lambda)]^{3/2}$. For example, the η_r equation for a suspension can be expressed as:

$$\eta_r = f(\varphi, \varphi_{max}) \tag{21}$$

where $f(\varphi, \varphi_{max})$ is a known function for suspension. This suspension η_r equation with known $f(\varphi, \varphi_{max})$ can be converted into emulsion η_r equation as:

$$\eta_r\left[\frac{2\eta_r+5\lambda}{2+5\lambda}\right]^{3/2} = f(\varphi, \varphi_{max}) \tag{22}$$

Based on this reasoning, Pal [14] has proposed several additional relative viscosity emulsions for non-dilute emulsions. Mendoza and Santamaria-Holek [15] also applied Pal's approach to convert their suspension model for emulsions as follows:

$$\eta_r\left[\frac{2\eta_r+5\lambda}{2+5\lambda}\right]^{3/2} = \left(1-\frac{\varphi}{1-c\varphi}\right)^{-2.5} \text{ where } c = \frac{1-\varphi_m}{\varphi_m} \tag{23}$$

2.2.4. Comparisons with Experimental Data

According to Equation (13), the plot of $(\eta_r)^{-0.4}[(2\eta_r+5\lambda)/(2+5\lambda)]^{-3/5}$ versus φ is expected to be linear with a slope of $-K_o$ and intercept of 1. Figures 8 and 9 show the typical plots of $(\eta_r)^{-0.4}[(2\eta_r+5\lambda)/(2+5\lambda)]^{-3/5}$ versus φ for a variety of emulsions covering λ in the range of $4.15\times10^{-3} \le \lambda \le 29.41$ [8]. As expected from Equation (13), a linear relationship is observed. The slope parameter K_o ranges from 1.184 to 1.466. This corresponds to φ_{max} values of 0.68 to 0.84.

In Figure 10, all the experimental data are plotted as $(\eta_r)[(2\eta_r+5\lambda)/(2+5\lambda)]^{3/2}$ versus $K_o\varphi$. Clearly, Equation (13) describes all the data very well [8].

 doi:10.20944/preprints202603.0830.v1

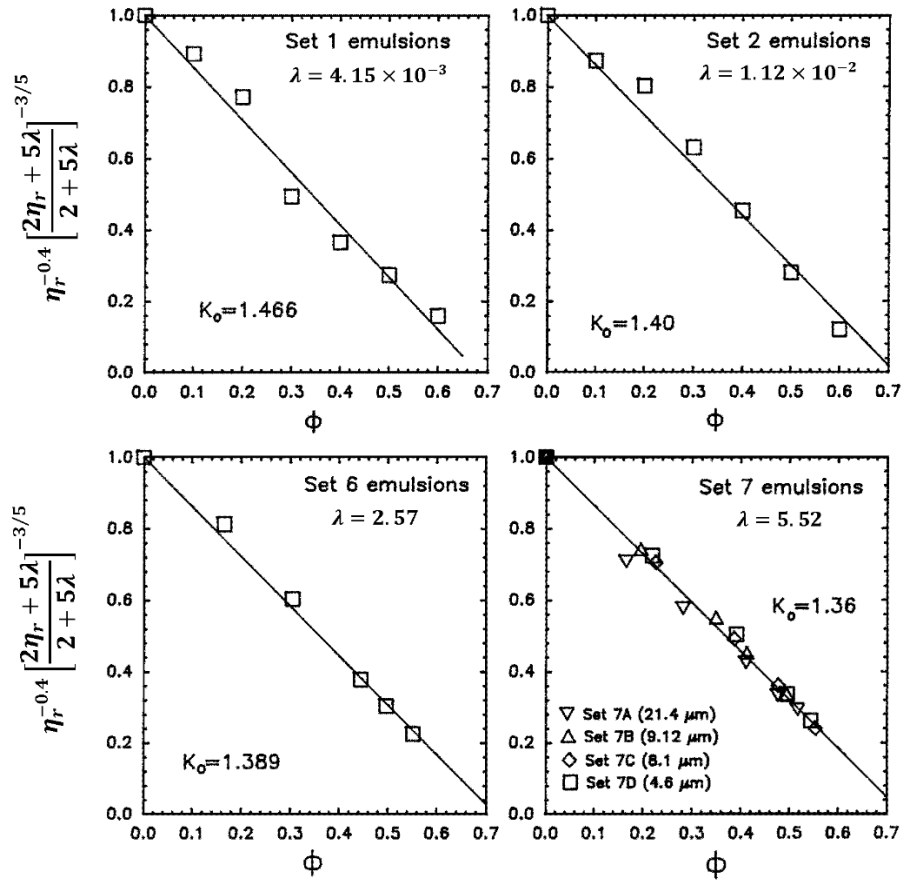

Figure 8. Experimental verification of Equation (13).

 doi:10.20944/preprints202603.0830.v1

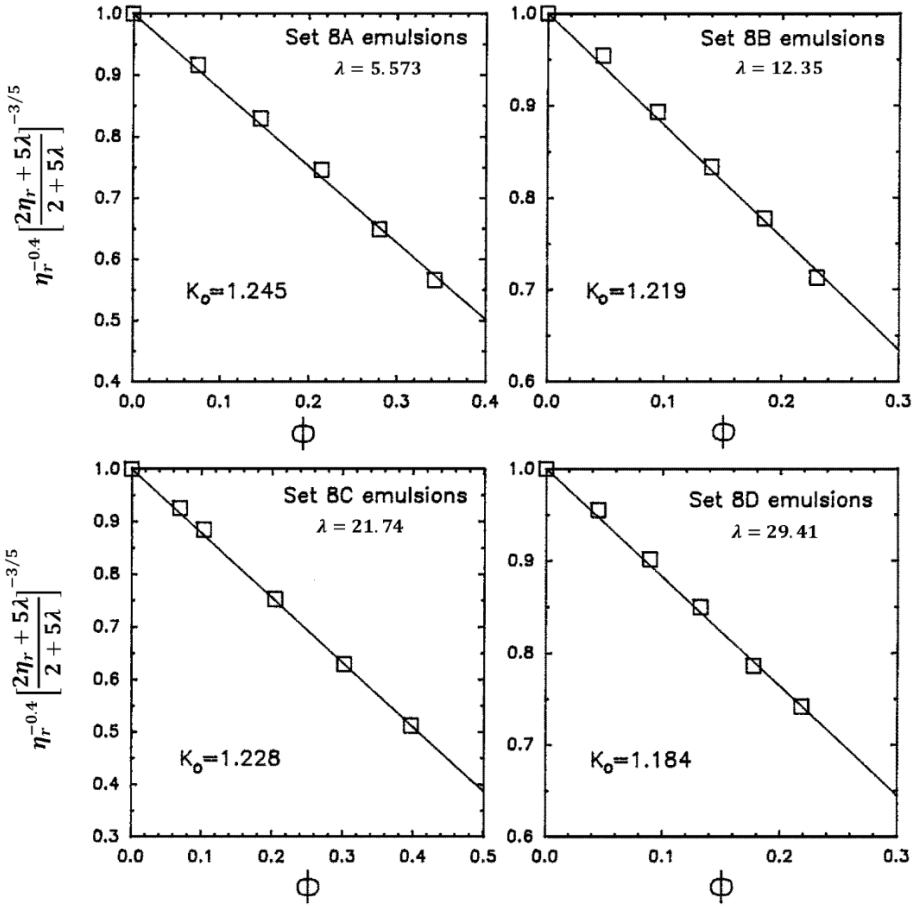

Figure 9. Experimental verification of Equation (13).

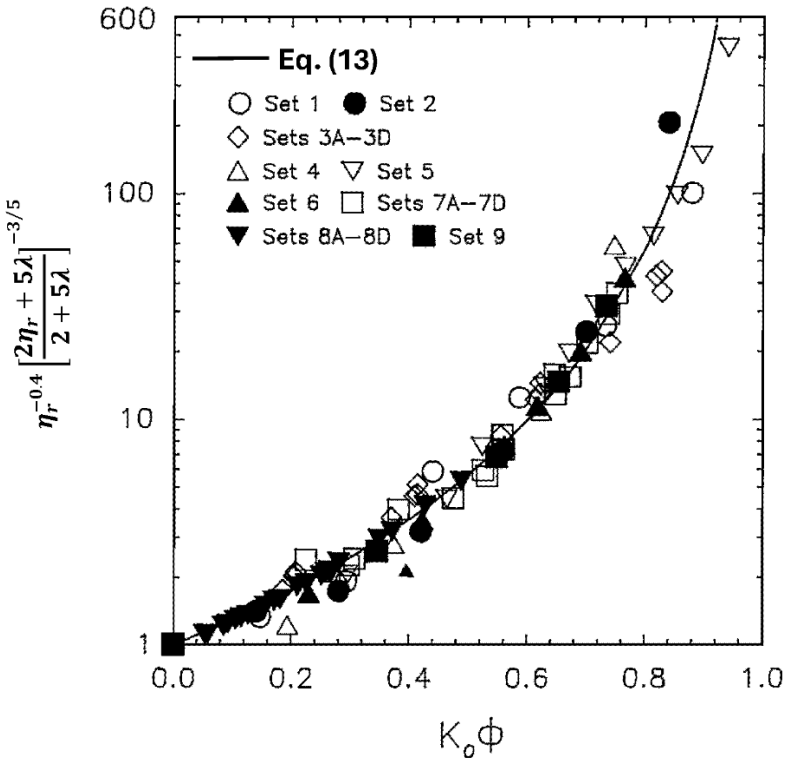

Figure 10. Comparison between nine sets of data with the predictions of Equation (13).

 doi:10.20944/preprints202603.0830.v1

Pal [16] recently collected a large amount of zero-shear (low capillary number) viscosity data of emulsions and evaluated the relative viscosity models. The viscosity ratio range covered was $4.15 \times 10^{-3} \leq \lambda \leq 1.17 \times 10^{3}$. The range of volume fraction of droplets covered was $0 \leq \varphi \leq 0.69$. Figure 11 shows the data of emulsions considered by Pal [16]. The relativity viscosity η_r is plotted as function of φ. A large variation in the viscosity values is observed from one set to another. One reason for spread of relative viscosity at the same φ is that the λ is not the same for all the systems.

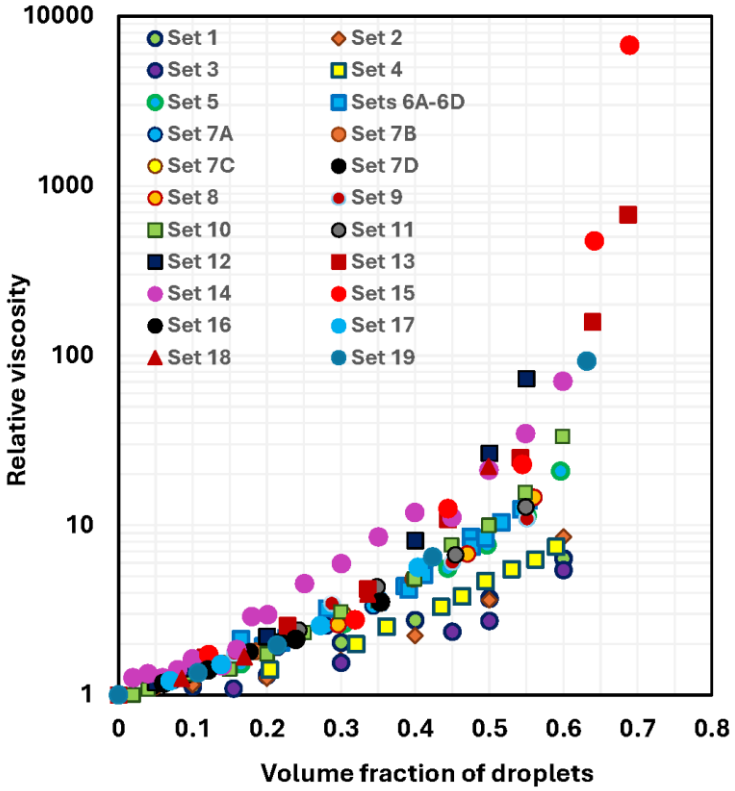

Figure 11. Data of emulsions collected from different sources.

In all the improved zero-shear viscosity models, Equations (13), (16), and (19), φ_{max} is the unknown parameter. Pal [16] estimated the unknown φ_{max} from the experimental data by plotting $(\eta_r)^{-0.4}[(2\eta_r + 5\lambda)/(2 + 5\lambda)]^{-0.6}$ versus φ. The plot is linear that is extended to $(\eta_r)^{-0.4}[(2\eta_r + 5\lambda)/(2 + 5\lambda)]^{-0.6} = 0$ to estimate the φ_{max}. This approach to estimate φ_{max} from the relative viscosity data has been used for suspensions of solid particles by several authors [17,18].

The plot of $(\eta_r)^{-0.4}[(2\eta_r + 5\lambda)/(2 + 5\lambda)]^{-0.6}$ versus φ data is shown on Figure 12 for $\varphi >$ 0.30. As expected, a linear relationship is observed with an estimated φ_{max} value of 0.708. It is well known that $\varphi_{max} = 0.637$ for the random packing of uniform spheres and $\varphi_m = 0.7405$ for hexagonal packing of uniform spheres. Thus, the estimated φ_{max} value for the emulsions falls in between.

 doi:10.20944/preprints202603.0830.v1

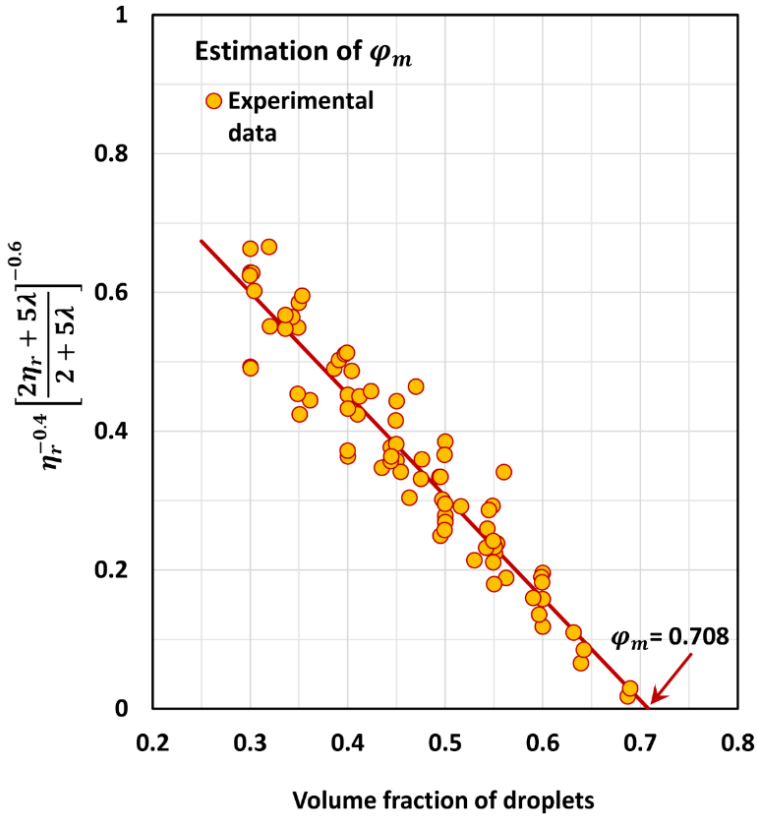

Figure 12. φ_{max} estimation.

Figure 13 compares predictions of Equation (13) with experimental data using the φ_{max} value of 0.708 as estimated in Figure 12. Interestingly, all the experimental viscosity data overlap on to a single curve confirming the validity of scaling the relative viscosity as $(\eta_r)[(2\eta_r + 5\lambda)/(2 + 5\lambda)]^{3/2}$ versus φ basis as suggested by the model, Equation (13). Furthermore, the data shows satisfactory agreement with the predictions of the model. Note that the range of $(\eta_r)[(2\eta_r + 5\lambda)/(2 + 5\lambda)]^{3/2}$ covered in Figure 13 is much wider (1 to 10^5) than compared with the data shown on Figure 10 (1to 600).

 doi:10.20944/preprints202603.0830.v1

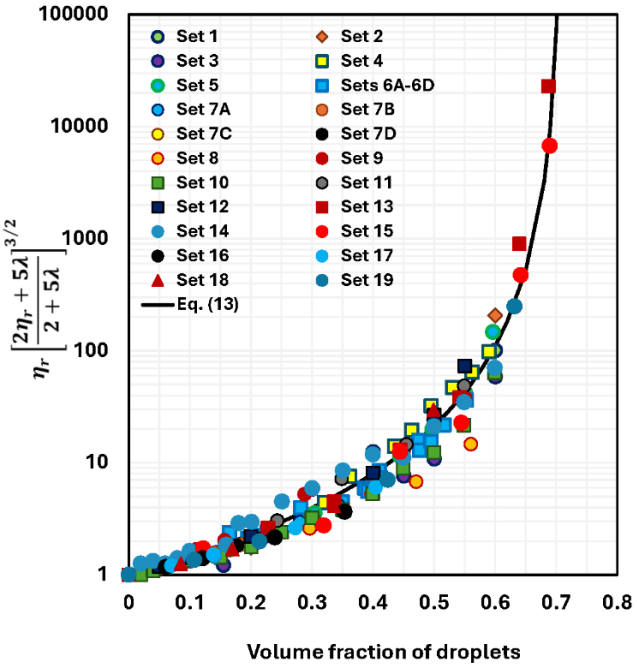

Figure 13. Comparison between data and the model predictions given by Equation (13).

Figures 14–16 compare predictions of Equation (16), Equation (19), and Equation (23) with experimental data emulsions. The φ_{max} value used is 0.708 as determined in Figure 12. Equation (16) overestimates the viscosities severely especially when $\varphi > 0.4$ whereas Equation (19) underestimates the viscosities over the full range of φ. Equation (23) also generally underpredicts the viscosities.

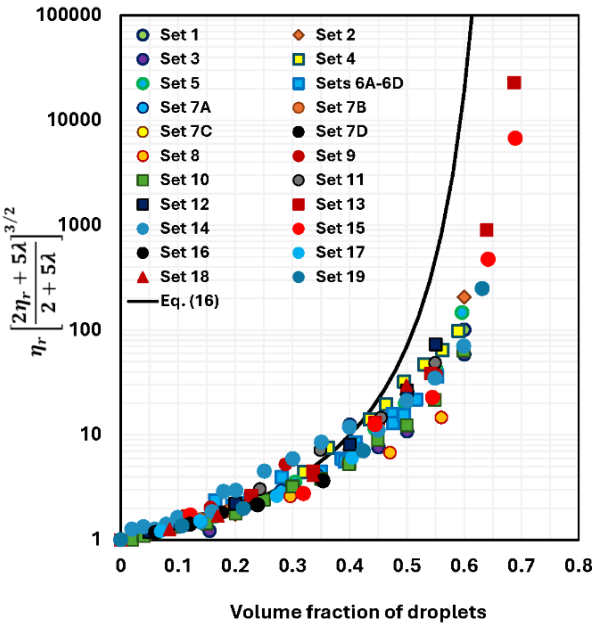

Figure 14. Comparison between data and the model predictions given by Equation (16).

 doi:10.20944/preprints202603.0830.v1

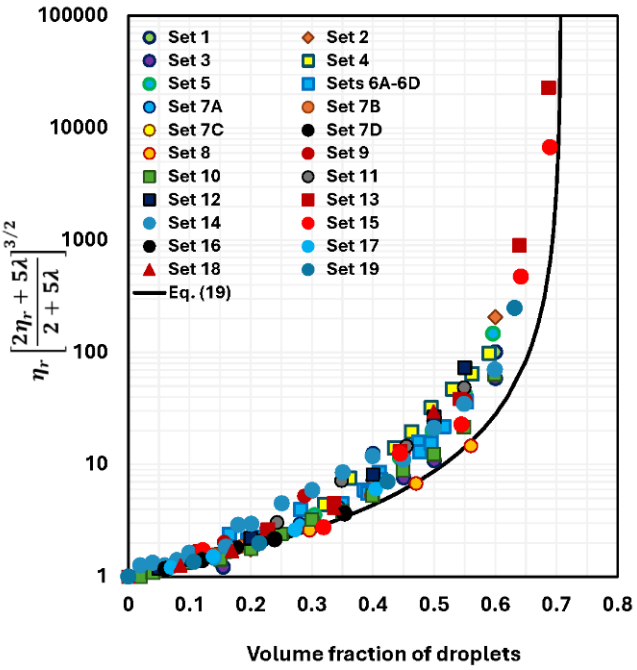

Figure 15. Comparison between data and model predictions given by Equation (19).

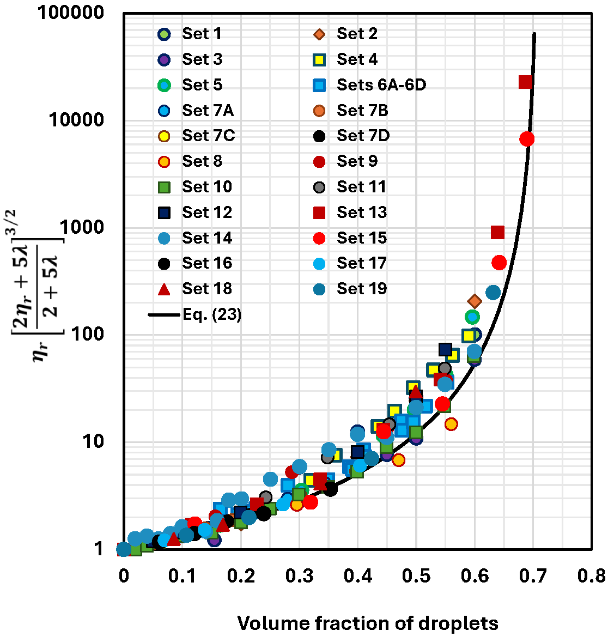

Figure 16. Comparison between data and model predictions given by Equation (23).

The average percentage relative error (APRE) of model prediction is estimated for each model as:

$$APRE = \frac{1}{n}\sum_{i=1}^{i=n}\frac{(y_{exp})_i-(y_{mod})_i}{(y_{exp})_i}\times 100 \qquad (24)$$

where n is the total number of data points and $y = (\eta_r)[(2\eta_r + 5\lambda)/(2 + 5\lambda)]^{3/2}$. The subscripts "exp" and "mod" of y indicate experimental and model values, respectively. The estimated APRE values are as follows: -10.43%, Equation (13) overpredicts to a small degree; -3.9 × 10^{24}%, Equation (16) severely overpredicts; 29.09%, Equation (19) underpredicts substantially; and 20.24%, Equation (23) underpredicts substantially [16].

2.2.5. Best Available Model for Zero-Shear Viscosity of Non-Dilute Emulsions

 doi:10.20944/preprints202603.0830.v1

The models presented in the preceding section (section 2.2.4) are an improvement over the models presented earlier in section 2.2 (Oldroyd, Yaron and Gol-Or, Choi and Schowalter, Phan-Thien and Pham). The improvement in the models is due to the introduction of φ_{max} in the models. However, the APRE (average percentage relative error) is still large.

Pal [16,19] developed another model which is much more accurate compared with other models. The model was developed using the effective medium technique and considering the aggregation of droplets in a flow field caused by collision of neighboring droplets:

$$\eta_r \left[\frac{2\eta_r+5\lambda}{2+5\lambda}\right]^{3/2} = \left(1-\varphi_{eff}\right)^{-2.5} \qquad (25)$$

where

$$\varphi_{eff} = \left\{1+\left[\frac{1-\varphi_{max}}{\varphi_{max}^2}\right]\varphi\right\}\varphi \qquad (26)$$

Figure 17(a) compares predictions of Equation (25) with the data for emulsions. The φ_{max} used is 0.708, same as that used in previous comparisons. The APRE of this model is just 3%, that is, it underpredicts the viscosities slightly.

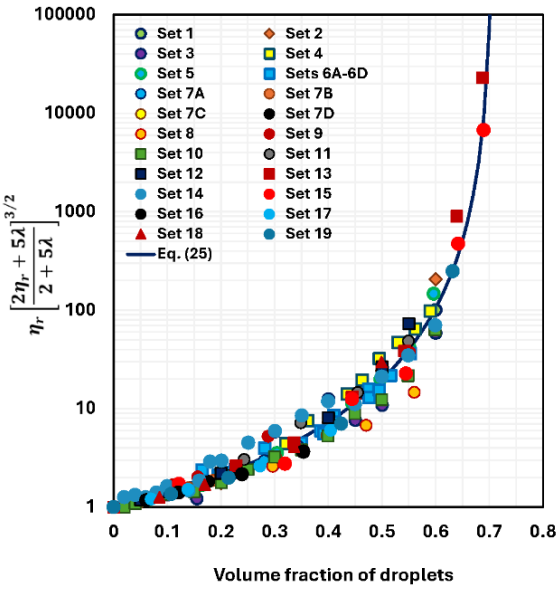

Figure 17. a). Comparison between data and model predictions given by Equation (25).

Figure 17(b) compares the experimental η_r data for emulsions at a fixed φ value of 0.5 with the estimations of Equation (25) [19]. For $\lambda < 10$, the η_r data follows the model (Equation (25)) closely when $\varphi_{max} = 0.637$. For $\lambda > 20$, the η_r data follows the model closely when $\varphi_{max} = 0.7404$. This could mean that the microstructure of emulsions is affected by λ.

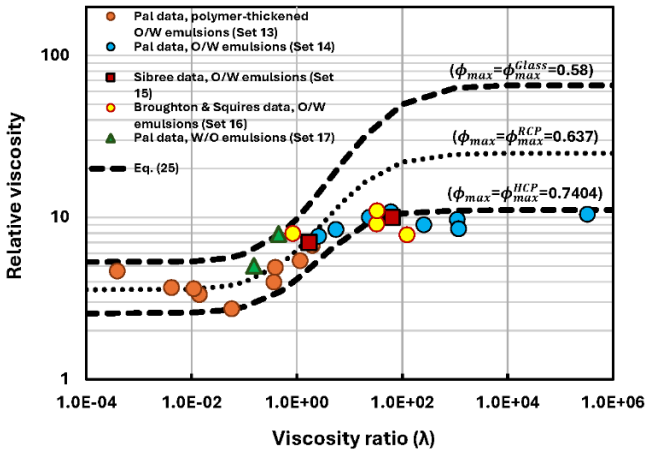

 doi:10.20944/preprints202603.0830.v1

Figure 17. b). Comparison of experimental viscosity and the prediction of Equation (25) at a fixed φ of 0.5 but varying λ.

2.2.6. Effect of Droplet Size and Distribution on Zero-Shear Viscosity of Non-Dilute Emulsions

The droplet size and size distribution have a strong effect on the viscosity of non-dilute emulsions, especially at volume fraction of droplets φ approaching the φ_{max}. For example, the emulsions of Figure 5 showed negligible effect of droplet size when $\varphi \leq 0.60$. However, at higher concentrations corresponding to $\varphi > 0.60$, the viscosity of emulsion increased substantially with the decrease in average droplet size. Figure 18 shows several additional examples where the viscosity of emulsion shows a large increase with the decrease in droplet size [20,21].

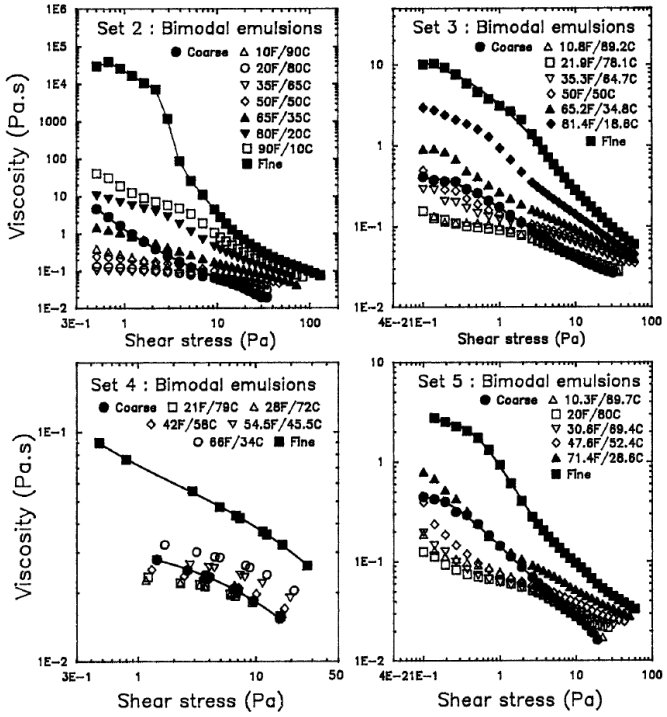

Figure 18. Viscosity plots of bimodal emulsions. Fine and coarse monomodal emulsions are mixed in various proportions at the same φ. The φ values for various sets shown are as follows: Set 2 ($\varphi = 0.745$), Set 3 ($\varphi = 0.71$), Set 4 ($\varphi = 0.63$), and Set 5 ($\varphi = 0.70$).

The fine emulsions in Figure 18 are much more viscous than the coarse emulsions at the same φ. For the emulsions data shown on Figure 18, the droplet size information is given in Table 1.

Table 1. Droplet size information of emulsions of Figure 18.

Set no.	Fine emulsion average droplet diameter	Coarse emulsion average droplet diameter
2	6.3 μm	20 μm
3	9 μm	65 μm
4	6.52 μm	32.3 μm
5	7.4 μm	22 μm

The increase in emulsion viscosity with the decrease in average droplet size could be explained in terms of an increase in hydrodynamic interaction between the droplets. The mean separation distance between the droplets a_m, given by the following equation [22], decreases with the decrease in droplet size:

$$a_m = 6R(1-\varphi)/2\varphi \quad (27)$$

 doi:10.20944/preprints202603.0830.v1

A decrease in the mean separation distance between the droplets with the decrease in droplet size is expected to enhance interaction between the droplets and hence result in an increase in viscosity.

Interestingly, the viscosity of emulsion is also affected strongly by the droplet size distribution. Figure 18 shows the viscosity of bimodal emulsion (mixture of fine and coarse emulsion at same φ) can be much lower than that of either fine or coarse emulsion, especially at low values of shear stress (zero shear rate). The effect of droplet size distribution is more clearly shown on Figure 19. For any given set, the fine emulsion exhibits a much higher viscosity than the coarse emulsion, as expected. However, the bimodal (mixed fine and coarse) emulsion exhibits viscosities even lower than that of the coarse emulsion at low values of fine emulsion content clearly demonstrating the effect of droplet size distribution on emulsion viscosity. Furthermore, the viscosity of the mixed emulsion goes through a minimum value at a certain content of the fine emulsion (around 0.20 to 0.30) [20].

The decrease in viscosity of mixed emulsion upon the addition of fine emulsion to a coarse emulsion can be justified in terms of φ_{max}, the packing volume fraction of droplets. According to the relative viscosity models described in the preceding sections, the higher the φ_{max}, the lower the emulsion viscosity. The φ_{max} is expected to increase with the addition of a fine emulsion to a coarse emulsion as fine emulsion droplets can easily fit into the voids between the large droplets and as a result, one can incorporate a higher concentration of droplets into the emulsion to reach a packed bed structure.

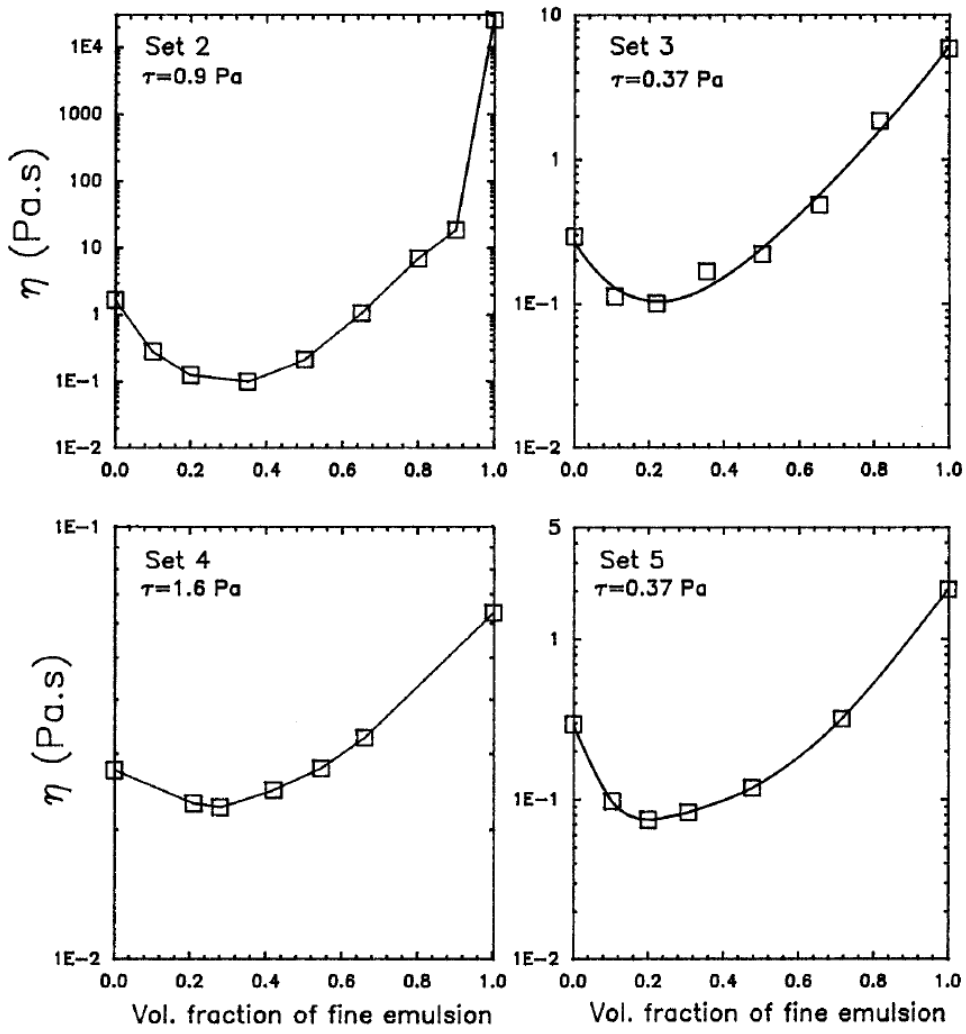

 doi:10.20944/preprints202603.0830.v1

Figure 19. Viscosity versus fine emulsion content of the bimodal emulsion. The data shown on Figure 19 is obtained from Figure 18. The droplet sizes information is given in Table 1. The φ values for various sets shown are as follows: Set 2 ($\varphi = 0.745$), Set 3 ($\varphi = 0.71$), Set 4 ($\varphi = 0.63$), and Set 5 ($\varphi = 0.70$).

Based on the size distribution data, the φ_{max} can be estimated from the analytical model of Ouchiyama and Tanaka [23]. The φ_{max} expression according to the Ouchiyama and Tanaka theory [23] is given as:

$$\varphi_{max} = \frac{\sum D_i^3 f_i}{\sum (D_i \sim \bar{D})^3 f_i + \frac{1}{\beta}\sum[(D_i + \bar{D})^3 - (D_i \sim \bar{D})^3] f_i} \quad (28)$$

where

$$\beta = 1 + \frac{4}{13}(8\varphi_{max}^{o} - 1)\bar{D}\frac{\sum (D_i + \bar{D})^2 [1 - \frac{(3/8)\bar{D}}{(D_i + \bar{D})}] f_i}{\sum [D_i^3 - (D_i \sim \bar{D})^3] f_i} \quad (29)$$

$$\bar{D} = \sum D_i f_i. \quad (30)$$

In Eqs. (28)-(30), φ_{max}^{o} is the φ_{max} of monodisperse emulsion, f_i is the number fraction of droplets of diameter D_i, $\bar{D}$ is the number-average diameter of the emulsion, and the abbreviation $(D_i \sim \bar{D})$ is defined as:

$$(D_i \sim \bar{D}) = 0 \quad \text{for} \quad D_i \leq \bar{D}, \quad (31)$$

$$= D_i - \bar{D} \quad \text{for} \quad D_i > \bar{D} \quad (32)$$

Figure 20 shows the plots of φ_{max} for bimodal emulsions as a function of volume fraction of fine emulsions. In calculating the values of φ_{max} from the Ouchiyama and Tanaka theory, Equations (28)-(30), the value of φ_{max}^{o} was taken as 0.74. The plots of φ_{max} versus volume fraction of fine emulsion exhibit a maximum value at a certain content of the fine emulsion. Interestingly, the maximum in φ_{max} occurs almost at the volume fraction of the fine emulsion where a minimum in viscosity is observed (see Figure 19). Also note that the value of φ_{max} increases with the decrease in d/D, the ratio of fine emulsion to coarse emulsion diameters.

 doi:10.20944/preprints202603.0830.v1

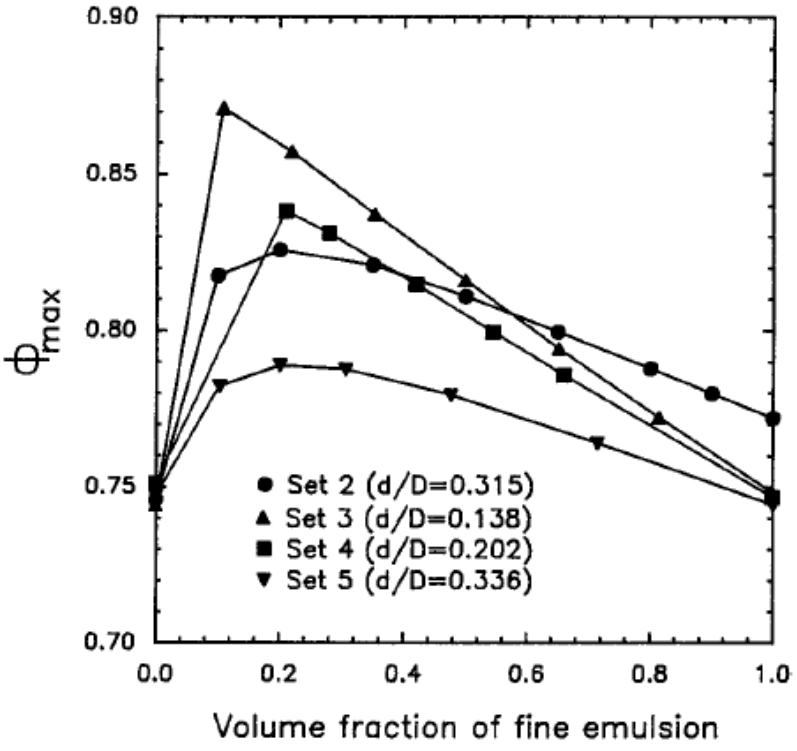

Figure 20. Variation of φ_{max} with fine emulsion content of bimodal emulsions, as predicted by the Ouchiyama and Tanaka theory.

The improved emulsion viscosity models involving φ_{max} (for example, Equation (25)) and discussed in the preceding sections could be used to predict the viscosities of multimodal emulsions. For simplicity, we will consider emulsions with $\lambda = 0$. We utilize the model expressed in Equation (25) to determine the influence of droplet size modality on η_r. When $\lambda \to 0$, the model becomes:

$$\eta_r = \left[1 - \left\{1 + \left(\frac{1-\varphi_{max}}{\varphi_{max}}\right)\left(\sqrt{1 - \left(\frac{\varphi_{max}-\varphi}{\varphi_{max}}\right)^2}\right)\right\}\varphi\right]^{-1} \qquad (33)$$

Consider a bimodal emulsion composed of two fractions of droplets: coarse droplet fraction and fine droplet fraction (see Figure 21). Let φ_1 be the concentration of fine droplets in the mixture of fine droplets and dispersion medium (excluding large droplets), φ_2 be the concentration of large droplets in the overall emulsion, and φ_T be the total concentration of all droplets in the emulsion. Thus,

$$\varphi_1 = \frac{V_1}{V_L + V_1} \; ; \; \varphi_2 = \frac{V_2}{V_L+V_1+V_2}; \; \varphi_T = \frac{V_1+V_2}{V_L + V_1 + V_2} \qquad (34)$$

where V_L, V_1, and V_2 are the volumes of the dispersion medium (matrix liquid), fine droplets, and large droplets, respectively in the whole emulsion.

 doi:10.20944/preprints202603.0830.v1

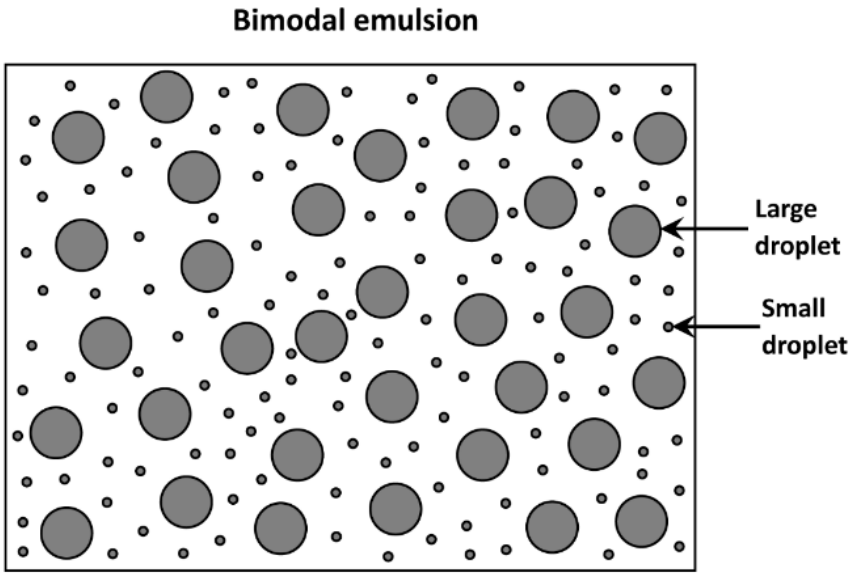

Figure 21. Bimodal emulsion.

If the fine-droplets are assumed to be very small in comparison with the large droplets, the fine-droplet fraction can be treated as a homogeneous phase with respect to the large droplets. Thus,

$$\frac{\eta_{overall-emulsion}}{\eta_{fine-emulsion}} = f(\varphi_2) \quad (35)$$

$$\frac{\eta_{fine-emulsion}}{\eta_c} = f(\varphi_1) \quad (36)$$

where $\eta_{overall-emulsion}$ is the overall viscosity, $\eta_{fine-emulsion}$ is the viscosity of the fine emulsion fraction, η_c is the continuous phase viscosity, and $f(\varphi)$ is the function given by Equation (25). Using Equations (35) and (36), the η_r of the whole emulsion can be expressed as [16]:

$$\eta_r = \frac{\eta_{overall-emulsion}}{\eta_c} = \frac{\eta_{overall-emulsion}}{\eta_{fine-emulsion}} \times \frac{\eta_{fine-emulsion}}{\eta_c} = f(\varphi_1)\, f(\varphi_2) \quad (37)$$

Combining Equations (33) and (37), we obtain:

$$\eta_r = \left[1 - \left\{1 + \left(\frac{1-\varphi_{max}}{\varphi_{max}}\right)\left(\sqrt{1 - \left(\frac{\varphi_{max}-\varphi_1}{\varphi_{max}}\right)^2}\right)\right\}\varphi_1\right]^{-1}\left[1 - \left\{1 + \left(\sqrt{1 - \left(\frac{\varphi_{max}-\varphi_2}{\varphi_{max}}\right)^2}\right)\right\}\varphi_2\right]^{-1} \quad (38)$$

The unknown volume fractions φ_1 and φ_2 can be calculated if we know the values of φ_T and fraction f_c of coarse droplets as follows:

$$\varphi_2 = f_c \varphi_T \quad (39)$$

$$\varphi_1 = \frac{\varphi_T - \varphi_2}{1-\varphi_2} \quad (40)$$

Note that:

$$f_c = \frac{V_2}{V_1+V_2};\ f_f = 1 - f_c = \frac{V_1}{V_1+V_2} \quad (41)$$

Figure 22 shows η_r of bimodal emulsions as function of f_f at various values of φ_T. The φ_{max} value used was 0.7405, that is, hexagonal close packing concentration.

 doi:10.20944/preprints202603.0830.v1

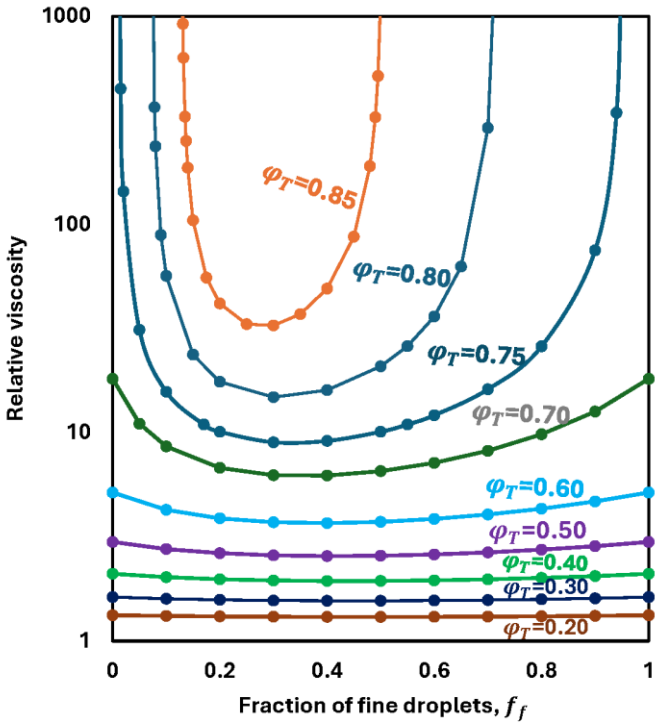

Figure 22. η_r of bimodal emulsions as function of f_f for different values of φ_T.

According to Figure 22, a large drop in η_r is observed upon the conversion of a monomodal emulsion to a bimodal emulsion keeping φ_T constant. The effect of size modality is large when $\varphi_T >$ 0.70. Furthermore, the η_r of a mixed emulsion shows a minimum at some content of fine droplets f_f, as observed experimentally in Figure 19. In Figure 19, it was observed that the viscosity of the mixed emulsion experiences a minimum value around a fine emulsion proportion around 0.20 to 0.30. The model predictions (Figure 22) also exhibit minimum around a fine emulsion proportion of 0.30.

2.3. Effect of Reynolds Number on Emulsion Viscosity

The discussion so far was restricted to zero-shear viscosity of non-dilute emulsions. Thus, the non-Newtonian behavior of emulsion was not considered. Non-dilute emulsions generally exhibit pseudoplastic behavior caused by clustering and break-up of clusters even when $N_{Ca} \to 0$ and there is negligible deformation of droplets. In shear flow, the droplets undergo frequent collisions and form aggregates (see Figure 23) which translate and rotate with emulsion flow (see Figure 24) [7,24–27]. The size of the clusters is related to the Reynolds number defined as:

$$N_{Re,p} = \rho_c \dot{\gamma} R^2 / \eta_c \quad (42)$$

where ρ_c, R, and η_c are matrix density, droplet radius, and matrix viscosity, respectively. The average cluster size decreases with the increase in $N_{Re,p}$, resulting in a decrease in the emulsion viscosity.

 doi:10.20944/preprints202603.0830.v1

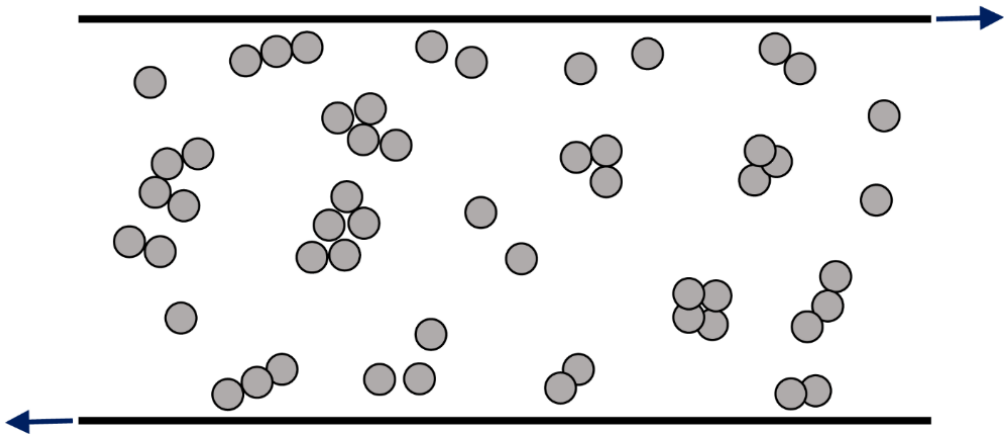

Figure 23. Flocculation of droplets in flow of emulsion.

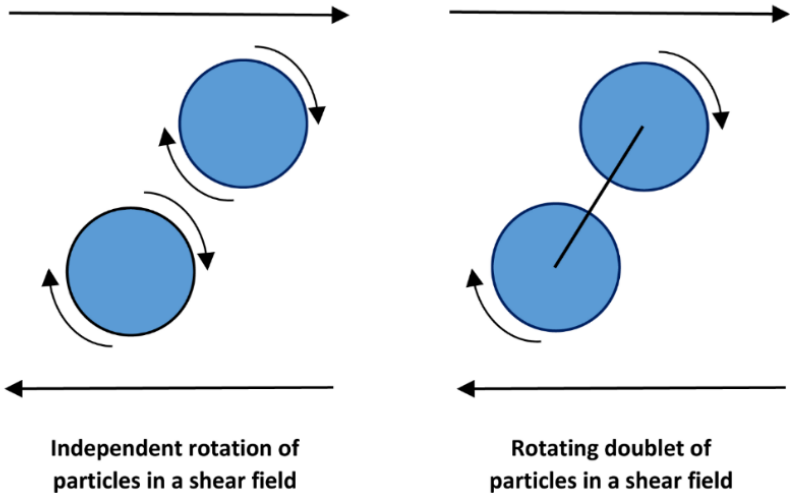

Figure 24. Formation and rotation of collision doublets.

The viscosity data of shear-thinning non-dilute emulsions can be scaled in terms of η_r versus $N_{Re,p}$ regardless of the droplet size (at a fixed λ). Pal [7,24,28] has published several articles on the rheology of non-dilute emulsions of noncolloidal droplets assuming the capillary number to be small ($N_{Ca}\rightarrow 0$). As an example, Figure 25 shows the η_r versus $N_{Re,p}$ data of Pal [7] for non-dilute emulsions at various values of φ. At any given φ, η_r versus $N_{Re,p}$ data for emulsions of different average droplet sizes overlap. Thus, the η_r data for the non-Newtonian shear-thinning emulsions having different droplet sizes can be scaled very well with $N_{Re,p}$.

Figure 26 shows the effect of φ on the η_r versus $N_{Re,p}$ curves for monomodal emulsions [20]. The η_r increases with the increase in φ, as expected. The increase in η_r with the increase in φ is quite large at low $N_{Re,p}$. As the $N_{Re,p}$ increases, the gap between different η_r versus $N_{Re,p}$ curves become smaller because of the shear-thinning effect.

 doi:10.20944/preprints202603.0830.v1

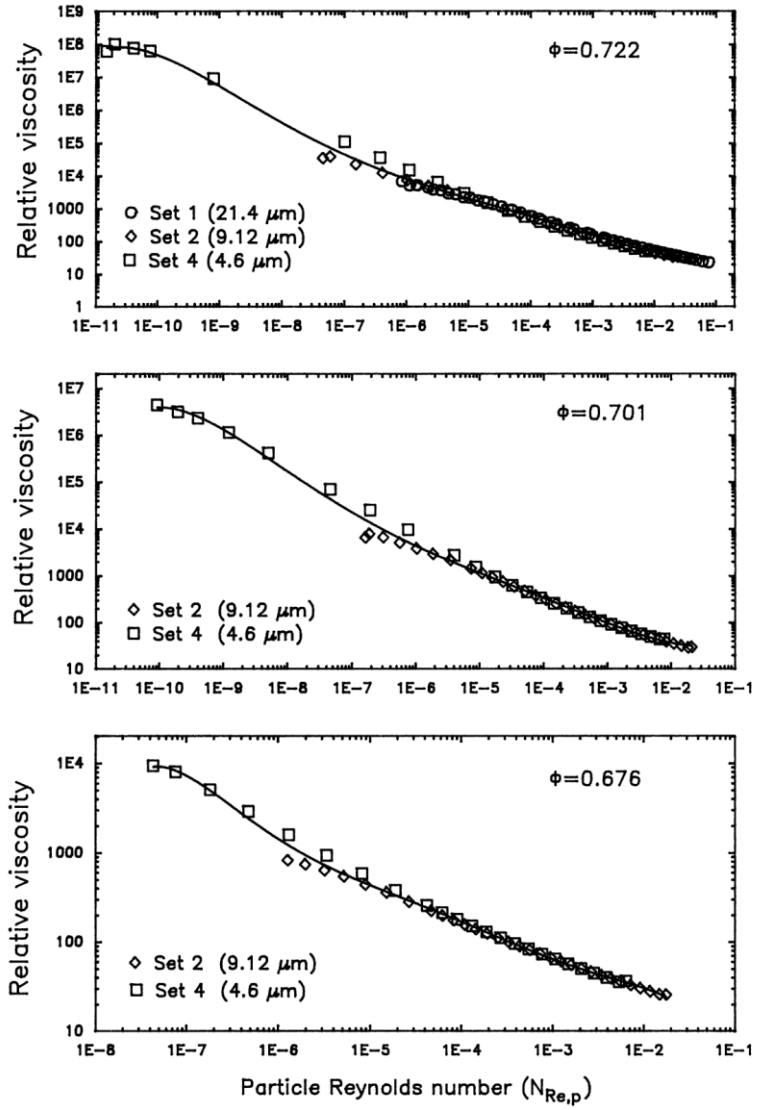

Figure 25. Scaling of relative viscosity with $N_{Re,p}$.

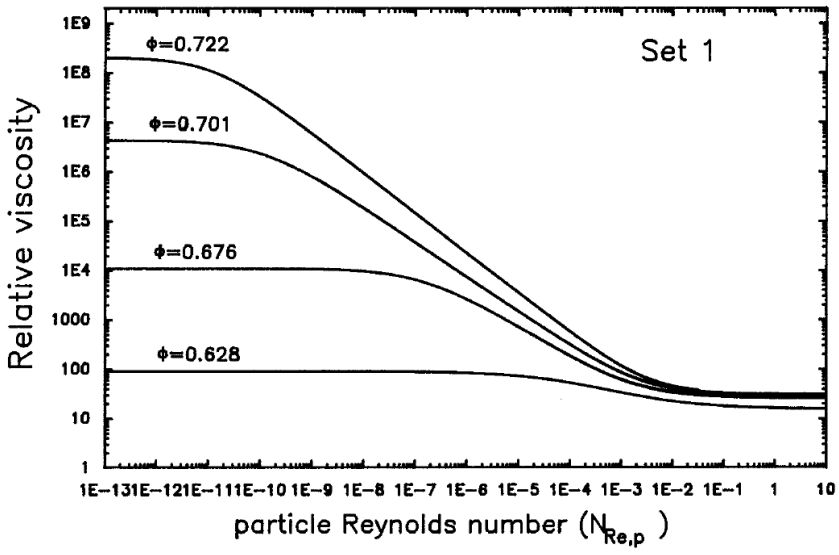

Figure 26. Relative viscosity with $N_{Re,p}$ curves for monomodal emulsions showing the effect of φ.

The η_r versus $N_{Re,p}$ curves follow the model given as [20]:

 doi:10.20944/preprints202603.0830.v1

$$\frac{\eta_r-\eta_{r\infty}}{\eta_{r0}-\eta_{r\infty}}=\frac{1}{1+a\left(N_{Re,p}\right)^b} \quad (43)$$

where η_{r0} is zero-shear η_r, $\eta_{r\infty}$ is high shear limiting η_r, a and b are constants. According to Equation (43), the plot of $[(\eta_r-\eta_{r\infty})/(\eta_{r0}-\eta_{r\infty})]^{-1}-1$ versus $N_{Re,p}$ is expected to be a straight line on a log-log scale. Figure 27 shows such a plot for monomodal emulsions of Sauter mean diameter of 4.6 μm at different volume fractions of droplets [20]. The plots of $[(\eta_r-\eta_{r\infty})/(\eta_{r0}-\eta_{r\infty})]^{-1}-1$ versus $N_{Re,p}$ are indeed linear on a log-log scale. The slope of the plots, that is, b in Equation (43) is nearly the same for all the plots corresponding to different values of φ. However, the constant a in Equation (43) varies with φ. Figure 27 also shows that the experimental data at different φ for monomodal emulsions overlap when plotted as $[(\eta_r-\eta_{r\infty})/(\eta_{r0}-\eta_{r\infty})]^{-1}-1$ versus $N_{Re,p}/\left(N_{Re,p}\right)_{critical}$ where $\left(N_{Re,p}\right)_{critical}$ is $N_{Re,p}$ where $[(\eta_r-\eta_{r\infty})/(\eta_{r0}-\eta_{r\infty})]^{-1}=0.5$.

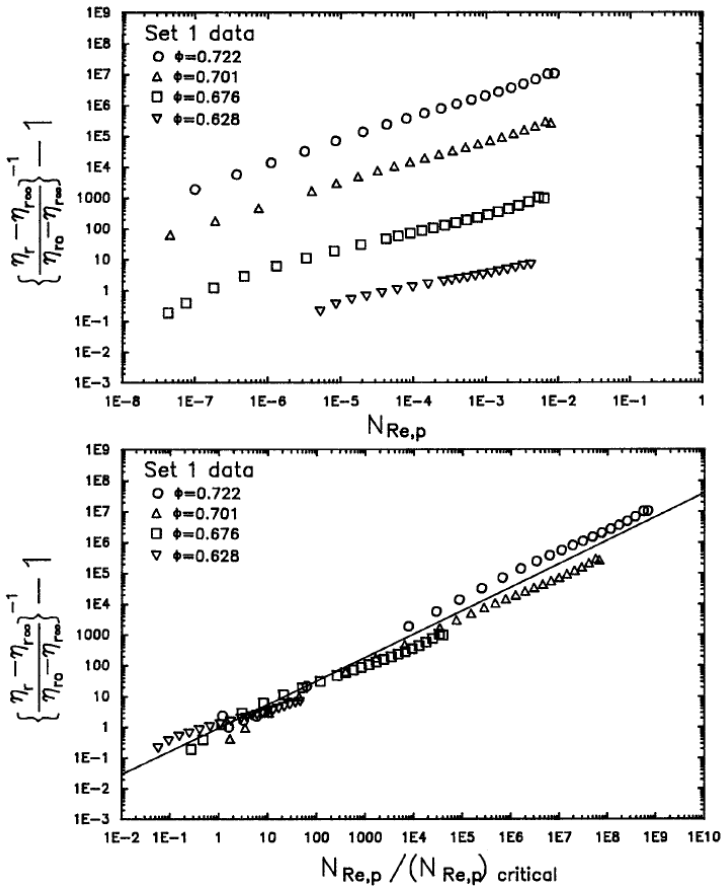

Figure 27. $[(\eta_r-\eta_{r\infty})/(\eta_{r0}-\eta_{r\infty})]^{-1}-1$ versus $N_{Re,p}$ and $N_{Re,p}/\left(N_{Re,p}\right)_{critical}$ for monomodal emulsions.

Figure 28 shows the plots of $[(\eta_r-\eta_{r\infty})/(\eta_{r0}-\eta_{r\infty})]^{-1}-1$ versus $N_{Re,p}$ and $N_{Re,p}/\left(N_{Re,p}\right)_{critical}$ for bimodal emulsions at a fixed $\varphi=0.745$ but varying fractions of fine and coarse droplets in the bimodal emulsion. Once again, linear plots are observed and all the data fall on the same line when plotted as $[(\eta_r-\eta_{r\infty})/(\eta_{r0}-\eta_{r\infty})]^{-1}-1$ versus $N_{Re,p}/\left(N_{Re,p}\right)_{critical}$. The slope of the line is the same as in Figure 27, that is, $b=0.673$. thus, all the data of Figures 27 and 28 could be described by the following equation [20]:

$$\frac{\eta_r-\eta_{r\infty}}{\eta_{r0}-\eta_{r\infty}}=\frac{1}{1+\left[N_{Re,p}/\left(N_{Re,p}\right)_{critical}\right]^{0.673}} \quad (44)$$

 doi:10.20944/preprints202603.0830.v1

This appears to be a universal correlation valid for all non-dilute shear-thinning emulsions where non-hydrodynamic effects are absent and $N_{Ca}\rightarrow 0$. However, η_{r0}, $\eta_{r\infty}$, and $\left(N_{Re,p}\right)_{critical}$ are expected to be dependent on φ, φ_{max}, and viscosity ratio λ.

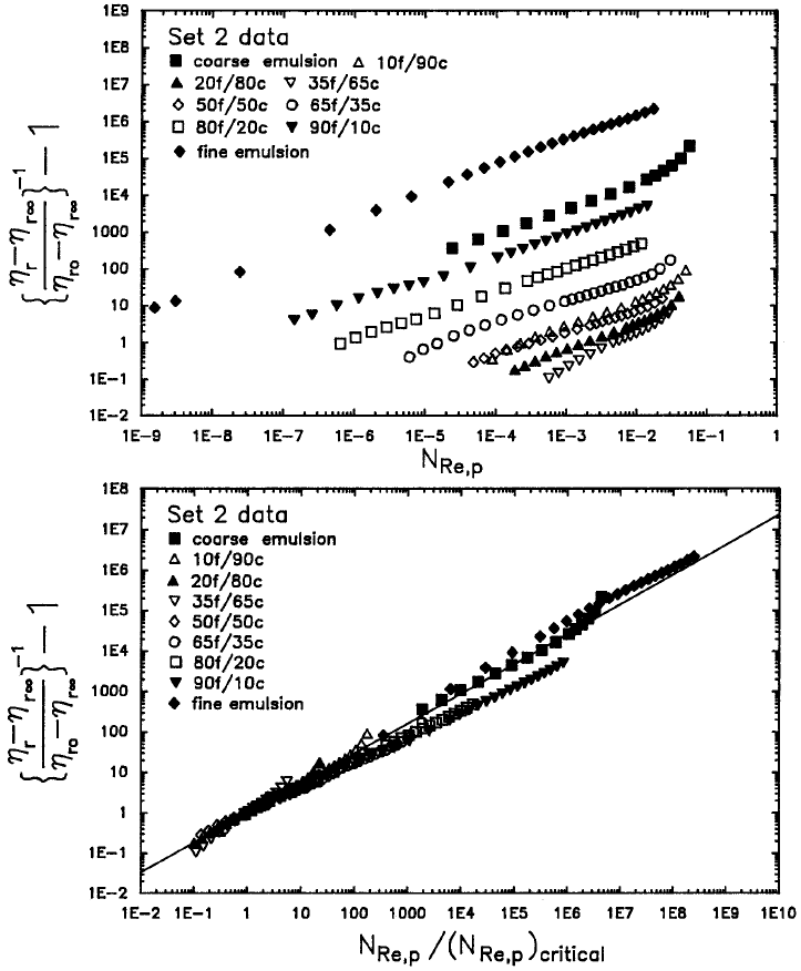

Figure 28. $[(\eta_r-\eta_{r\infty})/(\eta_{r0}-\eta_{r\infty})]^{-1}-1$ versus $N_{Re,p}$ and $N_{Re,p}/\left(N_{Re,p}\right)_{critical}$ for bimodal emulsions at $\varphi=0.745$.

Pal [28] proposed another approach to correlate the relative viscosity versus $N_{Re,p}$ data of multimodal non-dilute emulsions. According to dimensional considerations [32],

$$\eta_r = f\left([\eta],\varphi,\varphi_{max},N_{Re,p}\right) \tag{45}$$

where the intrinsic viscosity $[\eta]$ is a function of viscosity ratio λ, given as $(5\lambda+2)/(2\lambda+2)$. For a given λ and φ, η_r is a function of only φ_{max} and $N_{Re,p}$. For example, Figure 29(a) shows the η_r data for fine, coarse, and mixed kerosene-in-water emulsions at $\varphi=0.70$. The η_r is not a function of $N_{Re,p}$ alone. It also depends on the droplet size distribution. Emulsions with different proportions of fine droplets give different η_r especially at low values of $N_{Re,p}$. In Figure 29(b), the same data are replotted as $\varphi_{max}^{1/2}\left[1-\eta_r^{-1/\varphi_{max}[\eta]}\right]$ versus $N_{Re,p}$. The data for fine, coarse, and mixed emulsions overlap represented by the following empirical fit [28]:

$$\varphi_{max}^{1/2}\left[1-\eta_r^{-1/\varphi_{max}[\eta]}\right]=A_0+A_1log_{10}\left(N_{Re,p}\right)+A_2log_{10}\left(N_{Re,p}\right)^2 \tag{46}$$

where $A_0=0.69958$, $A_1=-5.6191\times10^{-2}$, and $A_3=-5.0269\times10^{-3}$.

 doi:10.20944/preprints202603.0830.v1

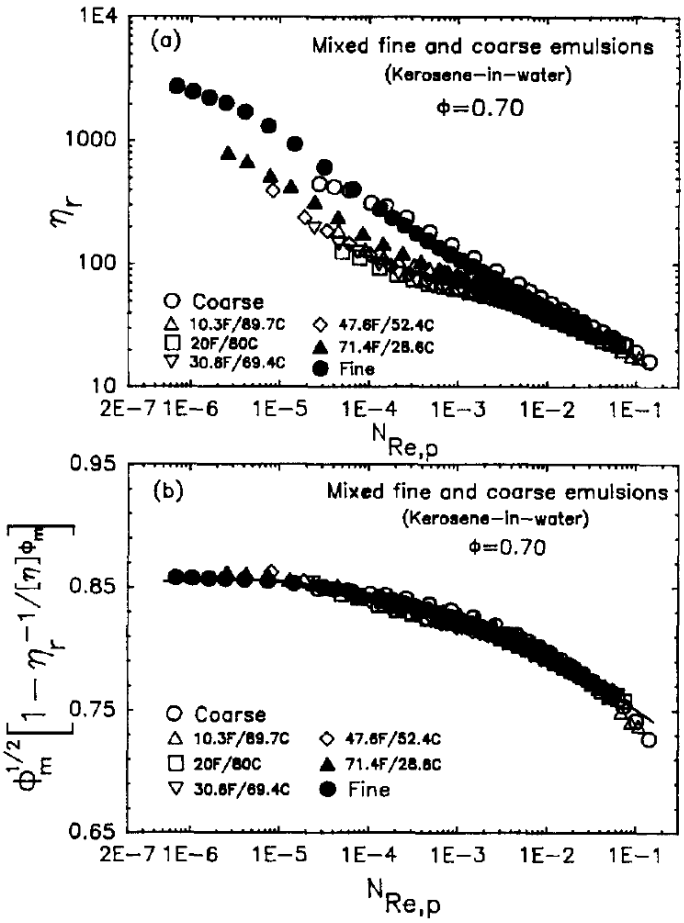

Figure 29. Correlation η_r and $\varphi_{max}^{1/2}\left[1-\eta_r^{-1/\varphi_{max}[\eta]}\right]$ as a function of $N_{Re,p}$ for bimodal emulsions at $\varphi = 0.70$.

3. Rheology of Non-Dilute Emulsions of Deformable Droplets

Figure 30 illustrates that the emulsion droplet deforms and orients with the flow field. When the shear rate is increased, the droplets become more stretched and aligned with the flow field. Consequently, even very dilute emulsions (extremely low φ) exhibit shear-thinning behavior [29–32]. Two dimensionless groups are important: λ and N_{Ca}. The droplets of emulsions undergo internal circulation that is governed by the viscosity ratio. Upon increasing the N_{Ca}, the droplets become more stretched and streamlined with the flow. This explains shear-thinning behavior of emulsions regardless of dilute or non-dilute in droplet concentration.

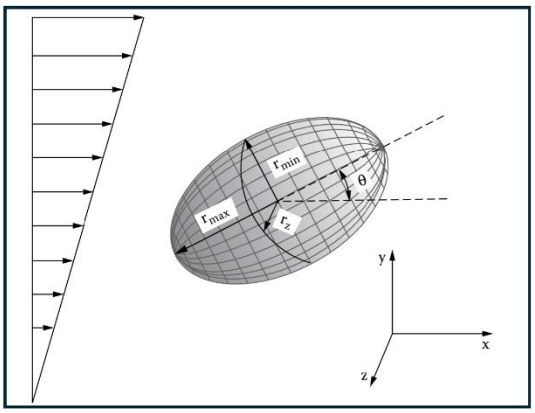

 doi:10.20944/preprints202603.0830.v1

Figure 30. Deformed droplet in shear flow.

Frankel and Acrivos [31] derived the rheological constitutive law for infinitely dilute emulsions considering small deformation of droplets in the flow field. Their constitutive law is given as:

$$\left[1+\tau_o\frac{D}{Dt}\right]\bar{\bar{\tau}} = 2\eta_c\left[1+\frac{5\lambda+2}{2(1+\lambda)}\varphi\right]\left[\bar{\bar{E}}+\tau_o\frac{D\bar{\bar{E}}}{Dt}\right]+$$
$$\varphi\eta_c\left(\frac{\eta_c R}{\gamma}\right)\left[-\frac{1}{40}\left(\frac{19\lambda+16}{1+\lambda}\right)^2\frac{D\bar{\bar{E}}}{Dt}+\frac{3(19\lambda+16)(25\lambda^2+41\lambda+4)}{140(1+\lambda)^3}\times Sd\left(\bar{\bar{E}}\cdot\bar{\bar{E}}\right)\right] \quad (47)$$

where D/Dt is the Jaumann derivative, $\bar{\bar{\tau}}$ is the viscous stress tensor, $\bar{\bar{E}}$ is the rate of strain tensor, τ_o is the characteristic time constant for the emulsion given as:

$$\tau_o = \frac{(19\lambda+16)\ (2\lambda+3)}{40(1+\lambda)}\left(\frac{\eta_c R}{\gamma}\right) \quad (48)$$

Note that $Sd\left(\bar{\bar{E}}\cdot\bar{\bar{E}}\right)$ is given as:

$$S_d\left(\bar{\bar{E}}\cdot\bar{\bar{E}}\right) = \frac{1}{2}\left[\bar{\bar{E}}\cdot\bar{\bar{E}}+\left(\bar{\bar{E}}\cdot\bar{\bar{E}}\right)^T-\frac{2}{3}tr\left(\bar{\bar{E}}\cdot\bar{\bar{E}}\right)\bar{\bar{\delta}}\right] \quad (49)$$

where superscript T indicates the transpose of a tensor, tr refers to trace of a tensor, and $\bar{\bar{\delta}}$ is unit tensor. Equation (47) predicts pseudoplastic, that is, shear-thinning behaviour, of emulsions and viscosity is given as:

$$\eta = \frac{\eta_c}{1+\tau_o^2\dot{\gamma}^2}\left\{1+\left(\frac{5\lambda+2}{2\lambda+2}\right)\varphi+\tau_o^2\dot{\gamma}^2\left[1+\left(\frac{5\lambda+2}{2\lambda+2}\right)\varphi-\frac{(19\lambda+16)}{(2\lambda+2)(2\lambda+3)}\varphi\right]\right\} \quad (50)$$

Eq. (50) gives:

$$[\eta] = \lim_{\varphi\to 0}\left(\frac{\eta-\eta_c}{\varphi\eta_c}\right) = \frac{1}{1+(hCa)^2}\left\{\left(\frac{5\lambda+2}{2\lambda+2}\right)\left[1+(hN_{Ca})^2-\frac{(19\lambda+16)}{(5\lambda+2)(2\lambda+3)}(hN_{Ca})^2\right]\right\} \quad (51)$$

where $h=(19\lambda+16)(2\lambda+3)/[40(1+\lambda)]$ and N_{Ca} is $\eta_c\dot{\gamma}R/\gamma$. Thus, $[\eta]$ of a dilute emulsion is dependent on λ and N_{Ca}. For a dilute emulsion of bubbles with $\lambda=0$, $h=6/5$ and $[\eta]$ becomes:

$$[\eta] = \frac{1}{\left\{1+\left(\frac{6N_{Ca}}{5}\right)^2\right\}}\left[1+\left(\frac{6N_{Ca}}{5}\right)^2-\frac{8}{3}\left(\frac{6N_{Ca}}{5}\right)^2\right] \quad (52)$$

Pal [33] also developed a viscosity equation for infinitely dilute emulsions. He utilized the analogy between shear modulus and shear viscosity to develop his equation given as follows:

$$\eta_r = \eta/\eta_c = [1\ +\ 5\varphi I] \quad (53)$$

where

$$I = \frac{(4/N_{Ca})(2+5\lambda)+(\lambda-1)(16+19\lambda)}{(40/N_{Ca})(1+\lambda)+(2\lambda+3)(16+19\lambda)} \quad (54)$$

The predictions of Equation (53) agree with Equation. (52).

Figure 31 shows the plots of $[\eta]$ of emulsion, defined as $(\eta_r-1)/\varphi$, as a function of N_{Ca} for different values of λ. Equation (53) is used to generate the plots. When $\lambda\to\infty$, that is, the droplets are rigid solid particles, the intrinsic viscosity is 2.5 independent of N_{Ca} indicating Newtonian behaviour. For a finite λ, the $[\eta]$ decreases as N_{Ca} is increased indicating pseudoplastic non-Newtonian behaviour. At a given N_{Ca}, $[\eta]$ increases as λ is increased. Note that the $[\eta]$ can even become negative at high N_{Ca}, when λ<1.

 doi:10.20944/preprints202603.0830.v1

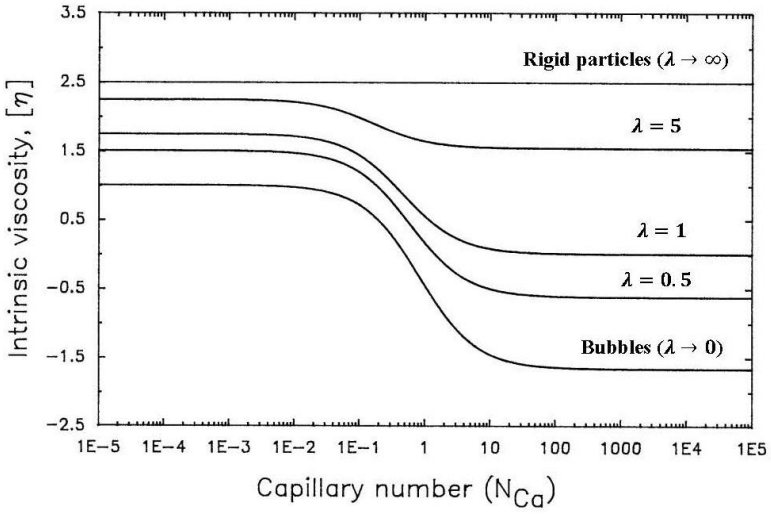

Figure 31. The effect of λ on emulsion $[\eta]$.

Starting from Eq. (54) and using the differential effective medium approach, Pal [33] derived the following viscosity equations for non-dilute emulsions:

$$\eta_r \left[\frac{M-P+32\eta_r}{M-P+32}\right]^{N-1.25} \left[\frac{M+P-32}{M+P-32\eta_r}\right]^{N+1.25} = (1-\varphi)^{-2.5} \quad (55)$$

$$\eta_r \left[\frac{M-P+32\eta_r}{M-P+32}\right]^{N-1.25} \left[\frac{M+P-32}{M+P-32\eta_r}\right]^{N+1.25} = exp\left[\frac{2.5\varphi}{1-\frac{\varphi}{\varphi_{max}}}\right] \quad (56)$$

$$\left[\frac{M-P+32\eta_r}{M-P+32}\right]^{N-1.25} \left[\frac{M+P-32}{M+P-32\eta_r}\right]^{N+1.25} = \left(1-\frac{\varphi}{\varphi_{max}}\right)^{-2.5\varphi_{max}} \quad (57)$$

where

$$M = \sqrt{(64/N_{Ca}^2) + 1225\lambda^2 + 1232(\lambda/N_{Ca})} \quad (58)$$

$$P = \frac{8}{N_{Ca}} - 3\lambda \quad (59)$$

$$N = \frac{(22/N_{Ca}) + 43.75\lambda}{\sqrt{(64/N_{Ca}^2) + 1225\lambda^2 + 1232(\lambda/N_{Ca})}} \quad (60)$$

Figure 32 shows η_r versus N_{Ca} plots generated from Equations (55)-(57), for two different values of λ at a fixed φ value of 0.50. The φ_{max} value used is 0.637. The η_r versus N_{Ca} plot at a given φ exhibits three distinct regions: constant η_r region at low values of N_{Ca}, pseudoplastic region at intermediate values of N_{Ca}, and finally constant η_r region again at high values of N_{Ca}. The η_r is always greater than unity for all values of N_{Ca} when $\lambda = 5$. However, for a low λ value of 0.1, η_r is greater than unity only when N_{Ca} is small. At high N_{Ca}, η_r becomes less than unity.

Figure 33 shows comparison between data and model predictions (Equations (55)-(57)) at low capillary number, $N_{Ca} \to 0$. The data covers a broad range of λ, 3.906 x $10^{-4} \leq \lambda \leq$ 3.25 x 10^5. The data are plotted as $Y^{0.4}$ versus φ, where Y is given as [37]:

$$Y = \eta_r \left[\frac{M-P+32\eta_r}{M-P+32}\right]^{N-1.25} \left[\frac{M+P-32}{M+P-32\eta_r}\right]^{N+1.25} \quad (61)$$

Note that Y is the left-hand side of Equations (55)-(57). The data can be described satisfactorily with Equation (57) using a single φ_{max} value of 0.637. Equation (55) underpredicts the viscosities whereas Equation (56) overpredicts the viscosities over the full range of φ.

 doi:10.20944/preprints202603.0830.v1

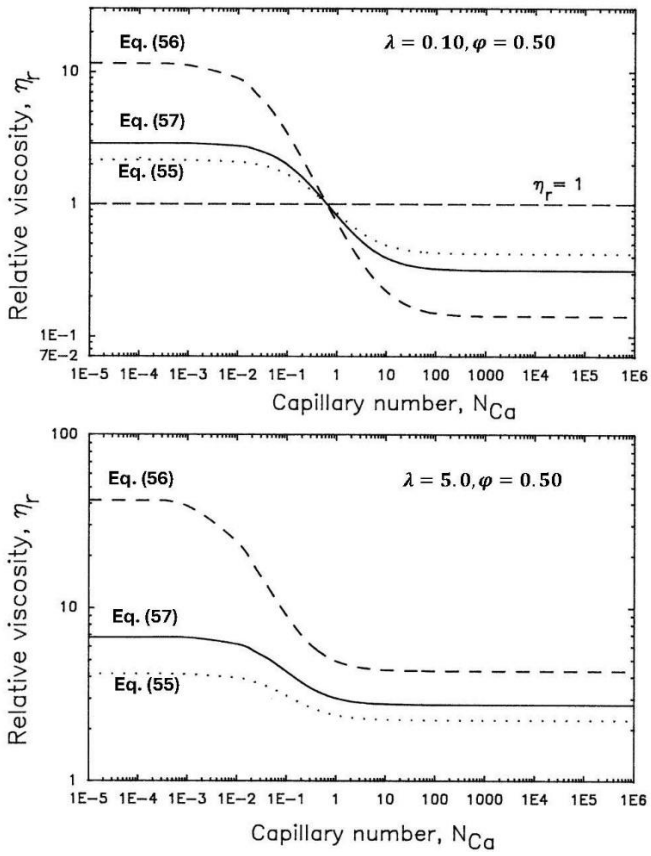

Figure 32. Relative viscosity versus capillary number predicted from Equations (55)-(57) at $\varphi = 0.50$. The φ_{max} used is 0.637 in calculations.

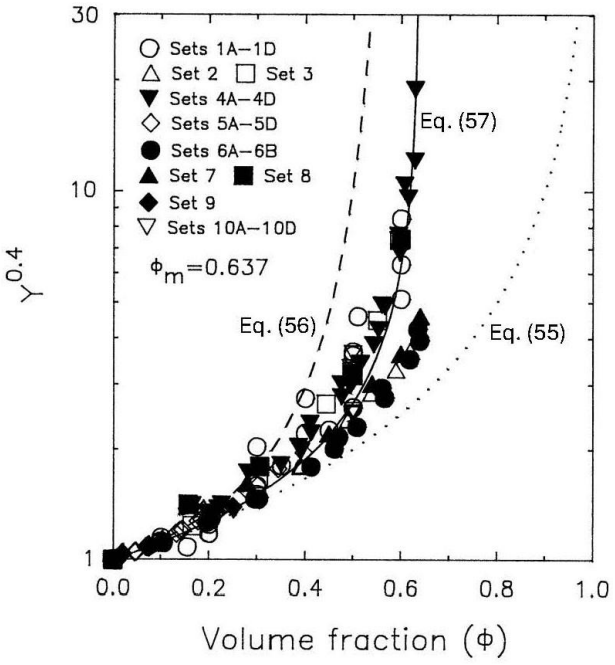

Figure 33. Comparison between model predictions and data at $N_{Ca} \to 0$.

Figure 34 shows comparison between data and model (Equations (55)-(57)) predictions at high capillary number, $N_{Ca} \to \infty$. The experimental data at high N_{Ca} were obtained for magmatic emulsions with $\lambda \to 0$. The data are plotted as Y versus φ, where Y is defined in Equation (61). Once again, Equation (57) shows good agreement with the data when a φ_{max} value of 0.637 is used.

 doi:10.20944/preprints202603.0830.v1

Equation (55) underestimates the viscosities whereas Equation (56) overestimates the viscosities at high φ.

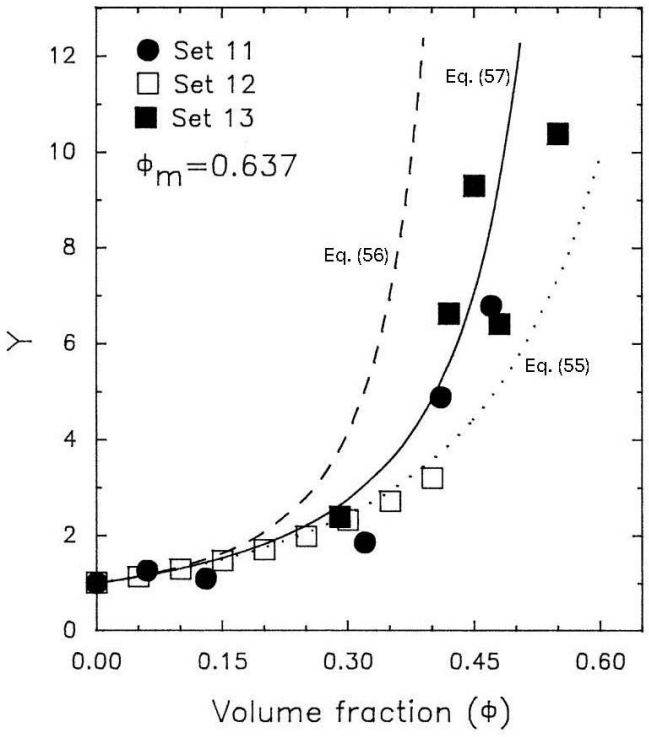

Figure 34. Comparison between model predictions and data at $N_{Ca} \to \infty$.

Figures 35-36 show comparisons between experimental and predicted profiles of η_r versus N_{Ca}. A φ_{max}value of 0.637 is used in the calculations. At high values of φ (Figure 35), Equation (57) gives good predictions. Equation (55) overpredicts and Equation (56) underpredicts the relative viscosities. Note that the relative viscosities are all less than one as capillary number is large. At low values of φ (Figure 36), Equations (55)-(57) predict similar values of η_r and show good agreement with the experimental data [33].

 doi:10.20944/preprints202603.0830.v1

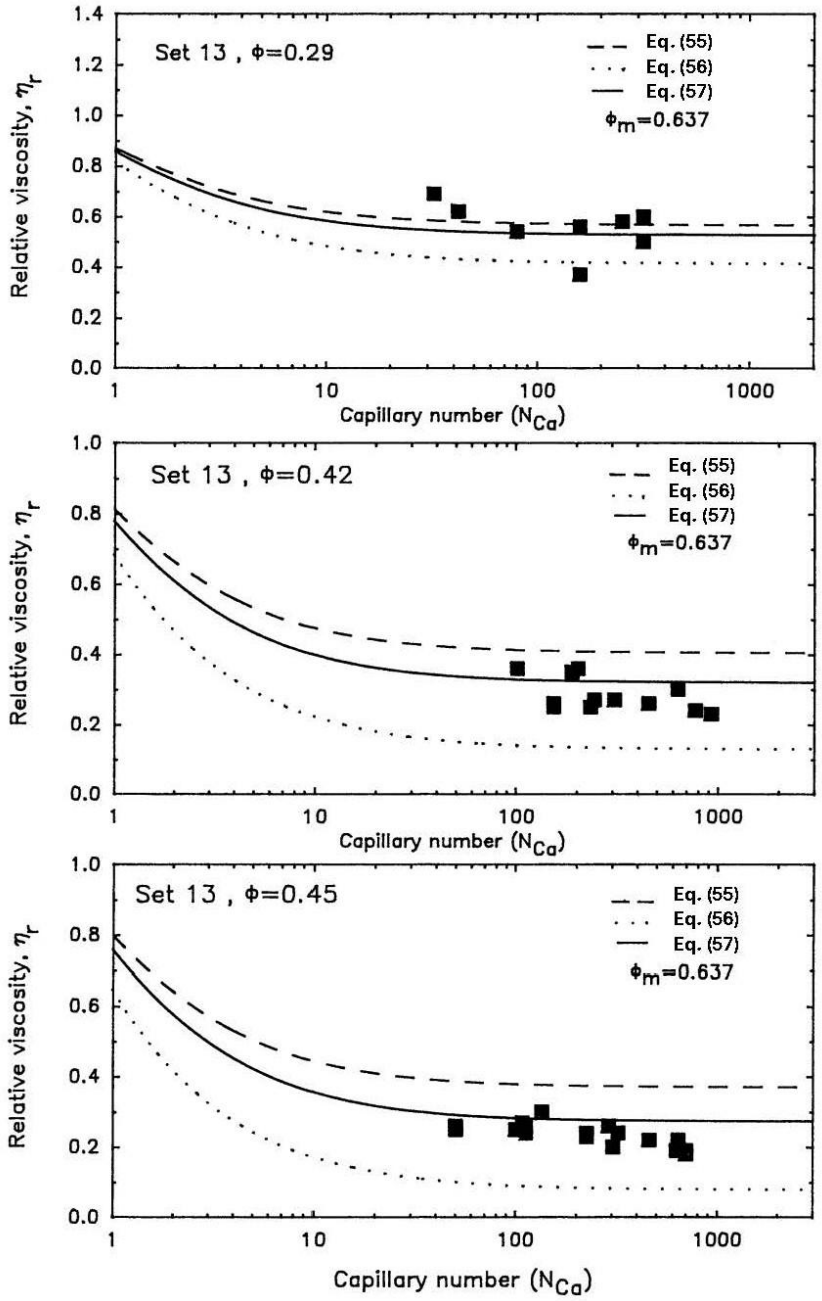

Figure 35. Comparison between model predictions and data of η_r as a function of N_{Ca}.

 doi:10.20944/preprints202603.0830.v1

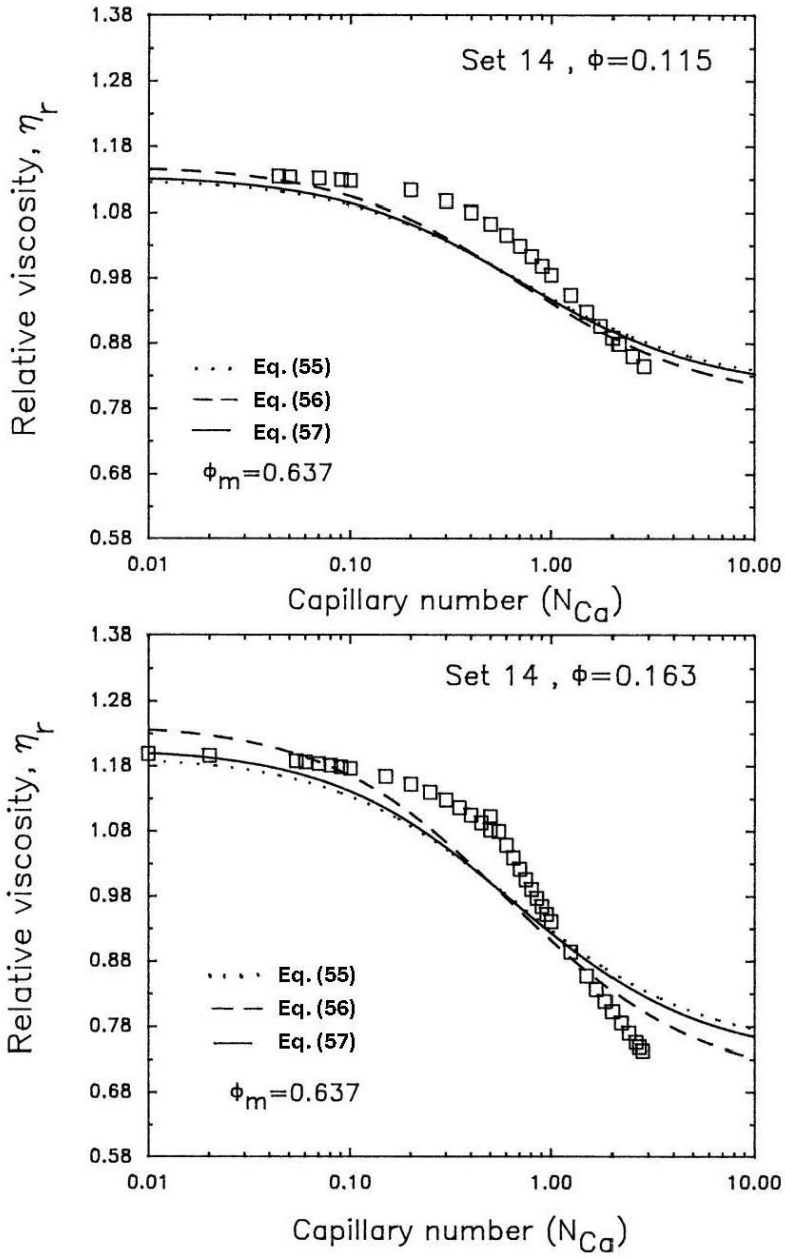

Figure 36. Comparison between model predictions and data of η_r as a function of N_{Ca}.

Pal [16] has recently proposed another improved model to describe the effect of N_{Ca} numbers on the η_r of non-dilute emulsions. It is as follows:

$$\eta_r \left[\frac{M-P+32\eta_r}{M-P+32}\right]^{R-1.25} \left[\frac{M+P-32}{M+P-32\eta_r}\right]^{R+1.25} = \left[1-\left\{1+\left(\frac{1-\varphi_{max}}{\varphi_{max}}\right)\left(\sqrt{1-\left(\frac{\varphi_{max}-\varphi}{\varphi_{max}}\right)^2}\right)\right\}\varphi\right]^{-2.5} \quad (62)$$

This model is based on the improved model of Equations (25)-(26). In the limit $N_{Ca} \to 0$, Equation (62) reduces to the model expressed in Equations (25)-(26).

4. Influence of Interfacial Rheology on the Bulk Rheology of Non-Dilute Emulsions

The bulk rheology of emulsions is strongly influenced by interfacial rheology. For a clean interface, the interface is characterized by only the interfacial tension (γ). In the presence of

 doi:10.20944/preprints202603.0830.v1

additives at the interface, the bulk rheological behavior is altered. Assuming that the interface is purely viscous in nature, the interface is now characterized by two interfacial viscosities, namely the surface shear viscosity (η_s) and the surface dilational viscosity (η_s^k), in addition to the interfacial tension. The rheological constitutive equation of a purely viscous interface is given as [29]:

$$\bar{\bar{\sigma}}_s = \gamma\bar{\bar{\delta}}_s + 2\eta_s\bar{\bar{E}}_s + (\eta_s^k - \eta_s)\left(\bar{\bar{\delta}}_s : \bar{\bar{E}}_s\right)\bar{\bar{\delta}}_s \quad (63)$$

where $\bar{\bar{\sigma}}_s$ is the surface-stress tensor, $\bar{\bar{E}}_s$ is the surface rate-of-strain tensor, and $\bar{\bar{\delta}}_s$ is surface unit tensor.

The bulk rheology of emulsion is linked to the interface constitutive equation through the boundary conditions at the droplet surface. For additive laden interface, the tangential viscous tractions are no longer continuous at the interface as observed in the case of clean interface. At the droplet surface, the tangential stress discontinuity is expressed as [29]:

$$\hat{n} \bullet (\bar{\bar{\sigma}} - \bar{\bar{\sigma}}^*) \bullet \bar{\bar{\delta}}_s = -(\nabla_s \bullet \bar{\bar{\sigma}}_s) \bullet \bar{\bar{\delta}}_s \quad (64)$$

The normal stress discontinuity across the interface is given as [29]:

$$\hat{n} \bullet (\bar{\bar{\sigma}} - \bar{\bar{\sigma}}^*) \bullet \hat{n} = -(\nabla_s \bullet \bar{\bar{\sigma}}_s) \bullet \hat{n} \quad (65)$$

where $\bar{\bar{\sigma}}$ is the stress tensor at the interface from the matrix side, $\bar{\bar{\sigma}}^*$ is the stress tensor at the interface from the droplet side, ∇_s is the surface gradient operator defined as $(\bar{\bar{\delta}} - \hat{n}\hat{n}) \bullet \nabla$, $\bar{\bar{\delta}}$ is the unit tensor, ∇ is the del operator, and $\hat{n}$ is the outward unit normal vector.

For dilute emulsions $(\varphi \to 0)$ with purely viscous interfaces, the zero-shear relative viscosity (η_r) is given as [29,34]:

$$\eta_r = [1 + \alpha\varphi] \quad (66)$$

where α is defined as follows:

$$\alpha = \frac{1+\frac{5}{2}\lambda+2N_{Bo}^{\eta}+3N_{Bo}^{k}}{1+\lambda+\frac{2}{5}\left(2N_{Bo}^{\eta}+3N_{Bo}^{k}\right)} \quad (67)$$

Here N_{Bo}^{η} is the shear Boussinesq number defined as $\eta_s/\eta_c R$, R is the droplet radius, and N_{Bo}^{k} is the dilational Boussinesq number defined as $\eta_s^k/\eta_c R$.

For an inviscid interface, $N_{Bo}^{\eta} \to 0$ and $N_{Bo}^{k} \to 0$ and the tangential viscous tractions are continuous at the interface. In this case, Equation (66) reduces to the Taylor viscosity equation (Equation (1)) for dilute emulsions of spherical droplets with clean interfaces. When the interface is highly viscous, that is, $\left(2N_{Bo}^{\eta} + 3N_{Bo}^{k}\right) \gg 1$, the transmission of tangential stresses from the continuous phase to the droplet phase is severely inhibited and α becomes 5/2. In this case, Equation (66) reduces to the Einstein expression for the viscosity of dilute suspension of rigid particles [33]:

$$\eta_r = \left(1 + \frac{5}{2}\varphi\right) \quad (68)$$

Equation (66) assumes that the interfacial properties are uniform over the entire interface. If the surfactant distribution over the droplet surface is not uniform, complications could arise due to the generation of Marangoni stresses. The Marangoni stresses cause the droplets to behave more like rigid particles. However, if the surface Peclet number (N_{Pe}^{s}) is very small $(N_{Pe}^{s} \to 0)$, the Marangoni stresses can be neglected. The Peclet number is defined as:

$$N_{Pe}^{s} = \frac{R^2\dot{\gamma}}{D_s} \quad (69)$$

where D_s is surface diffusivity of the surfactant.

 doi:10.20944/preprints202603.0830.v1

Danov [35] considered the Marangoni phenomenon in emulsions and derived the following expression for the zero-shear η_r:

$$\eta_r = \left[1 + \left(1 + \frac{3}{2}\varepsilon_m\right)\varphi\right] \tag{70}$$

where ε_m is the *interfacial mobility parameter*, given as:

$$\varepsilon_m = \left[\frac{\lambda + \frac{2}{5}\left(\frac{RE_G}{2\eta_c D} + 2N_{Bo}^{\eta} + 3N_{Bo}^{k}\right)}{1 + \lambda + \frac{2}{5}\left(\frac{RE_G}{2\eta_c D} + 2N_{Bo}^{\eta} + 3N_{Bo}^{k}\right)}\right] \tag{71}$$

where D is the effective diffusion coefficient of the surfactant and E_G is the Gibbs elasticity of the interface defined as:

$$E_G = -\left(\frac{\partial \gamma}{\partial \ell n \Gamma}\right) \tag{72}$$

where Γ is the surfactant concentration.

Equation (70) reduces to Equation (66) for interfaces with negligible Gibbs elasticity ($E_G \to 0$). The ε_m varies from 0 to 1, that is, $0 \le \varepsilon_m \le 1$. For a completely mobile interface such as bubbles without any surface additives, ε_m is 0 and for a completely immobile interface such as rigid particles, ε_m is unity. When the Gibbs elasticity of interface is high, that is, the Marangoni effect is strong, $E_G \to \infty$ and the parameter ε_m is unity. In this case, the expression for emulsion viscosity, Equation (70), reduces to Equation (68). For surfactant-free clean interface: $E_G \to 0$, $N_{Bo}^{\eta} \to 0$, $N_{Bo}^{k} \to 0$, and ε_m is $\lambda/(1+\lambda)$. Thus, the expression for emulsion viscosity, Eq. (70), reduces to the Taylor formula (Equation (1)). Note that $\varepsilon_m = 0$ only when the interface is completely mobile, that is, the dispersed phase is bubbles without any additives.

The viscosity models, Equations (66) and (70), are restricted to very dilute emulsions in the limit $\varphi \to 0$. Pal [36] developed models for non-dilute emulsions considering the effect of interfacial rheology. Starting with the dilute emulsion equation, Equation (70), and using the differential effective medium approach (DEMA), he developed the following models for non-dilute emulsions:

$$\eta_r \left[\frac{2\eta_r + 5\lambda + 2\left(\frac{RE_G}{2\eta_c D} + 2N_{Bo}^{\eta} + 3N_{Bo}^{k}\right)}{2 + 5\lambda + 2\left(\frac{RE_G}{2\eta_c D} + 2N_{Bo}^{\eta} + 3N_{Bo}^{k}\right)}\right]^{3/2} = (1-\varphi)^{-2.5} \tag{73}$$

$$\eta_r \left[\frac{2\eta_r + 5\lambda + 2\left(\frac{RE_G}{2\eta_c D} + 2N_{Bo}^{\eta} + 3N_{Bo}^{k}\right)}{2 + 5\lambda + 2\left(\frac{RE_G}{2\eta_c D} + 2N_{Bo}^{\eta} + 3N_{Bo}^{k}\right)}\right]^{3/2} = exp\left(\frac{2.5\varphi}{1 - \frac{\varphi}{\varphi_{max}}}\right) \tag{74}$$

$$\eta_r \left[\frac{2\eta_r + 5\lambda + 2\left(\frac{RE_G}{2\eta_c D} + 2N_{Bo}^{\eta} + 3N_{Bo}^{k}\right)}{2 + 5\lambda + 2\left(\frac{RE_G}{2\eta_c D} + 2N_{Bo}^{\eta} + 3N_{Bo}^{k}\right)}\right]^{3/2} = \left(1 - \frac{\varphi}{\varphi_{max}}\right)^{-2.5\varphi_{max}} \tag{75}$$

Figure 37 compares predictions of Equations (73)-(75) at a fixed volume fraction of droplets, that is, φ = 0.5. As can be seen, the relative viscosity of the emulsion increases with the increase in the value of the interfacial mobility parameter (ε_m) from 0 (bubbly suspension) to unity (rigid particle suspension). The Danov model (Equation (70)) predicts the lowest η_r as this model fails to consider hydrodynamic interactions between the droplets. The predictions of the models expressed in Equation (73)-(75) are in the following order: η_r (Equation (74)) > η_r (Equation (75)) > η_r (Equation (73)).

Figure 38 shows η_r versus φ plots different values of ε_m. The $\varphi_{max}$of 0.637 is used. The relative viscosity increases with the increase in ε_m for a given φ. Pal [36] estimated ε_m for emulsions using viscosity data of emulsions and fitting Equation (75) to the data. The φ_{max} value of 0.637 was used. Figure 39 shows the goodness of fit of Equation (75) to individual sets of data and

 doi:10.20944/preprints202603.0830.v1

the corresponding effective ε_m values. In Figure 40, effective ε_m versus $\varepsilon_{m,clean}$ is plotted where $\varepsilon_{m,clean}$ is calculated for the clean interface as $\varepsilon_{m,clean} = \lambda/(1+\lambda)$. Note that the emulsions consisted of interfaces coated with surfactants. The effective ε_m is generally larger than $\varepsilon_{m,clean}$ due to the presence of additives at the interface. The effect of interfacial additives is particularly important for emulsions with low viscosity ratio where $\varepsilon_{m,clean} \ll 1$.

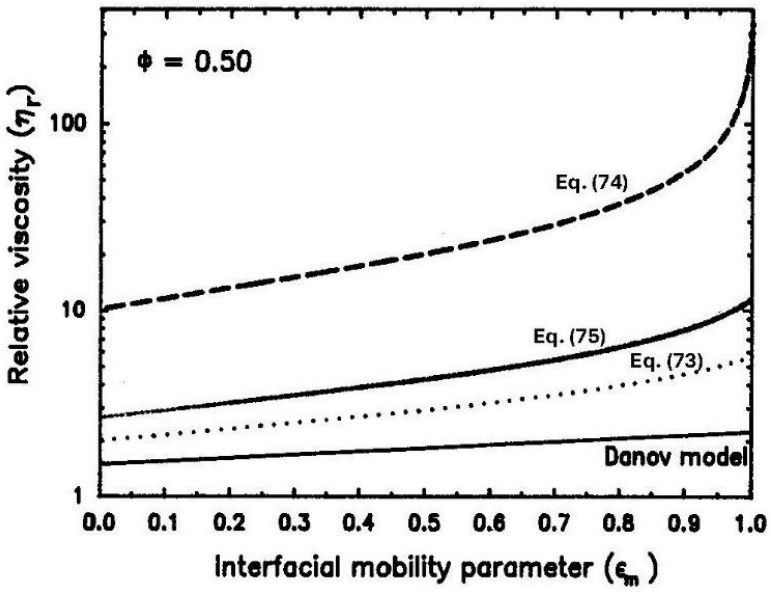

Figure 37. Predictions of η_r as a function of ε_m from the models expressed in Equations (70), (73)-(75). The emulsion φ is 0.5.

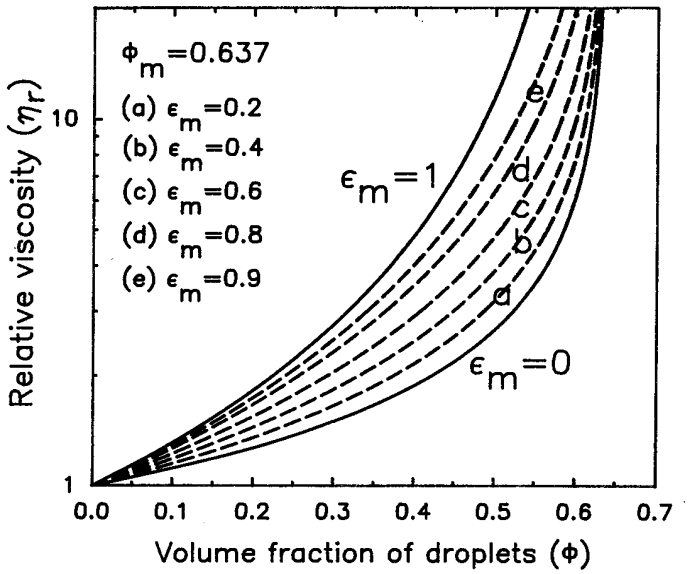

Figure 38. Relative viscosity predicted from Equation (75) for different ε_m.

 doi:10.20944/preprints202603.0830.v1

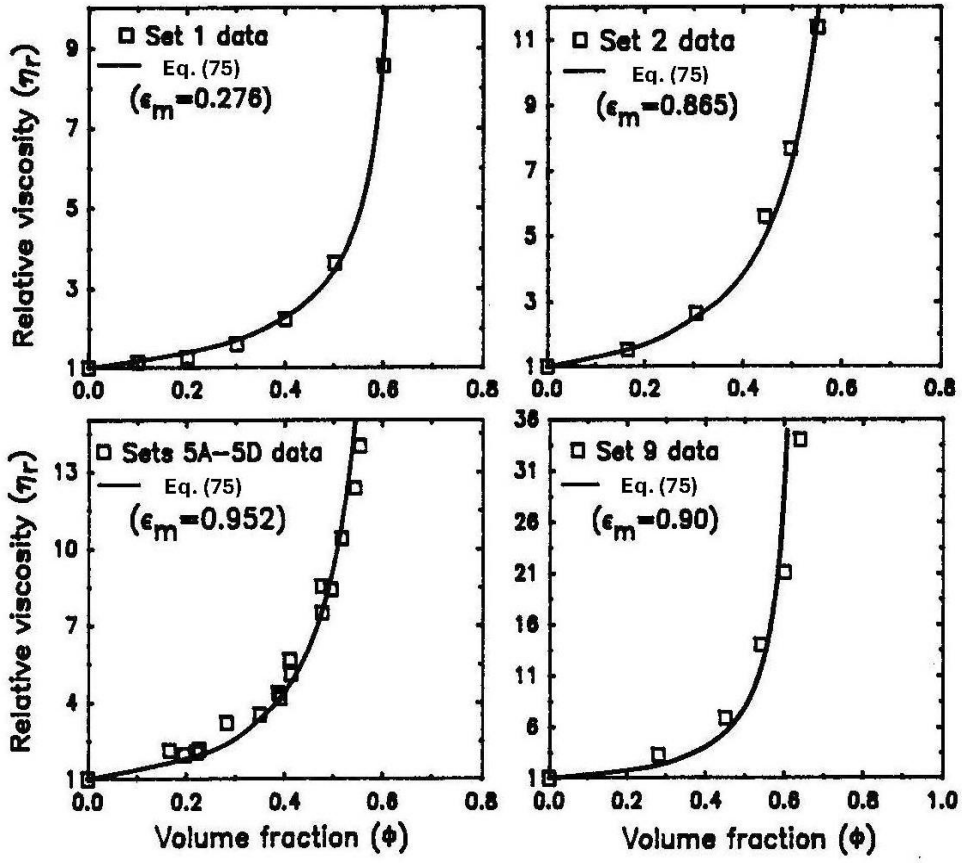

Figure 39. Comparisons between data and predictions of Equation (75).

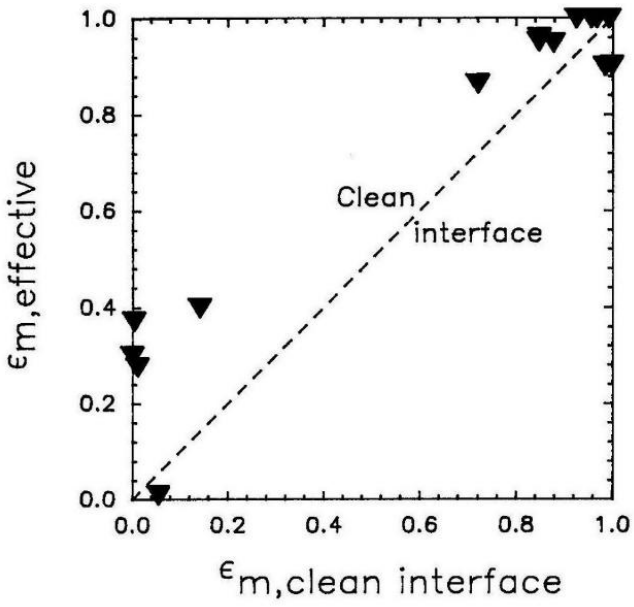

Figure 40. Plot of effective ε_m versus $\varepsilon_{m,clean}$ where $\varepsilon_{m,clean}$ is calculated from the viscosity ratio $\varepsilon_{m,clean} = \lambda/(1+\lambda)$. Note that $\varepsilon_{m,clean} = 0$ corresponds to bubbles with clean interface and $\varepsilon_{m,clean} = 1$ corresponds to high viscosity droplets with clean interface.

5. Influence of Surface Charge on the Rheology of Non-Dilute Emulsions

 doi:10.20944/preprints202603.0830.v1

The rheological properties of emulsion are strongly affected by the presence of electric charge on the surface of the droplets. As shown schematically in Figure 41, an electrically charged droplet attracts a cloud of counter-ions. Just next to the charged droplet surface, a monolayer of immobile ions of opposite charge is formed. This immobile layer of ions is called *Stern layer*. Outside the Stern layer, the ionic cloud consists of mobile co-ions and counter-ions. This diffused outer layer of ions is referred to as *Gouy* or *Debye-Huckel layer*. The concentration of counter-ions is higher than that of co-ions in the diffuse layer. As one moves away from the droplet's surface, the concentration of counter-ions gradually decreases toward the bulk concentration. The charge cloud surrounding the droplet surface, that is, the Stern and diffuse layers combined, is referred to as an *electrical double layer* [37].

Figure 42 shows the plots of η_r versus φ data for negatively charged droplets (electrostatically stabilized emulsions) [38]. The charge density of the droplets is the same. However, the average droplet diameter varies from one plot to another. The η_r of emulsion is much higher when the average droplet is small. Referring to Figure 42, the relative viscosities are in the following order at a given concentration (volume fraction) of oil droplets: $\eta_r(27.5\ \text{nm}) \gg \eta_r(58.5\ \text{nm}) \gg \eta_r(102\ \text{nm}) \gg \eta_r(205\ \text{nm})$. The reason for the increase in η_r with the decrease in droplet size is an increase in electrical double layer thickness with respect to the droplet size. Thus, the relative double layer thickness (κ^{-1}/R) is an important factor in governing the rheological properties of emulsions of charged droplets. Note that κ^{-1} is the Debye length which is a measure of electrical double layer thickness and R is the droplet radius.

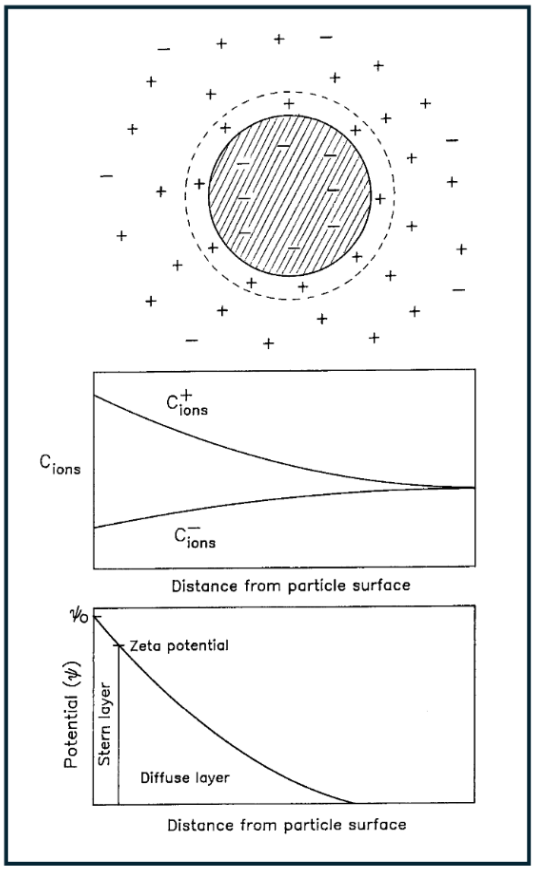

Figure 41. An electrically charged droplet surrounded by an ionic cloud. Variations of ionic concentration and electric potential with distance from the droplet surface are also shown.

 doi:10.20944/preprints202603.0830.v1

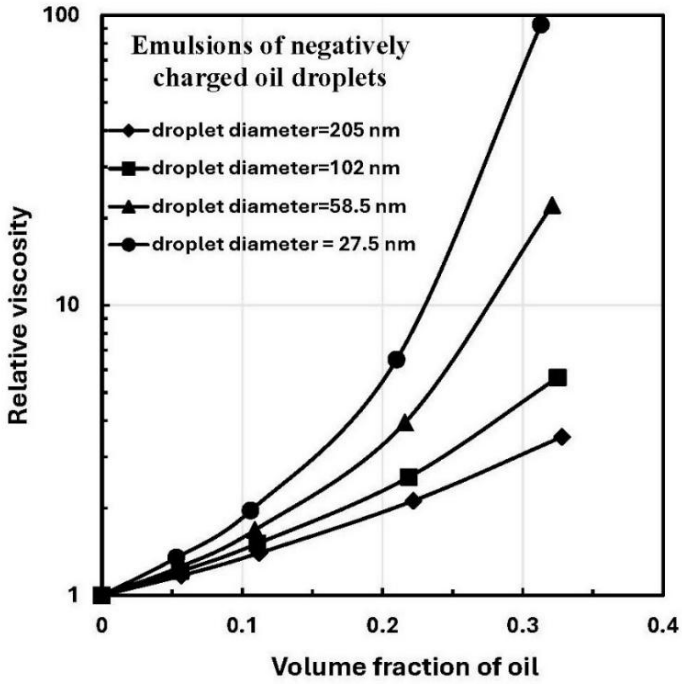

Figure 42. Relative viscosity of electrically charged non-dilute emulsions.

The theory for the viscosity of electrostatically stabilized dispersions has been well established. However, the studies are for the most part restricted to suspensions of solid particles. Nevertheless, they are equally relevant to emulsions. The viscosity of suspensions of electrically charged particles is governed by four dimensionless groups. They are Hartmann number (Ha), the ion Peclet number (Pe), the relative thickness of the electrical double layer ($1/R\kappa$), and the dimensionless surface potential ($\tilde{\psi}_0$). These dimensionless groups are defined as follows [27,29,37]:

$$Ha = \left(\frac{\varepsilon\psi_0^2}{\eta_c D}\right) \tag{76}$$

$$Pe = \frac{\dot{\gamma}}{\kappa^2 D} \tag{77}$$

$$R\kappa = R\sqrt{e^2 I/\varepsilon kT} \tag{78}$$

$$\tilde{\psi}_0 = \frac{e\psi_0}{kT} \tag{79}$$

where ψ_0 is surface potential, I is the bulk ionic strength, D is the ion diffusivity, ε is the permittivity of the fluid, k is the Boltzmann constant, T is the absolute temperature, R is the particle radius, e is electronic charge, and κ^{-1} is the Debye length (κ^{-1}) given as:

$$\kappa^{-1} = \sqrt{\varepsilon kT/e^2 I} \tag{80}$$

The Hartmann number Ha is the ratio of electrical force to viscous force acting on the fluid. It represents rigidity of the charge cloud. The ion Peclet number Pe is a measure of the extent to which the motion of the fluid relative to the particle disturbs the charge cloud. The dimensionless group $R\kappa$ is the inverse of relative thickness of the electrical double layer (κ^{-1}/R) with respect to the particle size. The dimensionless surface potential ($\tilde{\psi}_0$) is the ratio of electrical energy to thermal energy of ions.

The constitutive equation for a dilute suspension of electrically charged spherical particles under the condition that the distortion of charge cloud by fluid motion is small, that is, $Pe \ll 1$, can be expressed as [29,37]:

$$\bar{\bar{\sigma}} = -P\ \bar{\bar{\delta}} + 2\eta_c\ \bar{\bar{E}} + 5(1+p)\ \eta_c\ \varphi\ \bar{\bar{E}} \tag{81}$$

 doi:10.20944/preprints202603.0830.v1

where p is the primary electroviscous coefficient which depends on three dimensionless groups (assuming $Pe \to 0$), that is,

$$p = p(\tilde{\psi}_0, Ha, R\kappa) \tag{82}$$

From Eq. (81), it follows that

$$\eta_r = \left[1 + \frac{5}{2}(1+p)\varphi\right] \tag{83}$$

Several theoretical studies have been done to predict the primary electroviscous coefficient p [37,39–44] The predictive equations for p are summarized in Table 2.

Table 2. Primary electroviscous coefficient p for dilute suspensions of solid particles.

Primary electroviscous coefficient, p	Comments and restrictions
$p = 4\pi(Ha)(1+R\kappa)^2 f(R\kappa)$	low surface potential ($\tilde{\psi}_0 << 1$), low Hartmann number ($Ha << 1$), low $Pe \ll 1$
$f(R\kappa) = \frac{1}{200\pi(R\kappa)} + \frac{11(R\kappa)}{3200\pi}$	small $R\kappa$ ($R\kappa << 1$), that is, thick double layers
$f(R\kappa) = \frac{3}{2\pi(R\kappa)^4}$	large $R\kappa$ ($R\kappa >> 1$), that is, thin double layers.
$p = 6(Ha)(R\kappa)^{-2}$	thin electrical layers ($R\kappa >> 1$), low surface potential ($\tilde{\psi}_0 << 1$), low Hartmann number ($Ha << 1$), and low $Pe \ll 1$
$p = (Ha/50)(R\kappa)^{-1}$	thick electrical layers ($R\kappa << 1$), low surface potential, low Hartmann number ($Ha << 1$), and low $Pe \ll 1$
$p = \frac{72}{(R\kappa)^2}\left[m_+\left(ln\frac{1+e^{-\tilde{\psi}_0/2}}{2}\right)^2 + \left(\frac{m_-}{1+2F}\right)\left(ln\frac{1+e^{\tilde{\psi}_0/2}}{2}\right)^2\right]$ where $m_\pm = \frac{2\varepsilon kT}{3\eta_c Z^2 e^2}\lambda_\pm = \frac{2}{3}\left(\frac{Ha}{\tilde{\psi}_0^2}\right)$, $F = \frac{2}{R\kappa}(1+3m_-)\left(e^{\tilde{\psi}_0/2}-1\right)$. Note that $\lambda = kT/D$ and $\tilde{\psi}_0 = Ze\psi_0/kT$	Ohshima model [43]. Arbitrary surface potentials (no restriction on $\tilde{\psi}_0$), large $R\kappa$ ($R\kappa >> 1$), low $Pe \ll 1$, and Z-Z symmetrical type electrolyte where Z is the valence of the ion; $Z_1 = -Z_2 = Z$
$p = \frac{9(m_- + m_+)}{2(R\kappa)^2}\tilde{\psi}_0^2$	low surface potential, large $R\kappa$, and low $Pe \ll 1$
$p = 6(Ha)(R\kappa)^{-2}[1+Pe^2]^{-1}$	arbitrary Peclet number Pe, thin electrical layers ($R\kappa >> 1$), low surface potential ($\tilde{\psi}_0 << 1$), and low Hartmann number ($Ha << 1$)

For concentrated suspensions, the electroviscous coefficient p also depends on φ. The p for concentrated equations is defined according to the modified form of Eq. (83) [42]:

$$\eta_r = \left[1 + \frac{5}{2}(1+p)\varphi S(\varphi)\right] \tag{84}$$

where $S(\varphi)$ is given as:

$$S(\varphi) = \frac{4\left(1-\varphi^{7/3}\right)}{4\left(1-\varphi^{5/3}\right)^2 - 25\varphi\left(1-\varphi^{2/3}\right)^2} \tag{85}$$

Note that when $p = 0$ (uncharged particles), Equation (84) becomes the Simha equation for non-dilute suspensions of uncharged particles.

 doi:10.20944/preprints202603.0830.v1

For arbitrary surface potential and thin double layers, Ohshimo [44] has developed the expression for p for non-dilute suspensions of solid particles using the cell model approach. His model is listed in Table 3. An important point to note is that p for non-dilute suspensions considers interaction of double layers of neighbouring particles assuming there is no overlapping of double layers. Thus, p considers both primary and secondary electroviscous effects.

Table 3. Electroviscous coefficient p for non-dilute suspensions of solid particles.

Electroviscous coefficient, p	Comments and restrictions
$\eta_r = \left[1 + \frac{5}{2}(1+p)\varphi S(\varphi)\right]$	Concentrated suspension of rigid particles
$p = \frac{72}{(R\kappa)^2} S(\varphi)Q(\varphi)R(\varphi)\left[m_+\left(ln\frac{1+e^{-\tilde{\psi}_0/2}}{2}\right)^2 + \left(\frac{m_-}{1+2Q(\varphi)F}\right)\left(ln\frac{1+e^{\tilde{\psi}_0/2}}{2}\right)^2\right]$ where $S(\varphi) = \frac{4(1-\varphi^{7/3})}{4(1-\varphi^{5/3})^2 - 25\varphi(1-\varphi^{2/3})^2}$, $Q(\varphi) = \frac{3(1-\varphi^{5/3})}{3+2\varphi^{5/3}}$, $R(\varphi) = \left[1 - \frac{7(\varphi^{5/3}-\varphi^{7/3})}{2(1-\varphi^{7/3})}\right]^2$	Ohshimo model [44]. Arbitrary surface potential, thin double layer (large $R\kappa$), Z-Z symmetrical type electrolyte where Z is the valence of the ion; $Z_1 = -Z_2 = Z$

Figure 43 shows electroviscous coefficient p variation with φ for different values of dimensionless surface potential $\tilde{\psi}_0$ obtained from the Ohshimo model for concentrated suspensions described in Table 3. For a given $\tilde{\psi}_0$, the electroviscous coefficient p increases as φ increases. However, at a given value of φ, p initially increases with $\tilde{\psi}_0$, reaches a maximum value, and later falls off with further increase in φ. This can be seen more clearly on Figure 44.

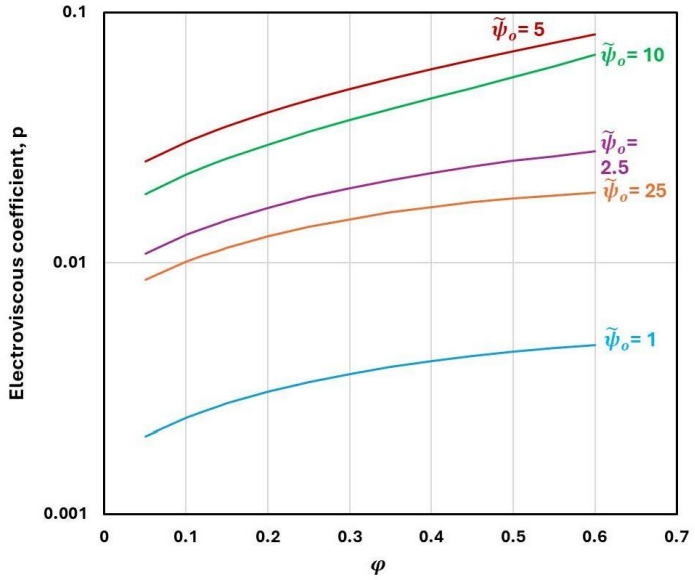

Figure 43. Variation of p with φ for concentrated suspensions. The $R\kappa$ value is 30. The electrolyte is KCl.

 doi:10.20944/preprints202603.0830.v1

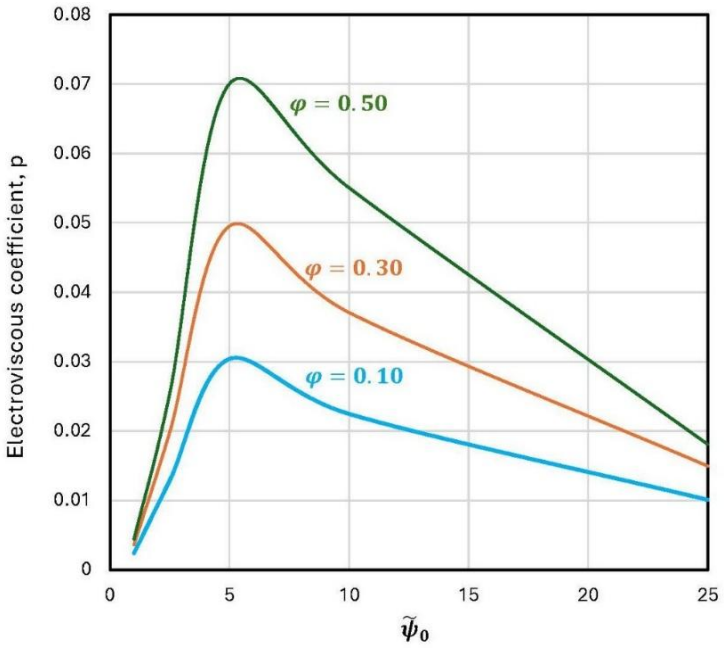

Figure 44. Variation of p with surface potential $\tilde{\psi}_0$ at different particle concentrations φ. The $R\kappa$ value is 30. The electrolyte is KCl.

There are no theoretical models available for the electroviscous coefficient p for concentrated emulsions. However, the scaling of η_r of concentrated emulsions could be readily achieved using the effective concentration of droplets defined as:

$$\varphi_{eff} = \varphi\left[1 + \frac{\delta}{R}\right]^3 \tag{86}$$

where δ is the thickness of the electrical double layer. The thickness of the double layer can be estimated using the intrinsic viscosity measurements of dilute emulsions [38]. For the van der Waarden emulsions of negatively charged oil droplets (see Figure 42), δ's estimated from intrinsic viscosity measurements are as follows: $\delta = 2.58$ nm for emulsions with droplet diameter of 205 nm, $\delta = 3.83$ nm for emulsions with droplet diameter of 102 nm, $\delta = 4.64$ nm for emulsions with droplet diameter of 58.5 nm, and $\delta = 3.63$ nm for emulsions with droplet diameter of 27.5 nm. In Figure 45, the data of Figure 42 is re-plotted as a function of effective volume fraction of droplets φ_{eff} given by Equation (86).

 doi:10.20944/preprints202603.0830.v1

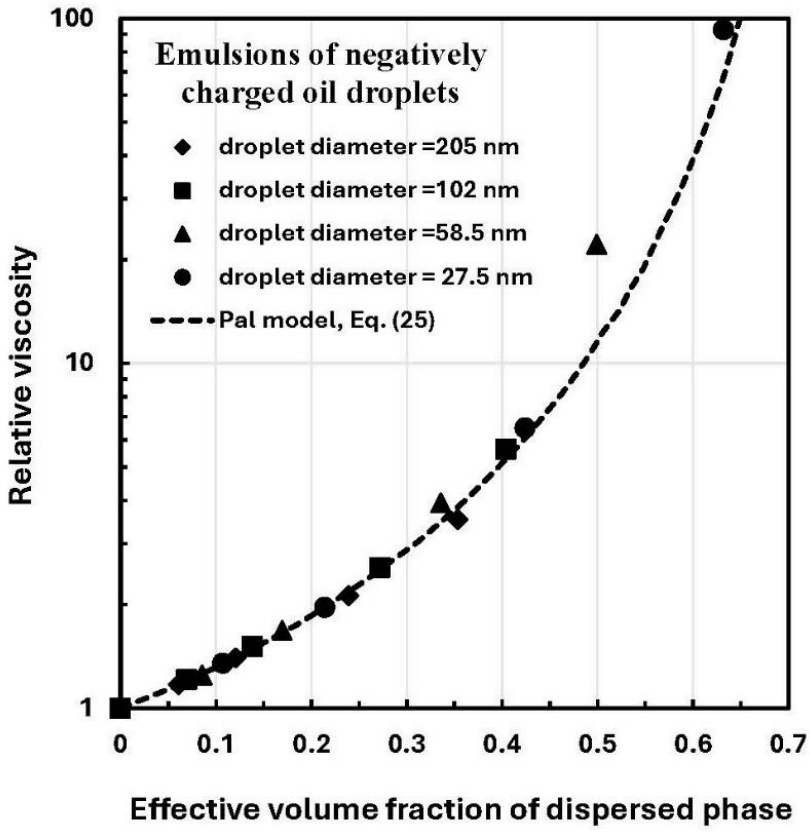

Figure 45. Scaling of η_r of electrically charged non-dilute oil-in-water emulsions with respect to φ_{eff}.

The data for all the emulsions of different droplet sizes overlap into a single curve confirming the scaling with of η_r with respect to φ_{eff} (instead of φ). Furthermore, the data is in excellent agreement with the predictions of the Pal model, Equation (25).

The Ohshimo model for concentrated suspensions addresses the effect of the "secondary electroviscous effect" only partially. However, at high concentration of particles, the electrical double layers of neighboring particles tend to overlap resulting in a much stronger "secondary electroviscous effect" than considered in the Ohshimo model. The suspension now becomes shear-thinning and even develops a yield stress [27].

When charged particles come close, they form doublets which rotate together and dissipate energy. Figure 46 shows the paths of two neighboring particles in flow [27,39,45]. The paths followed by electrically neutral particles are quite close as compared with the paths of the charged particles subjected to electrical repulsion. Note that the spatial distribution of particles at rest is determined by the balance of Brownian and electrostatic forces. When shear force is applied to the suspension, this microstructure is affected. The electrostatic repulsion force is larger than the viscous force at low shear rates and therefore, the radii of rotating doublets are quite large leading to high viscosities. The radii of doublets and hence the viscosity are reduced as the viscous force dominates over the electrostatic repulsion force at high shear rates.

 doi:10.20944/preprints202603.0830.v1

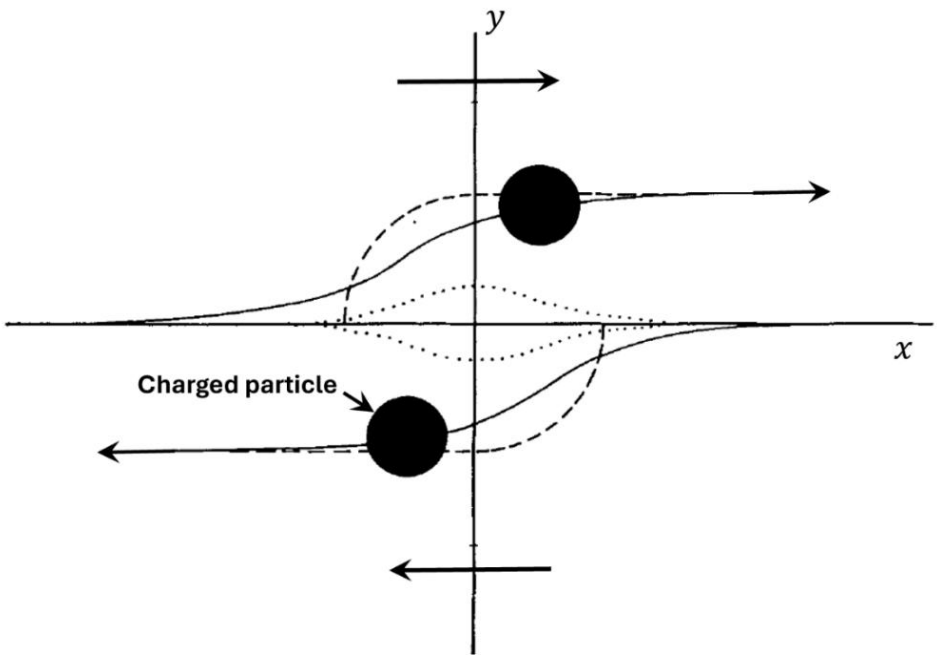

Figure 46. Trajectories of particles in flow; …. Uncharged particles with hydrodynamic interactions; ___ charged particles without hydrodynamic interactions; ----paths of charged particles according to Chan et al. [45]. Adapted from [39].

As an example, Figure 47 shows rheological behavior electrostatically stabilized O/W emulsions at $\varphi = 0.30$ [46]. The emulsions were stabilized by an anionic surfactant (sodium dodecyl benzene sulfonate, SDBS). The zeta potential of the droplets varied by varying the pH. With the increase in pH, the zeta potential and electrophoretic mobility of droplets increased, as shown in Figure 48 [46]. The emulsions are highly viscous and shear-thinning due to strong "secondary electroviscous effect". The electroviscous effect becomes stronger with the increase in pH due to an increase in zeta potential of the droplets.

Figure 49 shows another example of the viscous behavior of a concentrated electrostatically stabilized suspension. The φ of suspension is 0.425 [47]. The particles are strongly negatively charged, and the ionic strength of the suspension is controlled by the addition of electrolyte. The secondary electroviscous effect makes the suspension pseudoplastic. Furthermore, at low electrolyte concentration, suspension shows a yield stress as reflected in the upward bending of the viscosity versus shear stress plot. Viscosity decreases substantially when the electrolyte concentration increases due to reduction in the thickness of the electrical double layer.

 doi:10.20944/preprints202603.0830.v1

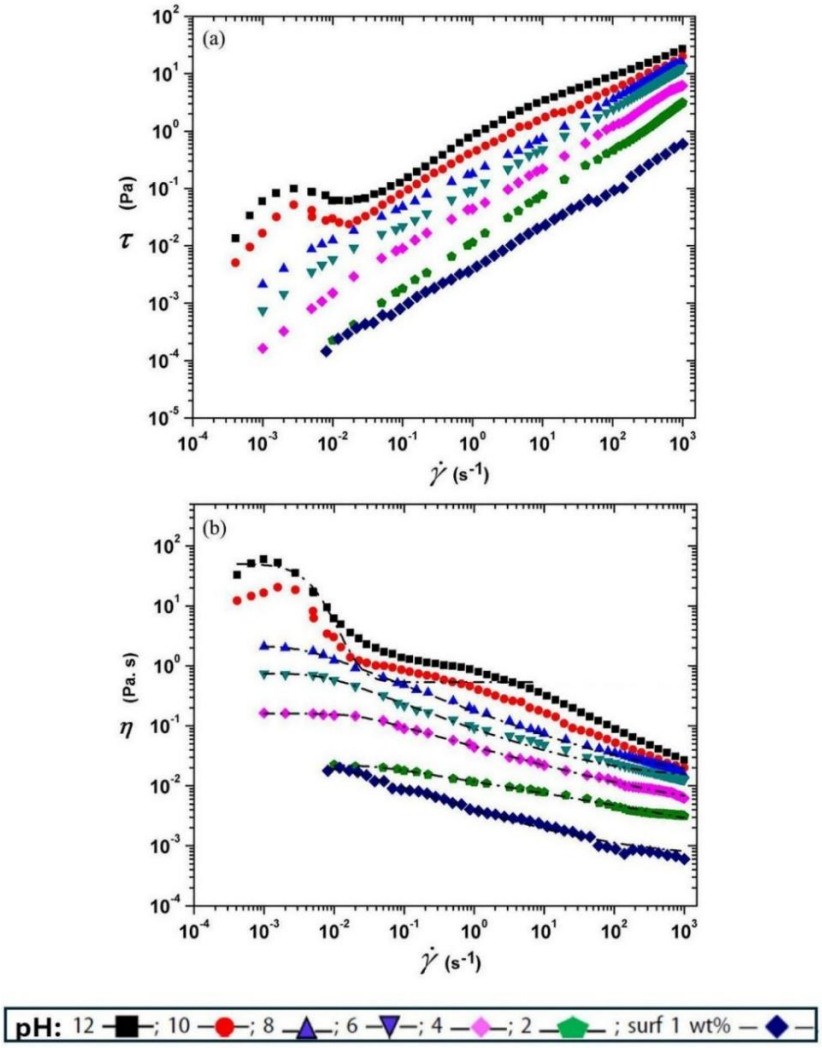

Figure 47. The evolution of flow curves of O/W emulsions with pH. Adapted from [46].

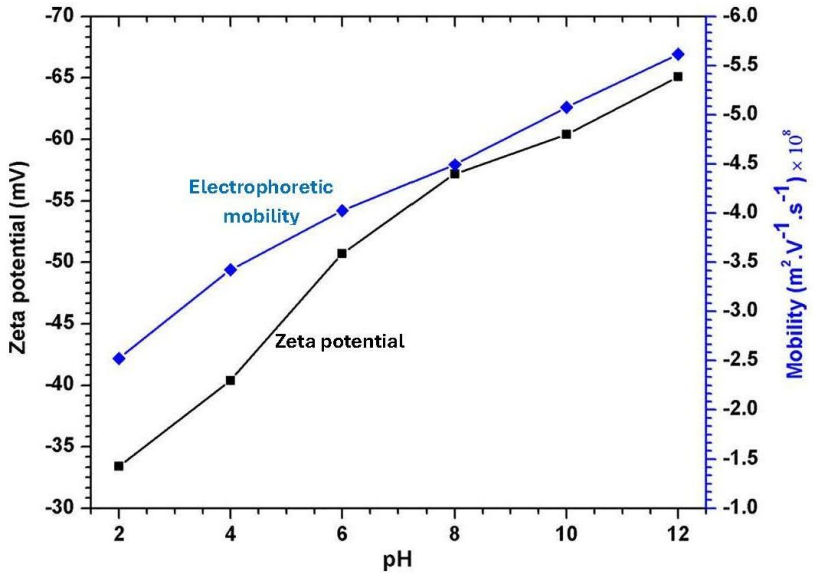

Figure 48. The variations of zeta potential and electrophoretic mobility of O/W emulsions with pH. Adapted from [46].

 doi:10.20944/preprints202603.0830.v1

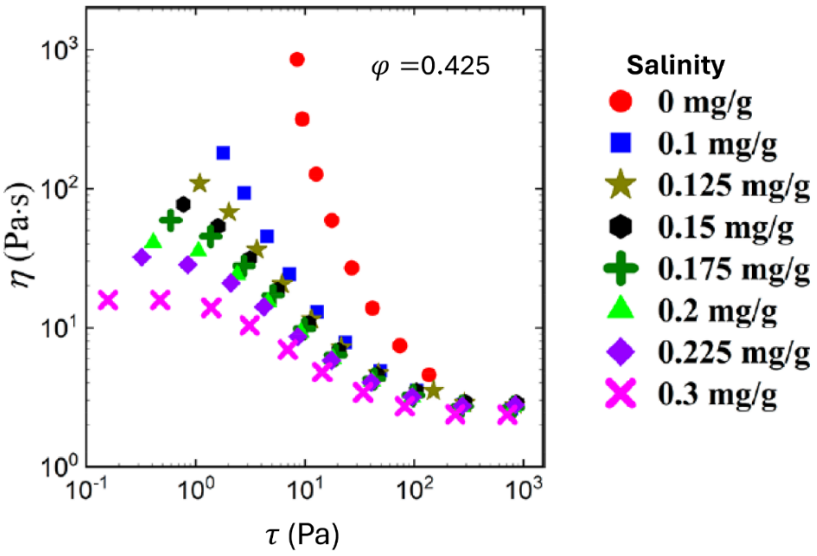

Figure 49. Viscous behavior of suspensions of charged particles at φ of 0.425. Adapted from [47].

Figure 50 shows η_r versus dimensionless shear stress for latex suspensions of charged particles at φ of 0.40 [48]. Once again, the electrostatically stabilized suspensions are pseudoplastic, and their viscosity decreases with the increase in electrolyte concentration due to the decrease in double layer thickness. The suspensions develop a yield stress when the electrolyte concentrations are low as reflected in the upward bending of viscosity versus shear stress plot.

The effect of φ on the η_r versus dimensionless shear stress data for latex suspensions of charged particles is shown in Figure 51 [48]. The suspensions exhibit pseudoplastic behavior even at a low φ of 0.05. The suspensions also develop a yield stress as reflected in the upward bending of viscosity versus dimensionless shear stress plot.

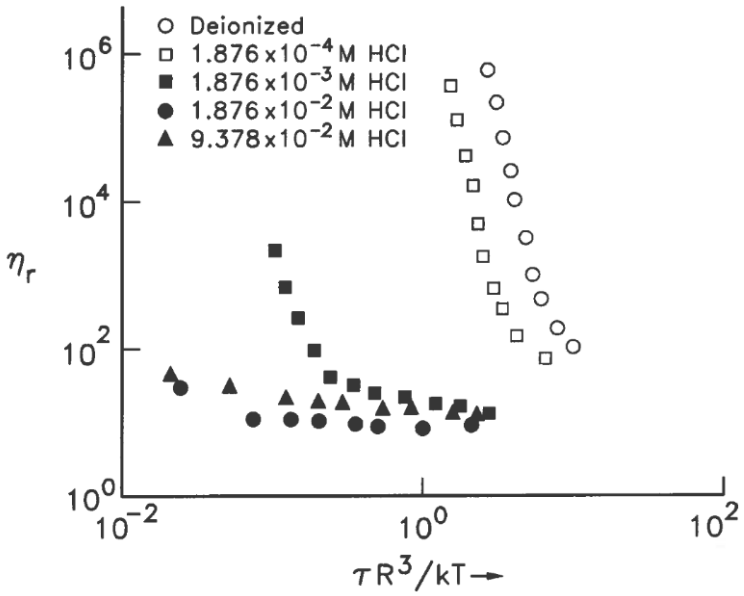

Figure 50. Viscous behavior of electrically charged suspensions at φ =0.40. Adapted from [48].

 doi:10.20944/preprints202603.0830.v1

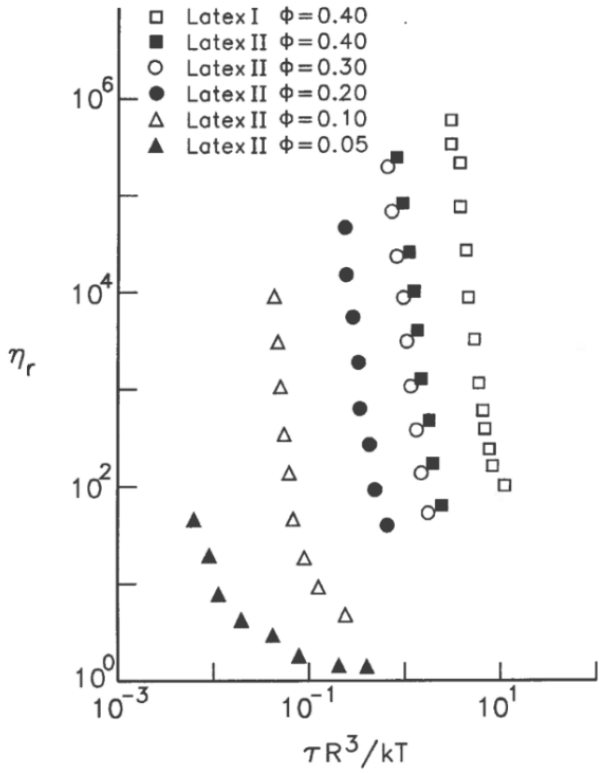

Figure 51. Viscous behavior of electrically charged suspensions at different values of φ. Adapted from [48].

Thus, the electrostatically stabilized suspensions are shear-thinning as well as develop yield stress at low electrolyte concentrations and high φ. The yield stress is due to overlapping of electrical double layers and crowding effect of particles (see Figure 52) [27].

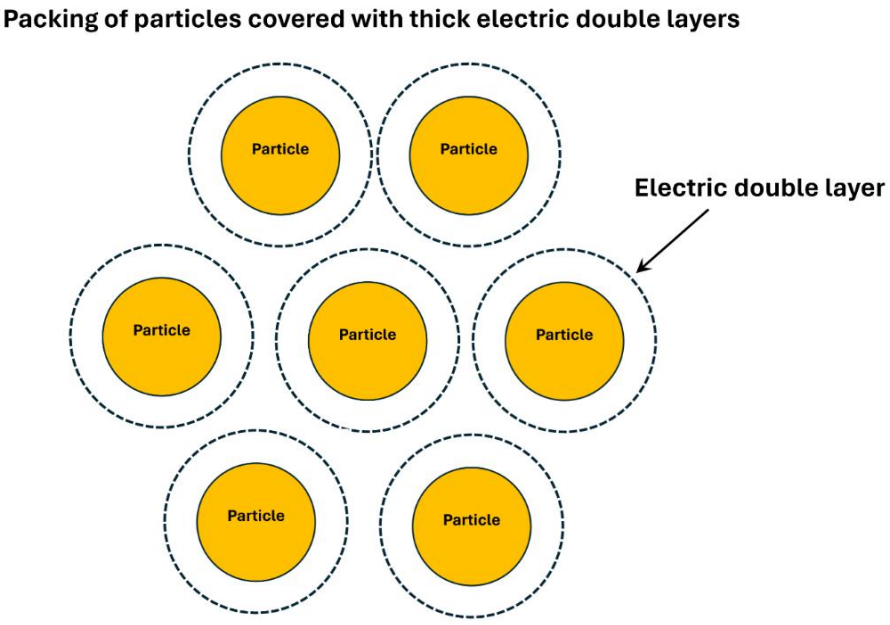

Figure 52. Merging electrical double layers of neighboring particles and crowding of particles at high φ.

Interestingly, the suspensions of electrically charged particles also exhibit strong shear-thickening at high φ close to φ_{max} (but less than φ_{max}) where overcrowding and jamming of particles occurs. As an example, Figures 53-54 show the viscous behaviour of non-dilute suspensions

 doi:10.20944/preprints202603.0830.v1

of charged silica particles [27,49]. The suspensions exhibit shear-thickening behaviour, that is, the viscosity rises sharply when the shear rate is increased. At high φ, a discontinuity in viscosity versus shear rate plots is also observed (see Figure 54).

It is not clear under what conditions do electrostatically stabilized suspensions exhibit yield stress and under what conditions do they exhibit shear-thickening. It appears that suspensions with moderate volume fractions but thick electrical double layers (large δ/R) tend to exhibit yield-stress behavior whereas suspensions at high volume fractions (but still significantly less than φ_{max}) with relatively thin double layers (small δ/R) exhibit shear-thickening. However, as packed bed volume fraction φ_{max} is approached, the stable suspensions coated with thin stabilizing layers almost always possess yield-stress with or without any shear-thickening behavior. This point is illustrated in Figure 55 where cornstarch suspensions exhibit shear-thickening behavior up until $\varphi = 0.469$ without any yield stress [50]. For $\varphi \geq 0.477,$ the suspensions possess both yield-stress and shear-thickening behavior. Note that the starch particles are not spherical and therefore, the $\varphi_{max}$of starch suspensions is expected to be lower in comparison with the spherical particles.

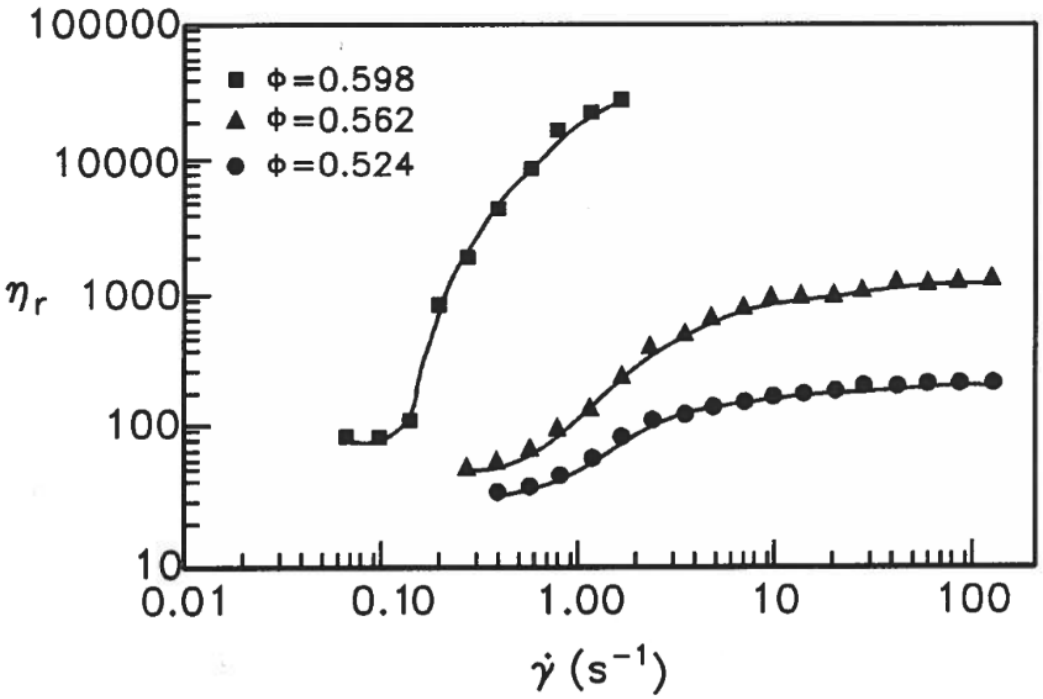

Figure 53. Viscous behaviour of suspensions of electrically charged particles. Adapted from [49].

 doi:10.20944/preprints202603.0830.v1

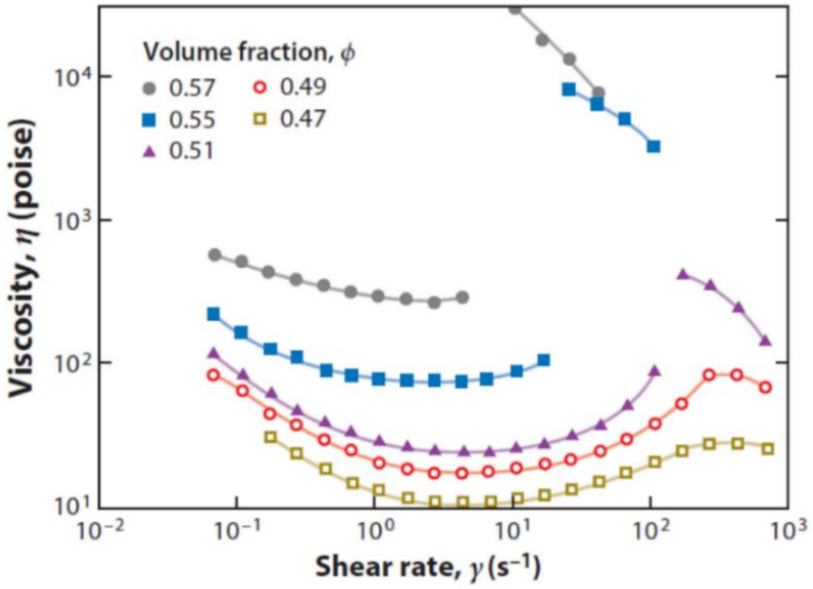

Figure 54. Shear thickening in suspensions of electrically charged particles at high φ. Adapted from [49].

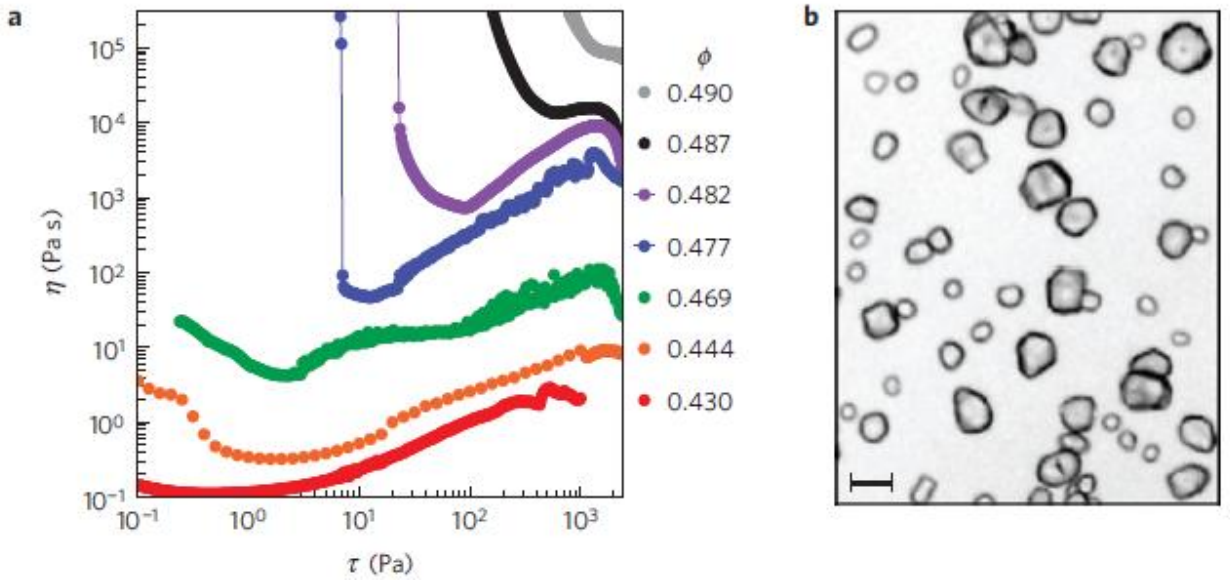

Figure 55. Yield-stress and shear-thickening in suspensions. a) Viscosity curves for cornstarch in water at different φ. The cornstarch particles had an average diameter of 14 μm. b) The microscope image of corn starch particles indicating the absence of clustering of particles. Adapted from [50].

6. Influence of Steric Effects on the Rheology of Non-Dilute Emulsions

The presence of an adsorbed layer of surfactant and/or polymer on the surface of the droplets (see Figure 56) can have a significant effect on the rheology of emulsion [27]. Such emulsions, referred to as sterically stabilized systems, are generally shear-thinning in nature.

 doi:10.20944/preprints202603.0830.v1

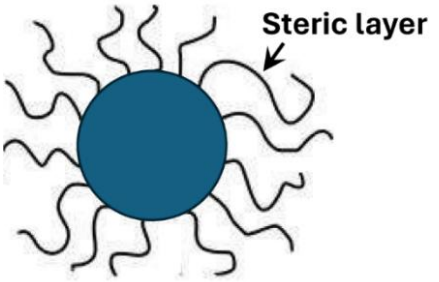

Figure 56. Droplet covered by a steric layer.

Consider the close approach of two neighboring droplets with adsorbed layers of surfactant/polymer of thickness δ (see Figure 57). When $b \gg 2\delta$, there is no steric interaction between the droplets. However, a strong steric interaction occurs between the droplets when $b < 2\delta$ due to overlapping and interpenetration of the adsorbed layers. The steric interaction is of two types: mixing (osmotic) interaction and entropic interaction. If the matrix fluid is a good solvent for the adsorbed surfactant/polymer chains, the mixing or interpenetration of adsorbed layers is thermodynamically unfavored, resulting of repulsion between the droplets. If the matrix fluid is a poor solvent for the adsorbed layers, the mixing/interpenetration of adsorbed layers is thermodynamically favored, resulting in the attraction of droplets. When $b < \delta$, the adsorbed material (for example, polymer chains) is compressed and there is a loss in configuration entropy of the adsorbed molecules. This elastic or entropic interaction causes repulsion between the droplets. The total free energy of interaction between two droplets covered with adsorbed layers is given as [51]:

$$G_{interaction} = G_{vdw} + G_{mix} + G_{entropy} \quad (87)$$

where vdw refers to van der Waals interaction.

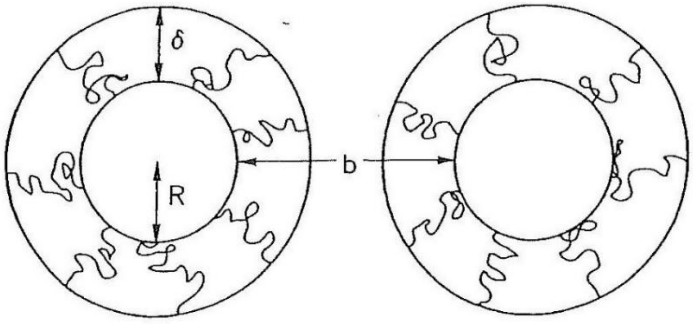

Figure 57. Interaction between droplets covered by steric layers.

The presence of an adsorbed layer of thickness δ increases the effective φ of the droplets in accordance with Equation (86). An increase in the effective φ of the droplets in turn increases the viscosity of emulsion. The sterically stabilized emulsion with small droplets and a thick layer of adsorbed layer is expected to exhibit much higher viscosity as compared with the emulsion of large droplets and thin adsorbed layers.

Figure 58 shows the viscous behavior of sterically stabilized suspensions at different values of φ [52]. The radius of the particles was 80 nm and were coated with a thick layer (60 nm) of end grafted PDMS (polydimethylsiloxane). The actual φ (without steric layer) was quite low, approximately in the range of 0.02 to 0.15. However, the effective φ estimated from Equation (86) varied from 0.12 to 0.81. As expected, the suspensions of sterically stabilized suspensions at high effective φ are generally pseudoplastic with a Newtonian plateau at low shear rates. However, at $\varphi_{eff} > 0.60$, the Newtonian plateau at low shear rates disappears indicating the appearance of

 doi:10.20944/preprints202603.0830.v1

yield stress. The cause of yield-stress in sterically stabilized suspensions is the overlapping of thick steric layers and crowding effect of particles as illustrated schematically in Figure 59.

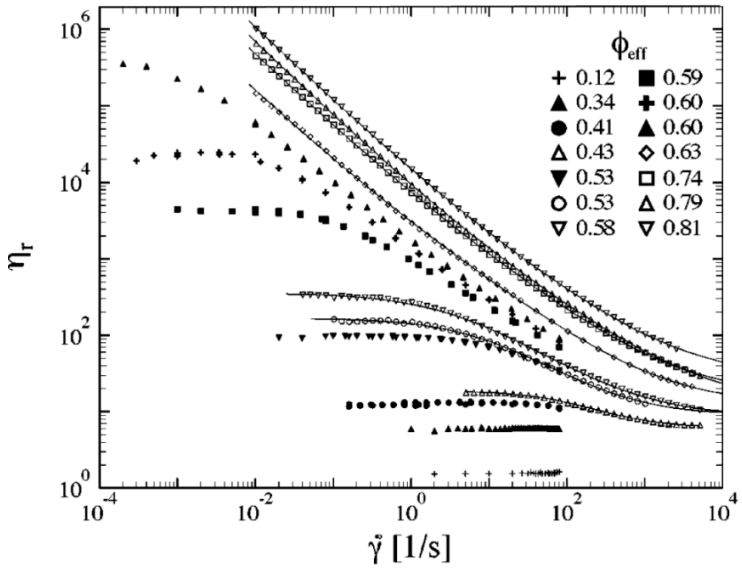

Figure 58. Viscous behavior of sterically stabilized suspensions at different values of φ. Adapted from [52].

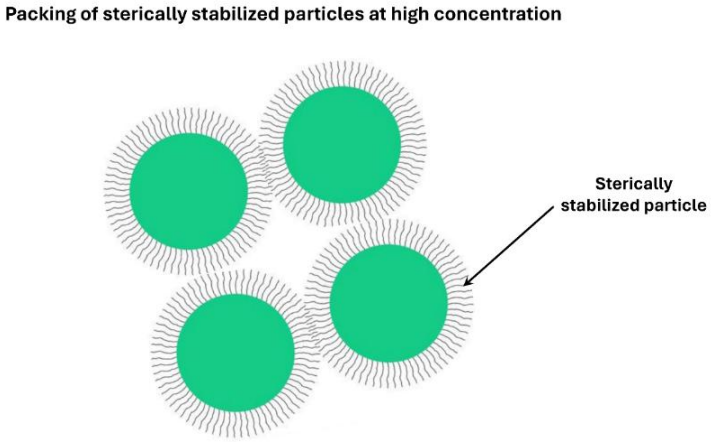

Figure 59. Merging of steric layers of neighboring particles and crowding of particles at high φ.

The sterically stabilized suspensions exhibit shear-thickening under certain conditions. Figure 60 shows an example of shear-thickening observed in sterically stabilized suspensions [53]. With the increase in shear stress, a region of nearly constant shear rate develops at high stresses. The discontinuity in shear rate is reflective of shear-thickening behavior of suspension.

 doi:10.20944/preprints202603.0830.v1

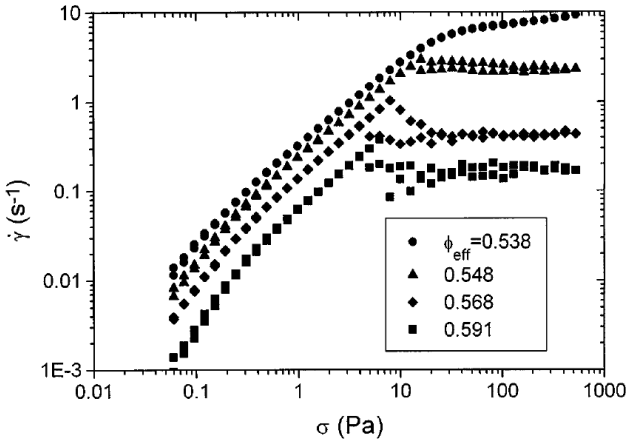

Figure 60. Shear thickening in suspensions of PMMA particles at different volume fractions. The particles are sterically stabilized. Adapted from [53].

Note that the thickness of steric layers of sterically stabilized suspensions shown in Figure 60 is relatively small, that is, δ/R is approximately 0.026 $(= 9nm/345\,nm)$. For sterically stabilized suspensions with large δ/R, yield-stress behavior is expected at relatively low φ. Thus, to observe shear-thickening in suspensions (electrostatically or sterically stabilized), the following conditions are favorable: repulsive particles (electrically charged or sterically stabilized), thin layer of double layer or steric layer compared with particle radius, high volume fraction of particles.

Interestingly, emulsions of deformable liquid droplets do not exhibit any shear-thickening. The inclusions must be rigid particles for shear-thickening to appear. Particle roughness also plays a role. Suspension of rough particles is more prone to shear-thickening. Figure 61 shows some shear-thickening effect in concentrated emulsions when the droplets are covered by a steric layer of solid nanoparticles [54]. The droplets covered by a steric layer of solid nanoparticles (see Figure 62), referred to as Pickering droplets, behave more like rigid particles [55].

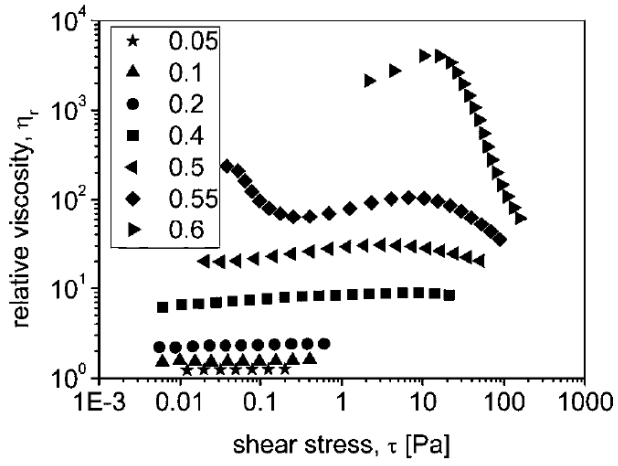

Figure 61. Viscous behavior of Pickering emulsions at φ. Adapted from [54].

 doi:10.20944/preprints202603.0830.v1

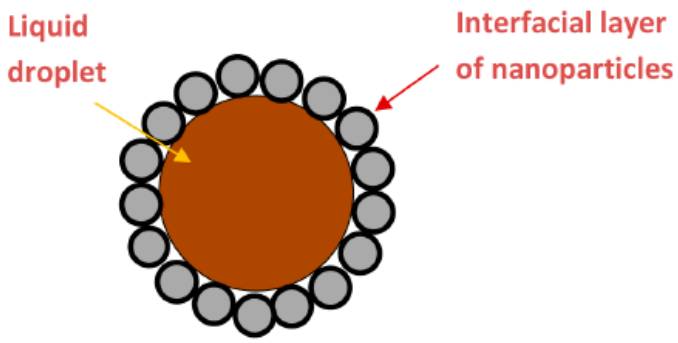

Figure 62. Pickering droplet. .

7. Rheology of Flocculated Emulsions

Flocculation of droplets induces non-Newtonian pseudoplastic behaviour of emulsions. The flocculated emulsions also possess yield-stress at high volume fractions of particles. The flocculation of droplets can be induced by different mechanisms: 1) removal or suppression of stabilizing layer (steric or electrical double layer) present on the droplet surfaces; 2) introduction of Brownian forces; 3) introduction of depletion forces; and 4) promotion of bridging of droplets.

Figure 63 shows the viscosity changes that occur when sterically stabilized particles of a suspension are made attractive by suppression of the steric layer [56]. The particles of the suspension were covered by octadecyl chains forming a steric layer. The temperature of suspension was varied to suppress the steric layer by altering the solvency of the suspending medium. The suppression of the steric layer by decreasing the temperature increased attraction between the particles resulting in flocculation of particles. Consequently, the suspension becomes pseudoplastic. The suspension could also develop yield-stress.

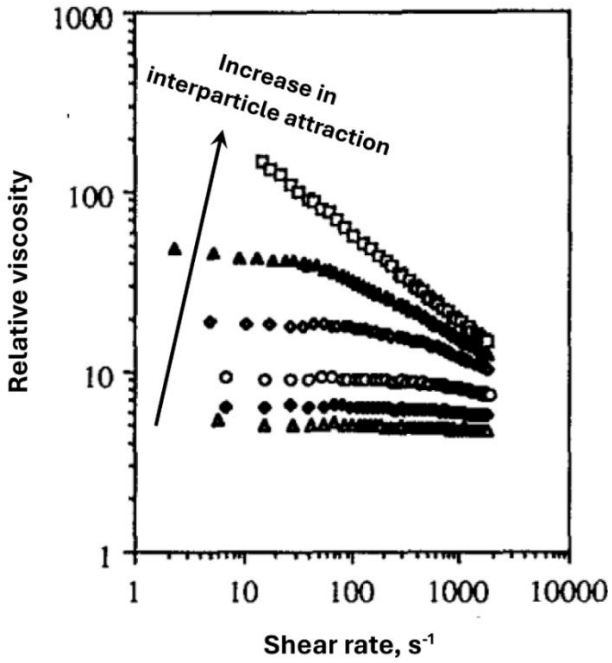

Figure 63. The effect of increasing interparticle attraction on the viscous behavior of a suspension. Adapted from [56].

Figure 64 shows the relative viscosity plots of sterically stabilized suspensions of PVC particles at a φ of 0.20 [57,58]. In this case, flocculation of particles is induced by changing the solvency of

 doi:10.20944/preprints202603.0830.v1

adsorbed steric layer in the dispersion medium. The quality of the solvent for steric polymer layer can be characterized in terms the Flory-Huggins interaction parameter (χ). For good solvents, $\chi < 0.5$ whereas for poor solvents, $\chi > 0.5$. For neutral theta solvent, $\chi \approx 0.5$. Figure 64 shows that the suspension becomes highly viscous and pseudoplastic when the solvent quality of the steric layer is changed from good solvent to poor solvent. The suspension is highly flocculated when the solvent for the steric layer is poor.

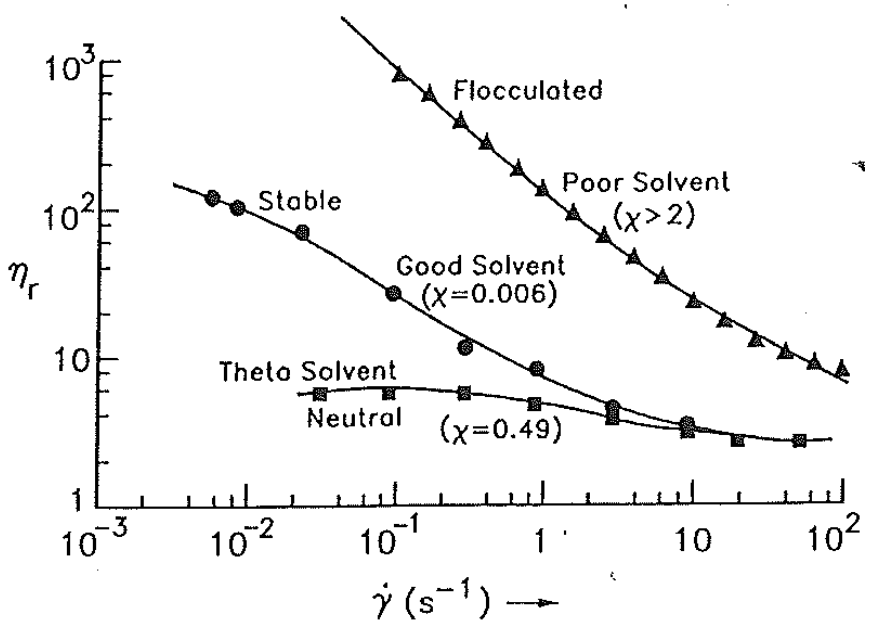

Figure 64. The influence of solvent quality on the steric layer, and hence the relative viscosity, on the sterically stabilized suspension where χ is Flory-Huggins interaction parameter. Adapted from [57,58].

The effect of Brownian motion on the rheology of dispersions (suspensions and emulsions) is strong when the size of the droplets/particles is in the submicron or nanometer range [57–60]. Assuming that the inclusions are "hard spheres" with thin stabilizing layers (steric or electrical double layer), the rheology of such dispersions is governed by hydrodynamic and Brownian forces. The rheological equation of state of Brownian dispersions under steady state can be expressed as:

$$\eta = f(\dot{\gamma}, \eta_c, R, n, \rho_d, \rho_c, kT) \tag{88}$$

where $\dot{\gamma}$ is the shear rate, η_c is the continuous-phase viscosity, R is the radius of inclusion (particle or droplet), n is the number density of inclusions, ρ_d, ρ_c are densities of dispersed and continuous phases, k is the Boltzmann constant, and T is the absolute temperature. Equation (88) could be written in dimensionless form as:

$$\eta_r = f\left(\varphi, \rho_r, N_{Pe}, N_{Re,p}\right) \tag{89}$$

where ρ_r is the relative density $(= \rho_d/\rho_c)$ and N_{Pe} is the Peclet number defined as:

$$N_{Pe} = \frac{\dot{\gamma}\eta R^3}{kT} = \frac{\tau R^3}{kT} \tag{90}$$

where τ is the shear stress. Assuming neutrally buoyant particles ($\rho_r \to 1$) and creeping flow ($N_{Re,p} \to 0$), Equation (89) reduces to:

$$\eta_r = f(\varphi, N_{Pe}) \tag{91}$$

 doi:10.20944/preprints202603.0830.v1

Thus, the relative viscosity of different hard-sphere type dispersions (emulsions / suspensions) is a function of volume fraction of particles and Peclet number. Consequently, dispersions of different size inclusions but same φ and N_{Pe} have the same relative viscosity.

Figures 65 and 66 show the viscous behaviours for latex 141 suspensions in bromoform and latex 84 suspensions in bromoform, respectively. The hydrodynamic radii of latex particles are 141 nm for latex 141 suspensions and 84 nm for latex 84 suspensions. As both dispersions are Brownian, they exhibit strong pseudoplastic behavior. The flow curves of Brownian suspensions at any φ can be described as [60]:

$$(\eta - \eta_\infty)/(\eta_0 - \eta_\infty) = [1 + (\tau/\tau_{crit})]^{-1} \quad (92)$$

where η_0 and η_∞ are zero-shear and infinite-shear limiting viscosities, respectively, τ is shear stress and τ_{crit} is critical shear stress at which $\eta = (\eta_0 + \eta_\infty)/2$.

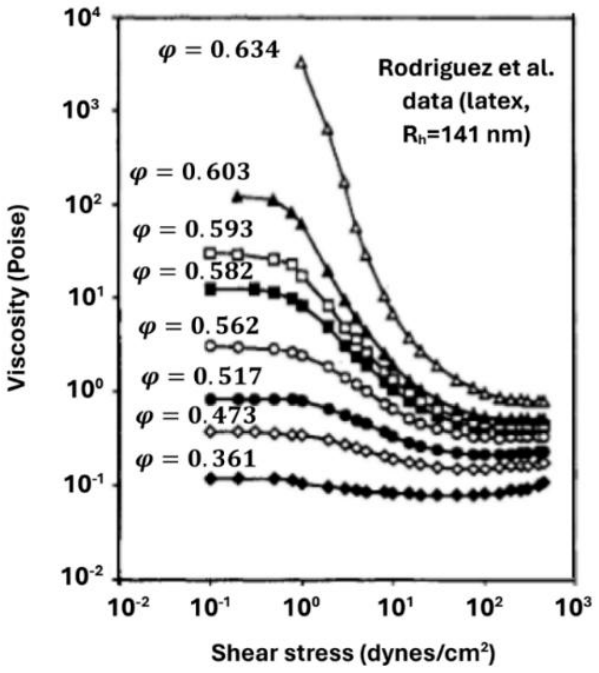

Figure 65. Viscous behavior of non-dilute Brownian suspensions of latex 141. Adapted from [60].

 doi:10.20944/preprints202603.0830.v1

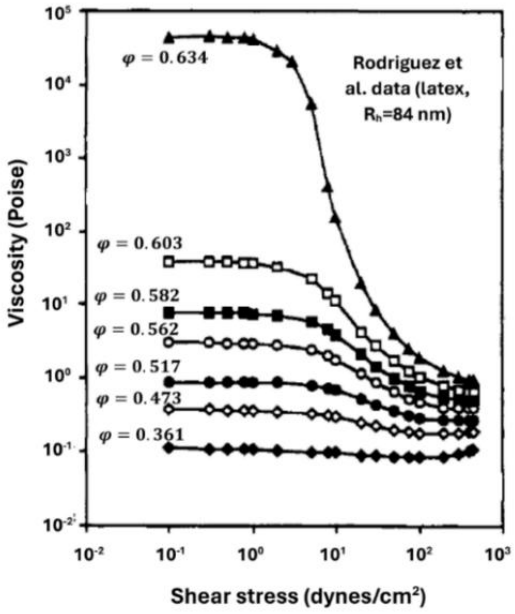

Figure 66. Viscous behavior of Brownian suspensions of latex 84. Adapted from [60].

Figure 67 shows the superposition of the latex suspension data of different size particles. Clearly, the η_r versus Peclet number N_{Pe} plots for different sized latex suspensions overlap at the same volume fraction of particles.

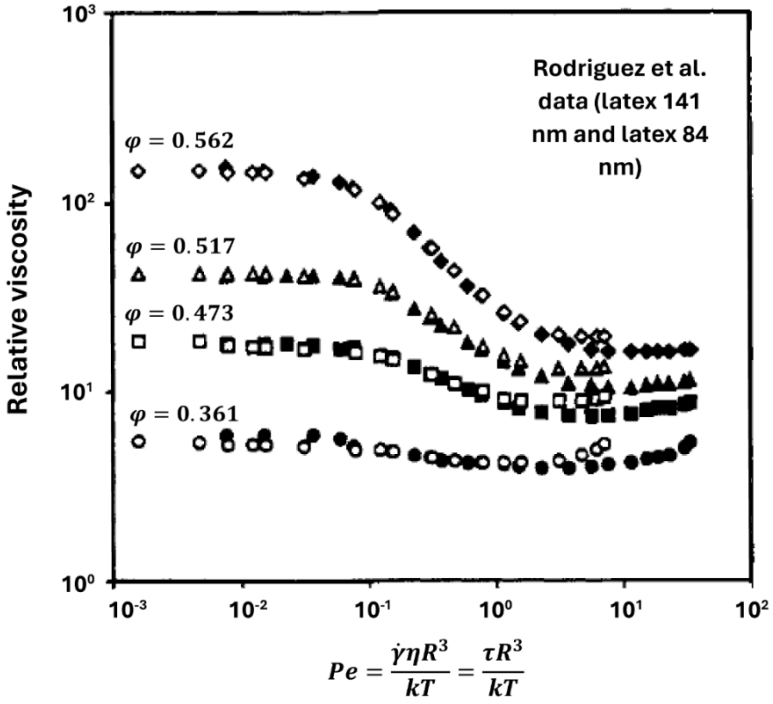

Figure 67. Plots of η_r versus N_{Pe} for Brownian suspensions at different values of φ. Adapted from [60].

Figure 68 shows another example of the superposition η_r versus N_{Pe} data for Brownian suspensions of different particle sizes and different dispersion mediums at a fixed $\varphi = 0.50$. The data covers suspensions of particle sizes ranging from 77 nm to 314 nm. Clearly, the scaling of data η_r versus N_{Pe} basis is excellent.

 doi:10.20944/preprints202603.0830.v1

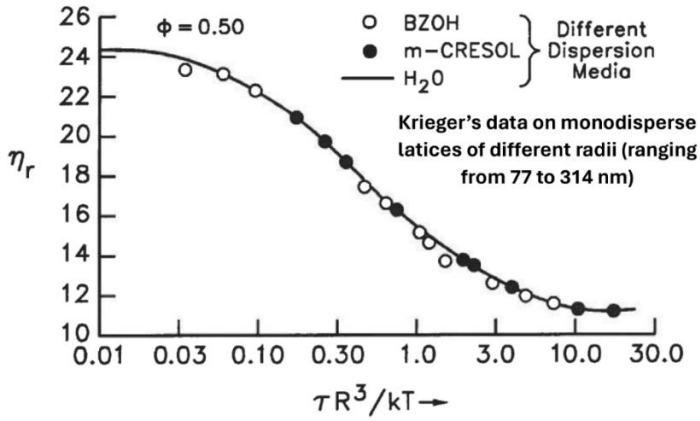

Figure 68. η_r versus N_{Pe} for Brownian suspensions. Adapted from [59].

Note that at high φ ($\varphi > 0.60$), close to φ_{max}, suspensions of Brownian hard spheres develop a yield stress due to crowding of particles [27,61]. The presence of yield stress in the suspension at high φ is indicated by an upward bend of viscosity versus shear stress plot.

Depletion flocculation of droplets/particles is induced by the addition of "free" polymer macromolecules or micelles to the dispersion medium [51,62–68] of emulsion/suspension. When the particles of a dispersion approach each other close enough to distances smaller than the size of polymer molecule or surfactant micelle, the polymer molecules or surfactant micelles present in the dispersion medium are forced out of the interparticle space (see Figure 69). This creates a polymer or micelle free (depleted) zone between the particles. As the concentration of polymer or micelles outside the interparticle space is not zero, an inward osmotic force is generated on the particles (see Figure 69) resulting in clustering of particles. Figure 69 shows depletion flocculation caused by polymer molecules whereas Figure 70 shows depletion flocculation caused by micelles.

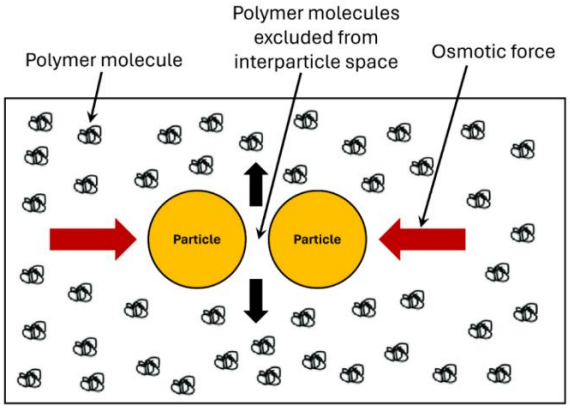

Figure 69. Flocculation of particles caused by polymer induced depletion.

 doi:10.20944/preprints202603.0830.v1

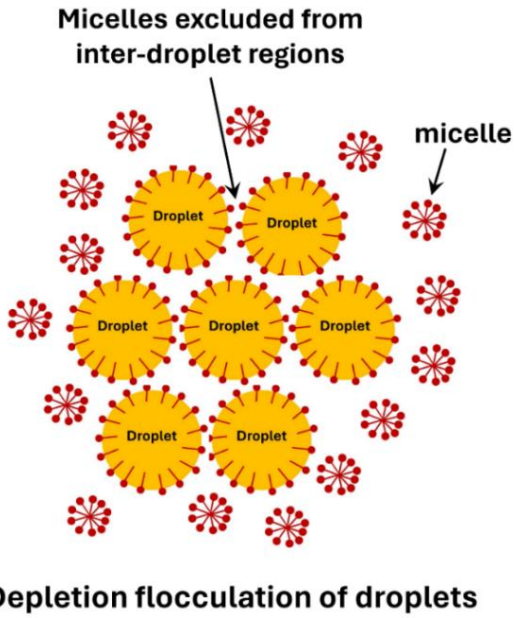

Figure 70. Flocculation of droplets caused by micelle induced depletion.

The flow curves (η versus τ plots) of depletion-flocculated emulsions are shown in Figure 71. The flocculation of emulsion was caused by surfactant micelles [69]. The emulsions are highly shear-thinning and flocculated (see Figure 72).

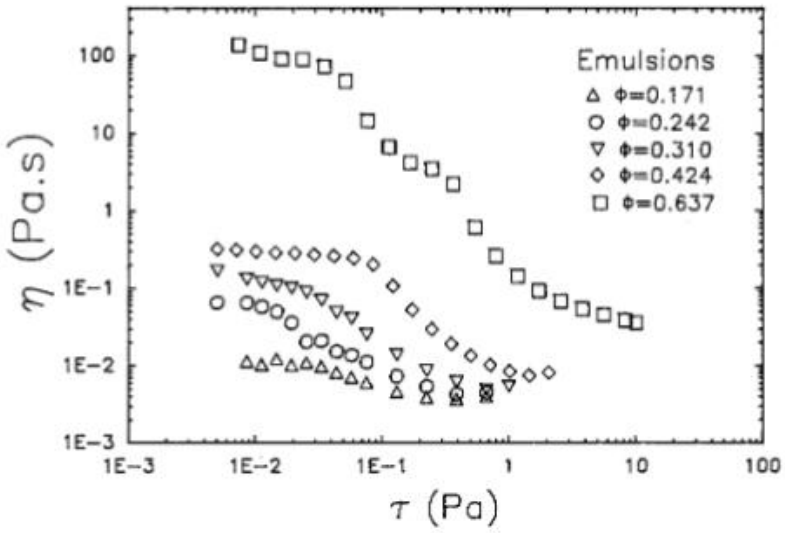

Figure 71. Viscous behavior of micelle-induced depletion-flocculated emulsions. Adapted from [69].

Figure 73 shows another example of depletion-flocculated emulsions. The emulsions are water-in-oil (W/O) type, and the φ is fixed at 0.29 [65]. The emulsions become shear-thinning as the surfactant concentration is increased due to depletion flocculation of water droplets (see Figure 74) caused by micelles.

 doi:10.20944/preprints202603.0830.v1

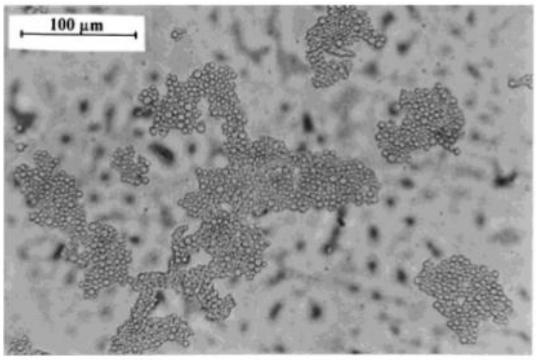

Figure 72. Aggregation of oil droplets caused by micelle-induced depletion.

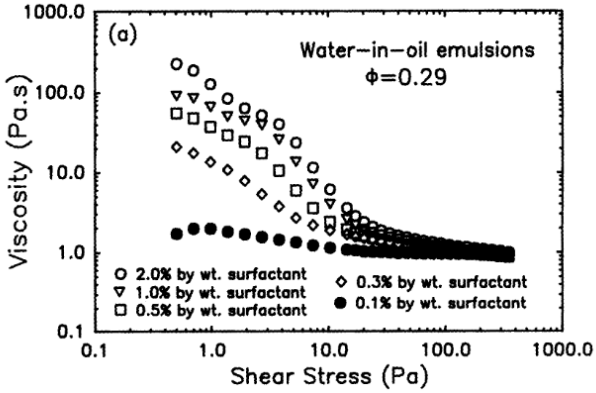

Figure 73. Viscous behavior of micelle induced depletion-flocculated emulsions at different surfactant concentrations. .

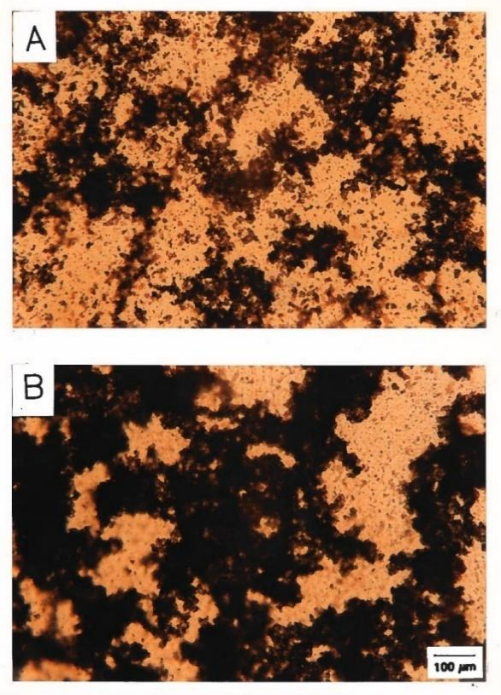

Figure 74. Flocculation of water droplets caused by micelle-induced depletion emulsion.

 doi:10.20944/preprints202603.0830.v1

Jansen et al. [66] have presented a theoretical analysis of correlation of relative viscosity for depletion-flocculated emulsions caused by surfactant micelles. According to them, the relative viscosity could be scaled adequately using the so-called "depletion flow number" (N_{df}) defined as:

$$N_{df} = \frac{4\pi\eta_c\dot{\gamma}R^2R_m}{kT\phi_m} \quad (93)$$

where R_m is micelle radius, and ϕ_m is volume fraction of micelles. N_{df} is the ratio of viscous energy needed to separate the droplets to the depletion energy that opposes this separation.

Figure 75 demonstrates the scaling of emulsion relative viscosity on depletion flow number basis. In Figure 75(a), the η_r versus $\dot{\gamma}$ plots are shown for depletion-flocculated W/O emulsions at different surfactant concentrations. At any given $\dot{\gamma}$, the relative viscosity increases with the increase in surfactant concentration. The same data are scaled on depletion flow number basis in Figure 75(b). The relative viscosity curves generally superpose when plotted against the depletion flow number. The only exception occurs for the highest surfactant concentration which falls slightly higher than the rest.

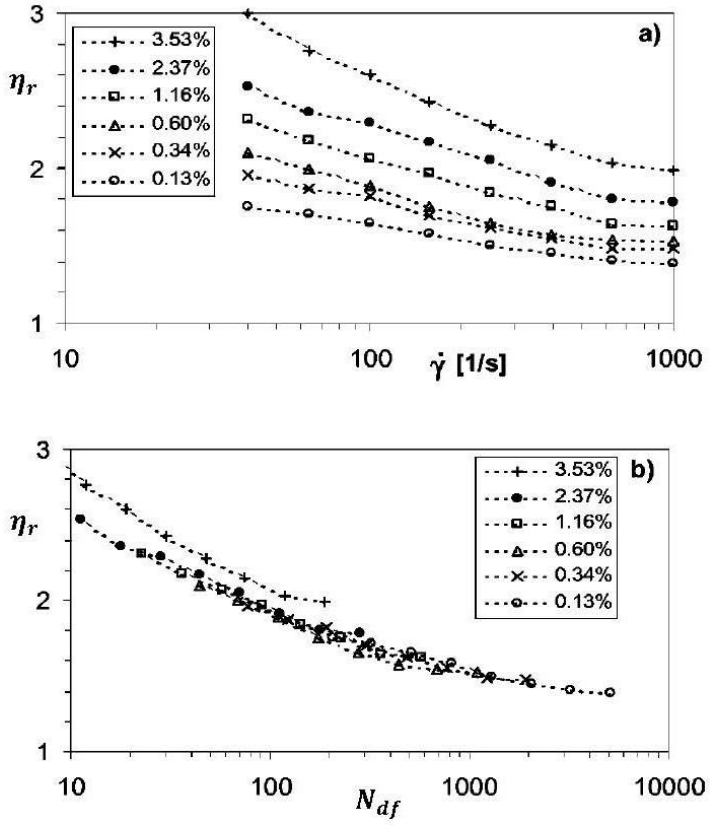

Figure 75. Effect of surfactant concentration on the relative viscosity of a W/O emulsion. a) η_r versus shear rate. b) η_r versus depletion flow number N_{df}. The numbers in the plots indicate volume fractions of surfactant (sorbitan monostearate). The value of φ is 0.15 and the Sauter mean diameter of emulsions is 3 μm. Adapted from [66].

Depletion flocculation could also be caused by the addition of excess or free protein in the dispersion medium. Figures 76-77 show the flow curves for emulsions flocculated by protein (sodium caseinate). The φ is 0.35 in Figure 76 [67] and 0.45 in Figure 77 [68] and the protein concentration is increased. As the protein concentration of the aqueous phase is increased, the emulsions become non-Newtonian pseudoplastic due to depletion flocculation of droplets.

 doi:10.20944/preprints202603.0830.v1

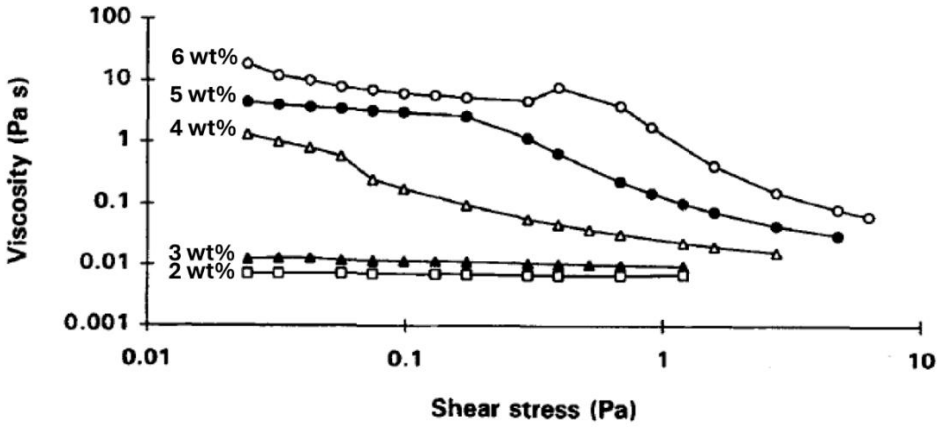

Figure 76. Pseudoplastic behavior of protein flocculated emulsion at different protein concentrations. (35 vol% n-tetradecane, pH 6.8, 30 °C). Adapted from [67].

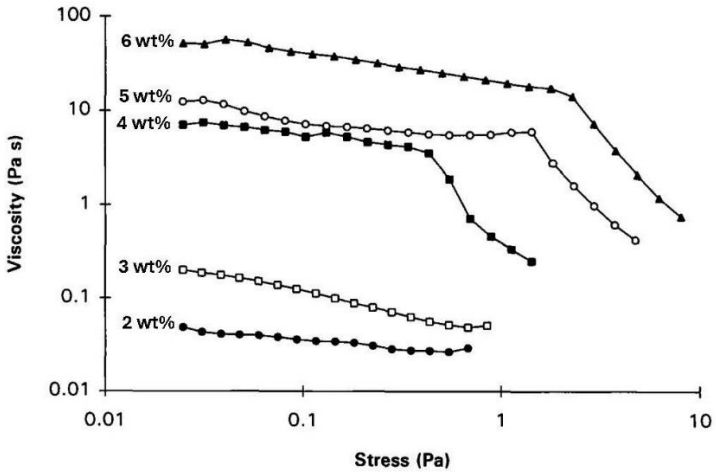

Figure 77. Effect of protein content on viscosity of depletion-flocculated O/W emulsions (45 vol% n-tetradecane, pH 6.8, 30 °C). Adapted from [68].

Flocculation of inclusions could also occur by a bridging mechanism. Bridging flocculation of inclusions occurs when the polymer present in the continuous phase fluid of the dispersion is adsorbing type [51,70]. Bridging of particles can occur in two ways as shown schematically in Figure 78. In Figure 78(a), bridging occurs when segments of the same polymer molecule adsorb onto different particles whereas in Figure 78(b), bridging of particles occur by entanglement of different polymer molecules adsorbed on to different particles.

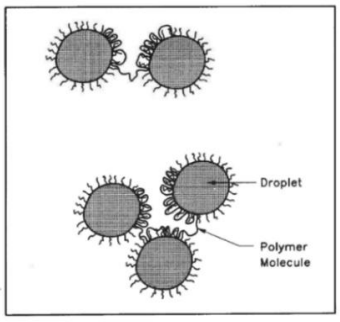

Figure 78. a). Bridging flocculation caused by the same polymer molecule adsorbed on two or more droplets/particles.

 doi:10.20944/preprints202603.0830.v1

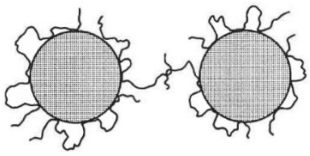

Figure 78. b). Bridging flocculation caused by entanglement of different adsorbed polymer molecules.

Figure 79 shows the viscous behavior of concentrated suspensions with adsorbing type polymer included in the suspending medium [70]. The polymer is polyacrylic acid (PAA) present at a concentration of 1wt%. The diameter of the particles is 80 nm. The suspensions are nearly Newtonian or slightly pseudoplastic up to a critical shear rate. However, a rapid rise in viscosity occurs above the critical value indicating shear-thickening behavior. After a sharp rise in viscosity, the viscosity decreases with further increase in shear rate.

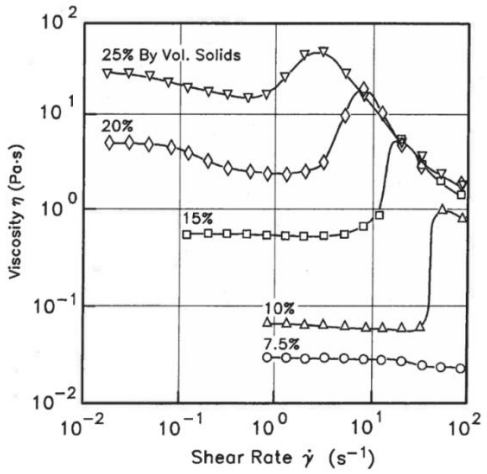

Figure 79. Viscosity versus shear rate curves for non-dilute suspensions in the presence of polymer in the suspending medium. Adapted from [70].

The shear-thickening behaviour observed in Figure 79 is caused by polymer bridging flocculation of particles. In the low shear rate region, an equilibrium exists between formation of polymer bridges between particles and their break-up resulting in nearly Newtonian behaviour of suspension. The break-up of polymer bridges is caused by thermal energy especially when the polymer is not strongly adsorbed on the particle surface. Thus, the polymer bridging between the particles is reversible when the polymer does not adsorb strongly on the particle surface. Shear-thickening in these suspensions is caused by rapid stretching of polymer chains. When polymer macromolecules are rapidly elongated, the restoring force of bridges increases the resistance to flow and hence a rise in viscosity occurs. However, at high shear rates, the bridges undergo breakup resulting in pseudoplastic behaviour.

Note that when the polymer is strongly adsorbing type, the polymer bridges formed between the particles are irreversible in nature. In this case, the suspension shows a hysteresis effect. For example, Figure 80 shows the viscosity versus shear rate plots of suspensions containing a strongly adsorbing type of polymer. The suspension behaves like a pseudoplastic fluid until the critical shear rate is reached. The viscosity rises sharply at some critical shear rate. This abrupt increase in viscosity occurs due to shear-induced bridging of particles. The suspensions also show hysteresis effect as the bridging of particles by polymer molecules is irreversible. In other words, the suspension viscosities do not return to the initial values when the shear rate is lowered to values below the critical shear rate. The viscosities remain high even when the shear rate is lowered below the critical value.

 doi:10.20944/preprints202603.0830.v1

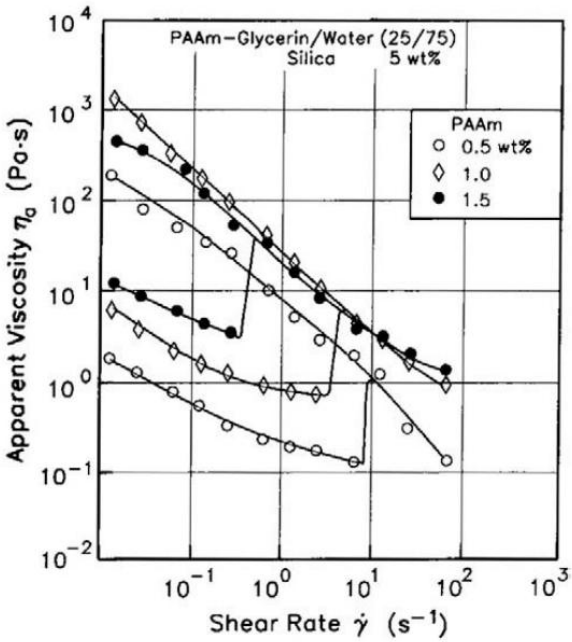

Figure 80. Viscous behavior of suspensions at different polymer concentrations keeping the particle concentration fixed at 5 wt% silica. Adapted from [70].

When surfactant is added to the suspension flocculated by polymer bridges, preferential adsorption of surfactant on the particle surface occurs resulting in breakup of polymer bridges. As an example, Figure 81 shows the influence of surfactant addition to the suspension flocculated by polymer bridges [70]. At a high surfactant concentration of 2 wt%, all the polymer bridges are disrupted, and the suspension loses its shear-thickening behavior.

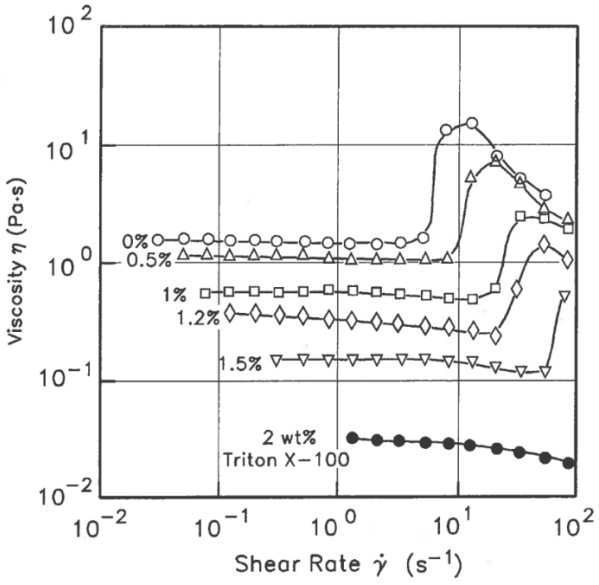

Figure 81. Influence of surfactant on the rheological behavior of suspension flocculated by polymer bridges. The φ is 0.15 and the polymer is polyacrylic acid at a concentration of 2 wt%. Adapted from [70].

Figure 82 shows the viscous behavior of emulsions flocculated by protein (sodium caseinate) bridging [68]. The adsorption and bridging of droplets by protein is a slow process. The flow curve shifts upward to higher viscosities as the emulsion ages. With aging, the number of protein bridges between the droplets increases causing an increase in viscosity. However, no shear-thickening

 doi:10.20944/preprints202603.0830.v1

behavior is observed. It seems that the bridges undergo breakup with the increase in shear rate resulting in shear-thinning of emulsions.

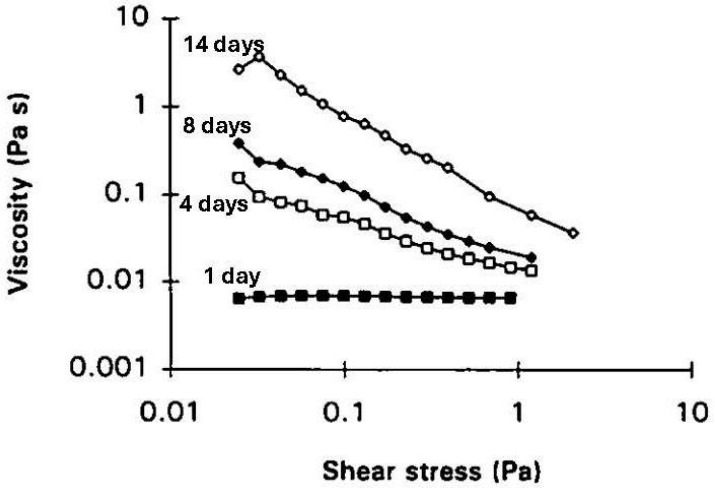

Figure 82. Effect of emulsion aging on the viscosity of caseinate-stabilized emulsion (35 vol% n-tetradecane, pH 6.8, 30 °C, 1 wt% protein). Upon aging, the emulsion droplets undergo bridging flocculation by protein adsorption. Adapted from [68].

8. Dynamic Rheology of Non-Dilute Emulsions

The linear viscoelastic behavior of emulsions has been studied theoretically by Oldroyd [3] and Palierne [71]. The complex shear modulus G^* of a dilute emulsion of identical droplets is given by the following expression derived by Palierne [71]:

$$G^* = G_c^* \ (1 + 5\varphi H^*) \tag{94}$$

where G_c^* is the complex shear modulus of the continuous phase (matrix) and H^* is given by:

$$H^* = \frac{(G_d^* - G_c^*)\ (16\ G_c^* + 19\ G_d^*) + (4\ \gamma/R)\ (2G_c^* + 5G_d^*)}{(2G_d^* + 3G_c^*)\ (16\ G_c^* + 19\ G_d^*) + (40\ \gamma/R)(G_c^* + G_d^*)} \tag{95}$$

In Equation (95), G_d^* is the complex shear modulus of droplets, and γ is the interfacial tension. Note that $G^* = G' + jG''$, where G' is storage modulus, G'' is loss modulus, and j is $\sqrt{-1}$.

The Palierne equation (Equation (94)) is applicable to infinitely dilute emulsions. It cannot be applied at finite concentrations of droplets as the hydrodynamic interaction between the droplets is ignored in its derivation. To consider the hydrodynamic interaction between the droplets, Palierne extended the dilute emulsion equation (Equation (94)) using a self-consistent treatment like the Lorentz sphere method in electricity. The complex shear modulus equation for non-dilute emulsions developed by Palierne is given as:

$$G^* = G_c^* \left(\frac{1+3\varphi H^*}{1-2\varphi H^*}\right) \tag{96}$$

where H^* is given by Equation (95).

The Palierne model, Equation (96), could be re-written in terms of storage and loss moduli as:

$$G' = G_c' M' - G_c'' M'' \tag{97}$$

$$G'' = G_c' M'' + G_c'' M' \tag{98}$$

where

$$M' = \frac{AC + BD}{[C^2 + D^2]}\ ;\quad M'' = \frac{BC - AD}{[C^2 + D^2]} \tag{99}$$

$$A = 1 + 3\varphi H';\quad B = 3\varphi H'';\quad C = 1 - 2\varphi H';\quad D = -2\varphi H'' \tag{100}$$

$$H' = \frac{g'h' + g''h''}{[(g')^2 + (g'')^2]} \tag{101}$$

 doi:10.20944/preprints202603.0830.v1

$$H'' = \frac{g'h'' - g''h'}{[(g')^2 + (g'')^2]} \quad (102)$$

$$g' = (2G_d' + 3G_c')(19G_d' + 16G_c') - (2G_d'' + 3G_c'')(19G_d'' + 16G_c'') + \left(\frac{40\gamma}{R}\right)(G_d' + G_c') \quad (103)$$

$$g'' = (2G_d' + 3G_c')(19G_d'' + 16G_c'') + (2G_d'' + 3G_c'')(19G_d' + 16G_c') + \left(\frac{40\gamma}{R}\right)(G_d'' + G_c'') \quad (104)$$

$$h' = (G_d' - G_c')(19G_d' + 16G_c') - (G_d'' - G_c'')(19G_d'' + 16G_c'') + \left(\frac{4\gamma}{R}\right)(5G_d' + 2G_c') \quad (105)$$

$$h'' = (G_d' - G_c')(19G_d'' + 16G_c'') + (G_d'' - G_c'')(19G_d' + 16G_c') + \left(\frac{4\gamma}{R}\right)(5G_d'' + 2G_c'') \quad (106)$$

For emulsions of two immiscible Newtonian liquids, the Palierne model, Equation (96), reduces to:

$$G^* = \left(\frac{\eta_0\omega^2}{1+\omega^2\lambda_1^2}\right)(\lambda_1 - \lambda_2) + j\left(\frac{\eta_0\omega}{1+\omega^2\lambda_1^2}\right)(1 + \omega^2\lambda_1\lambda_2) \quad (107)$$

where η_0 is zero-shear viscosity, λ_1 is relaxation time, λ_2 is retardation time, and ω is frequency of oscillation. η_0, λ_1 and λ_2 are given as:

$$\eta_0 = \eta_c\left[\frac{10(1+\lambda)+3\varphi(2+5\lambda)}{10(1+\lambda)-2\varphi(2+5\lambda)}\right] \quad (108)$$

$$\lambda_1 = \left(\frac{R\eta_c}{4\gamma}\right)(19\lambda + 16)\left[\frac{2\lambda+3-2\varphi(\lambda-1)}{10(1+\lambda)-2\varphi(2+5\lambda)}\right] \quad (109)$$

$$\lambda_2 = \left(\frac{R\eta_c}{4\gamma}\right)(19\lambda + 16)\left[\frac{2\lambda+3+3\varphi(\lambda-1)}{10(1+\lambda)+3\varphi(2+5\lambda)}\right] \quad (110)$$

Figure 83 shows the storage and loss moduli and Cole-Cole plots of non-dilute emulsion ($\varphi = 0.50$) generated from the Palierne model (Equation (107)) for different values of interfacial stress γ/R. The viscosity ratio λ is fixed at 1 and the continuous phase viscosity η_c is 1Pa.s. The plateau storage modulus at high frequencies increases with the increase in interfacial stress γ/R. The interfacial stress has negligible effect on the Cole-Cole diagram. The Cole-Cole diagram exhibits a single frequency domain as indicated by a single arc due to relaxation of the shape of droplets.

 doi:10.20944/preprints202603.0830.v1

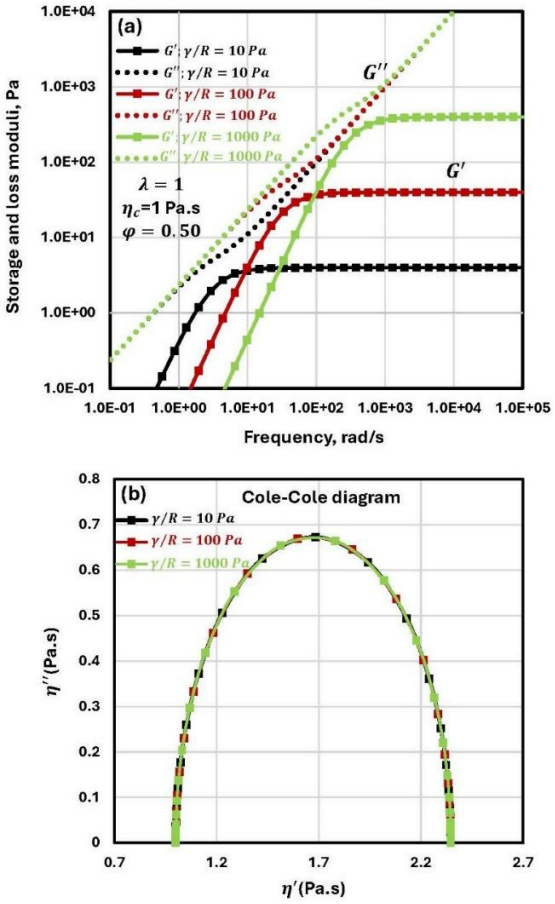

Figure 83. Moduli and Cole-Cole plots of non-dilute emulsion ($\varphi = 0.50$) generated from the Palierne model (Equation (107)) for different values of interfacial stress γ/R.

Figure 84 shows the storage and loss moduli and Cole-Cole plots of non-dilute emulsion ($\varphi = 0.50$) generated from the Palierne model (Equation (107)) for different values of λ. The interfacial stress γ/R is fixed at 100 Pa and the η_c is 1Pa.s. The plateau storage modulus at high frequencies decreases with the increase in λ. The Cole-Cole diagram shifts to higher dynamic viscosities η' with the increase in λ.

 doi:10.20944/preprints202603.0830.v1

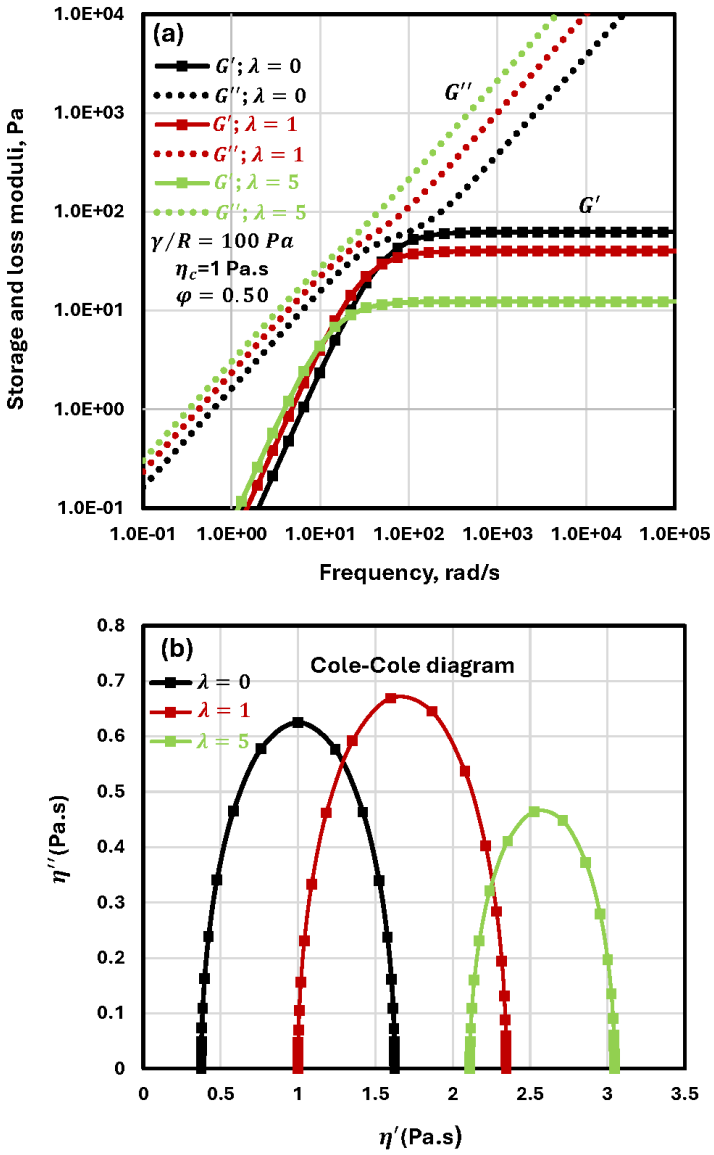

Figure 84. Moduli and Cole-Cole plots of non-dilute emulsion ($\varphi = 0.50$) generated from the Palierne model (Equation (107)) for different values of λ.

Figure 85 shows comparison of theoretical predictions (Palierne model, Equation (96)) with experimental data of storage and loss moduli for non-dilute emulsions [72]. The continuous-phase of the emulsions was 0.82 wt% polymer (Praestol 2540 TR) solutions containing 0.5 wt% Triton X-100 as a surfactant. The dispersed phase (droplets) was a Newtonian petroleum oil of viscosity 5.8 mPa.s at 25 °C. Emulsions were prepared at three oil fractions: $\varphi =$ 0.20, 0.35, and 0.51. While the predictions of the Palierne model are in good agreement with the experimental data at $\varphi =$ 0.20, the model severely underpredicts the moduli values at higher values of φ.

 doi:10.20944/preprints202603.0830.v1

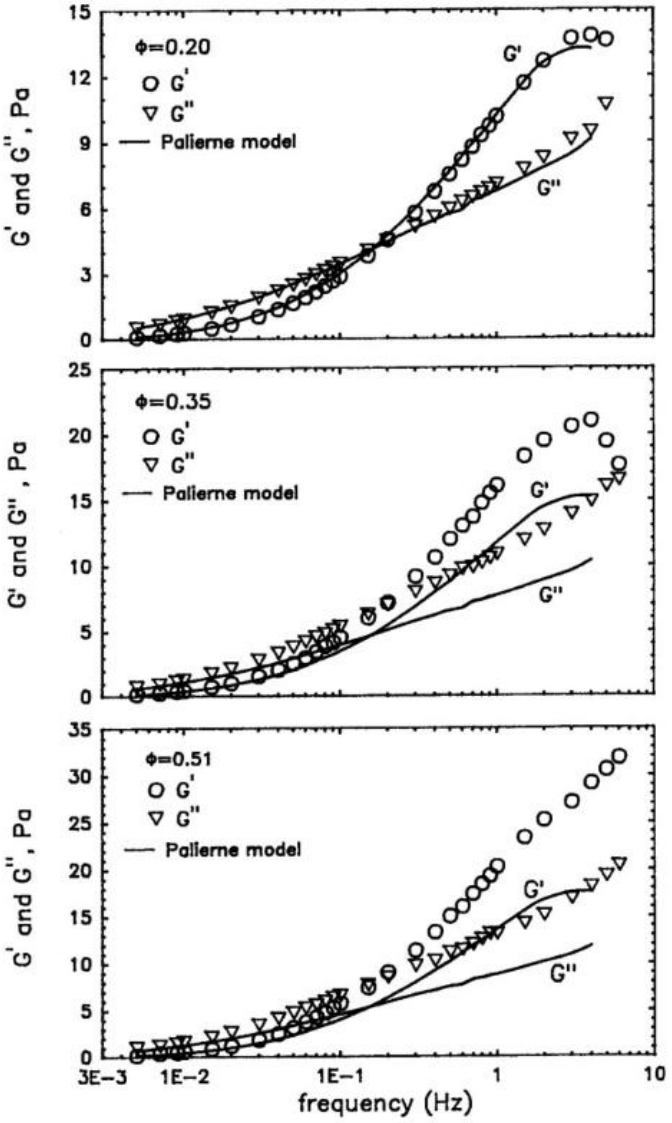

Figure 85. Comparisons between theoretical predictions (Palierne model, Eq. (96)) and data of storage and loss moduli of non-dilute O/W emulsions.

Figure 86 shows comparison of theoretical predictions (Palierne model, Equation (96)) with experimental data of storage and loss moduli for non-dilute suspensions of solid particles [72]. The continuous-phase of the emulsions was 1.02 wt% polymer (Cellulose gum) solutions containing 2 wt% Triton X-100 as a surfactant. The dispersed phase (particles) was glass beads with Sauter mean diameter of 46 μm. The suspensions were prepared at four volume fractions of glass beads: $\varphi =$ 0.176, 0.289, 0.377, and 0.449. Once again, the Palierne model gives good predictions at a low φ of 0.176. The model severely underpredicts the moduli values at higher values of φ.

 doi:10.20944/preprints202603.0830.v1

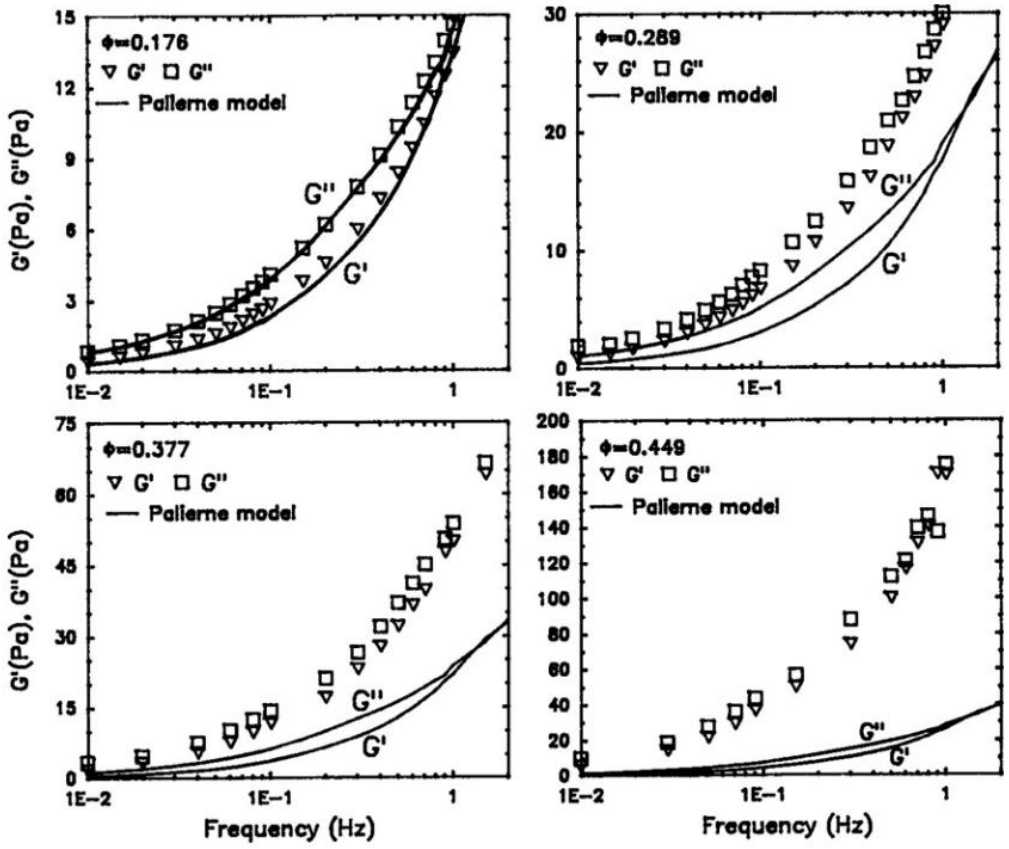

Figure 86. Comparisons between theoretical predictions (Palierne model, Equation (96)) and experimental data of storage and loss moduli of non-dilute suspensions.

The drawbacks of the Palierne model are as follows: 1) it generally underestimates the values of storage and loss moduli at high concentrations of dispersed phase as observed in Figures 85 and 86; 2) it allows the φ of particles/droplets to reach a value of unity. This is physically unrealistic. It may be possible for the volume fraction of particles to reach a value of unity only under the special case where the particle size distribution of the dispersion is extremely wide. Generally, the φ_{max} is much less than unity. For example, $\varphi_{max} \approx 0.64$ for random close packing of uniform spheres; and 3) it fails to exhibit the divergence of storage modulus at $\varphi = \varphi_{max}$, especially when the dispersed phase consists of solid particles. Thus, the Palierne model does not adequately consider the crowding effect of particles and droplets.

To overcome the limitations of the Palierne model, Pal [73] derived new complex shear modulus equations for emulsions using the differential scheme and taking into consideration the crowding effect of droplets. His models are as follows:

$$\left(\frac{G^*}{G_c^*}\right)^2 \left(\frac{M^* - P^* + 32G^*}{M^* - P^* + 32G_c^*}\right)^{N^*-2.5} \left(\frac{M^* + P^* - 32G_c^*}{M^* + P^* - 32G^*}\right)^{N^*+2.5} = exp\left(\frac{5\varphi}{1 - \frac{\varphi}{\varphi_{max}}}\right) \quad (111)$$

where

$$M^* = \sqrt{64(\gamma/R)^2 + 1225G_d^{*2} + 1232(\gamma/R)G_d^*} \quad (112)$$

$$P^* = 8(\gamma/R) - 3G_d^* \quad (113)$$

$$N^* = [44(\gamma/R) + 87.5G_d^*]/M^* \quad (114)$$

 doi:10.20944/preprints202603.0830.v1

Equation (111) reduces to the following equation for suspension of solid spherical particles without interfacial tension:

$$\left(\frac{G^*}{G_c^*}\right)\left(\frac{G^*-G_d^*}{G_c^*-G_d^*}\right)^{-2.5}=exp\left(\frac{2.5\varphi}{1-\frac{\varphi}{\varphi_{max}}}\right)$$

(115)

For rigid spheres $G_d^* \to \infty$, and therefore, Equation (115) further simplifies to:

$$G^*=G_c^*\,exp\left(\frac{2.5\varphi}{1-\frac{\varphi}{\varphi_{max}}}\right)$$

(116)

Another model developed by Pal [73] for the complex shear modulus of emulsions using the differential scheme and taking into consideration the crowding effect of droplets is as follows:

$$\left(\frac{G^*}{G_c^*}\right)^2\left(\frac{M^*-P^*+32G^*}{M^*-P^*+32G_c^*}\right)^{N^*-2.5}\left(\frac{M^*+P^*-32G_c^*}{M^*+P^*-32G^*}\right)^{N^*+2.5}=\left(1-\frac{\varphi}{\varphi_{max}}\right)^{-5\varphi_m}$$

(117)

Equation (116) reduces to the following equation for suspension of solid spherical particles without interfacial tension:

$$\left(\frac{G^*}{G_c^*}\right)\left(\frac{G^*-G_d^*}{G_c^*-G_d^*}\right)^{-2.5}=\left(1-\frac{\varphi}{\varphi_{max}}\right)^{-2.5\varphi_m}$$

(118)

For rigid spheres, Equation (118) simplifies to:

$$G^*=G_c^*\left(1-\frac{\varphi}{\varphi_{max}}\right)^{-2.5\varphi_m}$$

(119)

Figure 87 compares the predictions of the Pal model, Equation (116), with the experimental data ($G^*$and phase lag angle δ) for solids-in-liquid suspensions prepared with spherical glass beads [90]. The Sauter mean diameter of the particles was 92 μm. The dispersion medium was 1.02 wt% cellulose gum. The volume fraction of solids was varied from 0.176 to 0.449. The predictions of the Pal model are in good agreement with the experimental values of complex shear modulus $G^*$and phase lag angle δ for suspensions. The φ_{max} value used in the model was 0.74.

Figure 88 shows comparisons between the predictions of the Pal model, Equation (119), with the experimental data ($G^*$and phase lag angle δ) for solids-in-liquid suspensions prepared with spherical glass beads (Sauter mean diameter of 92 μm) and considered in Figure 87 [74]. The predictions of the Pal model are in good agreement with the experimental values of complex shear modulus $G^*$and phase lag angle δ for suspensions. However, the φ_{max} value used in the model is now 0.50.

While Equation (116) gives a high φ_{max} value of 0.74, Equation (119) gives a significantly lower value of $\varphi_{max}=0.50$.

 doi:10.20944/preprints202603.0830.v1

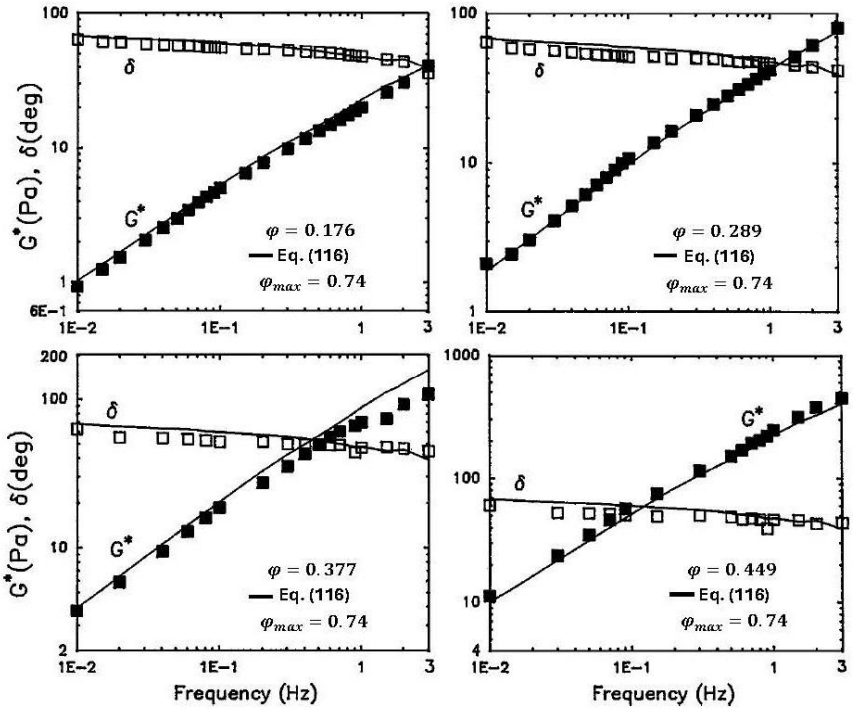

Figure 87. Comparisons between theoretical predictions (Pal model, Equation (116)) and experimental data of G^* and δ of non-dilute suspensions.

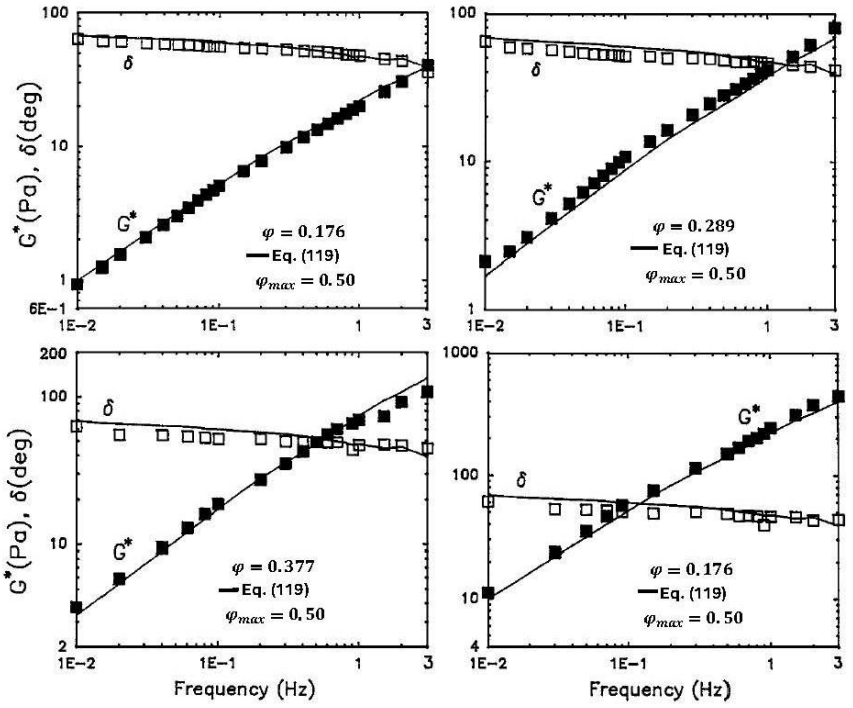

Figure 88. Comparisons between theoretical predictions (Pal model, Equation (119)) and experimental data of G^* and δ of non-dilute suspensions.

The Pal models, Equations (111) and (117), overcome the limitations of the Palierne model, Equation (96) in that the crowding effect of particles/droplets is accounted for adequately. However, the Pal models are not explicit in complex modulus of emulsion G^*. Furthermore, they are not easy to solve to predict the moduli of emulsions. The equations are too complicated and highly nonlinear with no analytical solutions possible.

 doi:10.20944/preprints202603.0830.v1

A new modified form of the Palierne model, Equation (96), was also proposed by Pal [72] to accurately describe the linear viscoelastic behavior of non-dilute emulsions and suspensions. The proposed model takes into consideration the crowding effect and packing limit of particles by replacing the actual φ in the Palierne model (Equation (96)) by the effective φ given as $\psi\varphi$, where $\psi\varphi$ is required to obey the following boundary conditions: $\psi\varphi \to 1$ at $\varphi = \varphi_{max}$, $\psi\varphi \to 0$ at $\varphi = 0$, and $\frac{d(\psi\varphi)}{d\varphi} = 1$ at $\varphi = 0$. Thus, the modified Palierne model proposed by Pal [72] is as follows:

$$G^* = G_c^* \left(\frac{1+3\psi\varphi H^*}{1-2\psi\varphi H^*}\right) \tag{120}$$

One simple expression for $\psi\varphi$ that obeys the just-stated boundary conditions is [72]:

$$\psi\varphi = 1 - exp\left[\frac{-\varphi}{1-(\varphi/\varphi_{max})}\right] \tag{121}$$

The predictions of the modified Palierne model, Equation (120) in conjunction with Equation (121), are compared with data in Figures 89 and 90. As can be seen, the modified Palierne model describes the data of emulsions and suspensions adequately. The φ_{max} value used in the model predictions is 0.57 [72].

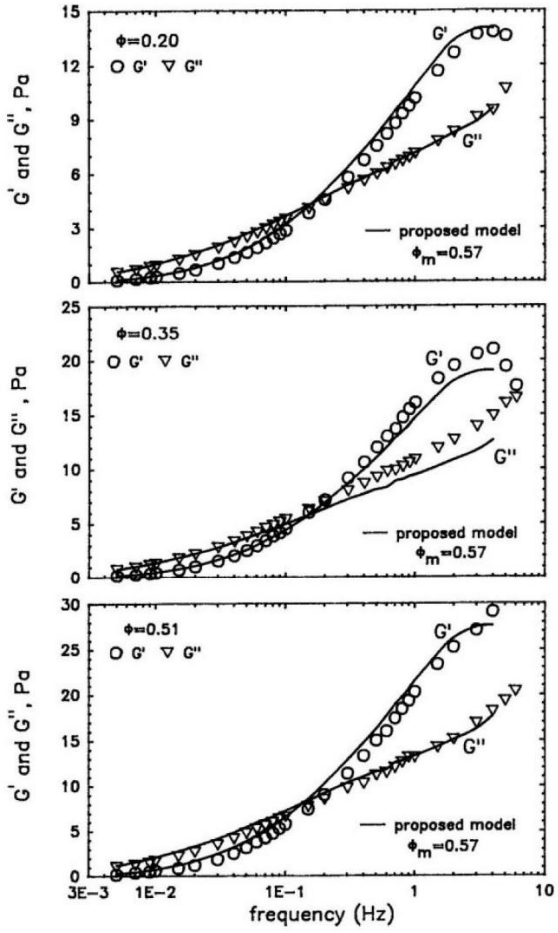

Figure 89. Comparisons between theoretical predictions (modified Palierne model, Equation (120)) and data of storage and loss moduli of non-dilute O/W emulsions.

 doi:10.20944/preprints202603.0830.v1

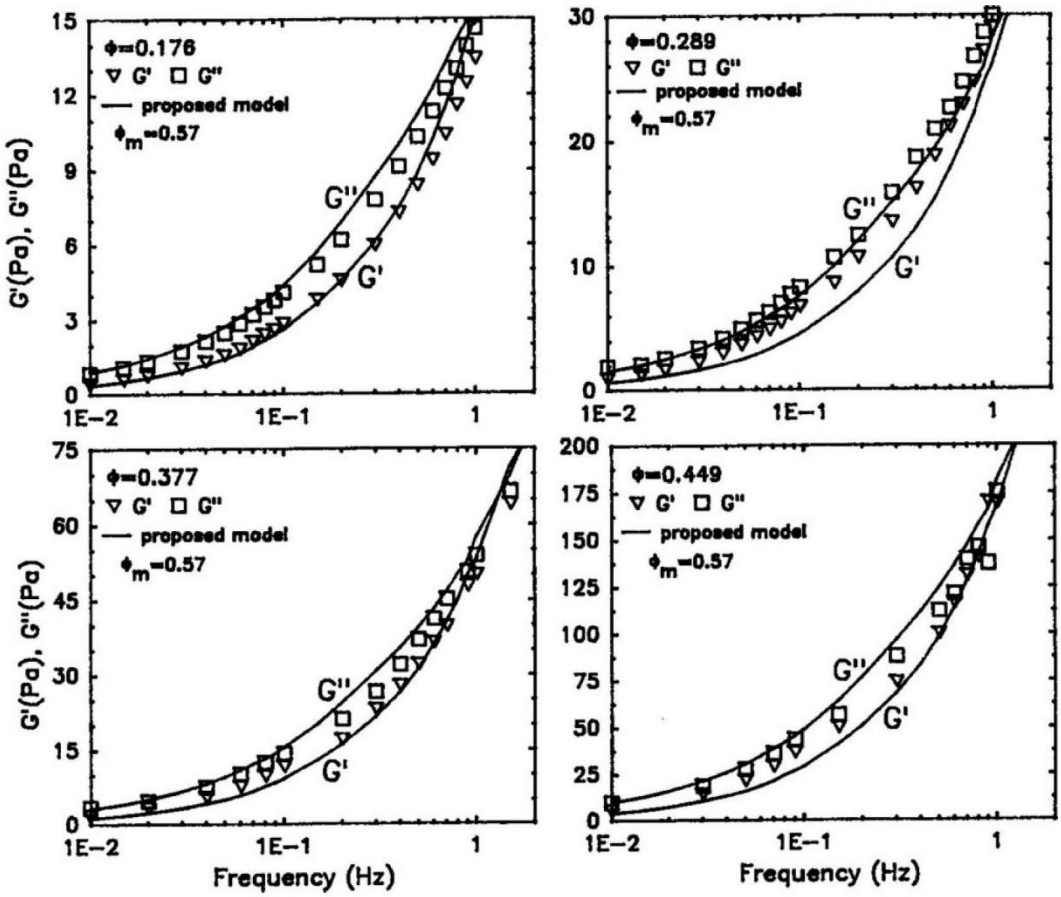

Figure 90. Comparisons between theoretical predictions (modified Palierne model, Equation (120)) and data of storage and loss moduli of non-dilute suspensions.

Thus far, we have considered dynamic rheology of emulsions with pure oil-water interfaces characterized by a uniform interfacial tension. In the presence of additives (surfactants, polymers, etc.) on the oil-water interfaces, the interface itself becomes viscoelastic in nature. The viscoelastic interface is characterized by complex surface-shear modulus G_s^* and complex surface-dilational K_s^* modulus defined as [29]:

$$G_s^* = G_s + j\eta_s\omega \tag{122}$$

$$K_s^* = K_s + j\eta_s^k\omega \tag{123}$$

where G_s , η_s , K_s and η_s^k are surface-shear modulus, surface-shear viscosity, surface-dilational modulus, and surface-dilational viscosity, respectively.

The linear viscoelastic behavior of emulsions with viscoelastic interfaces can be described by the generalized Palierne model, Equation (96) with H^* defined as [71]:

$$H^* = H' + jH'' = \frac{F^*}{D^*} \tag{124}$$

where F^* and D^* are given as:

$$F^* = F' + jF'' = [(G_d^* - G_c^*)\ (19G_d^* + 16G_c^*)] + [24\gamma K_s^*/R^2] + [16G_s^*(\gamma + K_s^*)/R^2] + [(4\gamma/R)\ (5G_d^* + 2G_c^*)] + [(K_s^*/R)(23G_d^* - 16G_c^*)] + [(2G_s^*/R)(13G_d^* + 8G_c^*)] \tag{125}$$

$$D^* = D' + jD'' = [(2G_d^* + 3G_c^*)\ (19G_d^* + 16G_c^*)] + [(40\gamma/R)(G_d^* + G_c^*)] + \left[\frac{2K_s^*}{R}(23G_d^* + 32G_c^*)\right] + \left[\frac{4G_s^*}{R}(13G_d^* + 12G_c^*)\right] + [48K_s^*\gamma/R^2] + [32G_s^*\ (\gamma + K_s^*)/R^2] \tag{126}$$

Thus, the storage and loss moduli of emulsions with viscoelastic interfaces can be calculated from Equations (97)-(100) using the following expressions for H' and H'':

 doi:10.20944/preprints202603.0830.v1

$$H' = \frac{D'F'+D''F''}{[(D')^2+(D'')^2]} \quad (127)$$

$$H'' = \frac{D'F''-D''F'}{[(D')^2+(D'')^2]} \quad (128)$$

where

$$F' = G_d'(19G_d' + 16G_c') - G_d''(19G_d'' + 16G_c'') - G_c'(19G_d' + 16G_c') + G_c''(19G_d'' + 16G_c'') + 24\gamma K_s/R^2 + \frac{16G_s(\gamma+K_s)}{R^2} - \frac{16}{R^2}(\eta_s\eta_s^k\omega^2) + \left(\frac{4\gamma}{R}\right)(5G_d' + 2G_c') + \left(\frac{K_s}{R}\right)(23G_d' - 16G_c') - \frac{\eta_s^k\omega}{R}(23G_d'' - 16G_c'') + \left(\frac{2G_s}{R}\right)(13G_d' + 8G_c') - \frac{2\eta_s\omega}{R}(13G_d'' + 8G_c'') \quad (129)$$

$$F'' = G_d''(19G_d' + 16G_c') + G_d'(19G_d'' + 16G_c'') - G_c''(19G_d' + 16G_c') - G_c'(19G_d'' + 16G_c'') + (24\gamma/R^2)\eta_s^k\omega + \frac{16G_s\eta_s^k\omega}{R^2} + \frac{16}{R^2}(\eta_s\omega)(+K_s) + \left(\frac{4\gamma}{R}\right)(5G_d'' + 2G_c'') + \left(\frac{K_s}{R}\right)(23G_d'' - 16G_c'') + \frac{\eta_s^k\omega}{R}(23G_d' - 16G_c') + \left(\frac{2G_s}{R}\right)(13G_d'' + 8G_c'') + \frac{2\eta_s\omega}{R}(13G_d' + 8G_c') \quad (130)$$

$$D' = (2G_d' + 3G_c')(19G_d' + 16G_c') - (2G_d'' + 3G_c'')(19G_d'' + 16G_c'') + \left(\frac{40\gamma}{R}\right)(G_d' + G_c') + \left(\frac{4G_s}{R}\right)(13G_d' + 12G_c') + \left(\frac{2K_s}{R}\right)(23G_d' + 32G_c') - \frac{2\eta_s^k\omega}{R}(23G_d'' + 32G_c'') - \frac{4\eta_s^k\omega}{R}(13G_d'' + 12G_c'') + \left(\frac{48\gamma K_s}{R^2}\right) + 32G_s\left(\frac{\gamma+K_s}{R^2}\right) - \frac{32\eta_s\eta_s^k\omega^2}{R^2} \quad (131)$$

$$D'' = (2G_d' + 3G_c')(19G_d'' + 16G_c'') + (2G_d'' + 3G_c'')(19G_d' + 16G_c') + \left(\frac{40\gamma}{R}\right)(G_d'' + G_c'') + \left(\frac{4G_s}{R}\right)(13G_d'' + 12G_c'') + \left(\frac{2K_s}{R}\right)(23G_d'' + 32G_c'') + \frac{2\eta_s^k\omega}{R}(23G_d' + 32G_c') + \frac{4\eta_s\omega}{R}(13G_d' + 12G_c') + \frac{48\gamma\eta_s^k\omega}{R^2} + 32G_s\left(\frac{\eta_s^k\omega}{R^2}\right) + \frac{32\eta_s\omega(\gamma+K_s)}{R^2} \quad (132)$$

As an example, Figure 91 shows the dynamic rheological behavior of non-dilute emulsion ($\varphi = 0.5$) with viscoelastic oil-water interfaces. The unique feature of emulsions with viscoelastic interfaces is that they exhibit two frequency domains corresponding to two plateaus in storage modulus and two arcs in Cole-Cole diagram. The right-hand side arc of the Cole-Cole plot corresponds to low frequency behavior, and the left-hand side arc corresponds to high frequency behavior. The low frequency domain reflects elastic behavior due to interfacial relaxation whereas the high frequency domain reflects elastic behavior due to shape relaxation of droplets.

 doi:10.20944/preprints202603.0830.v1

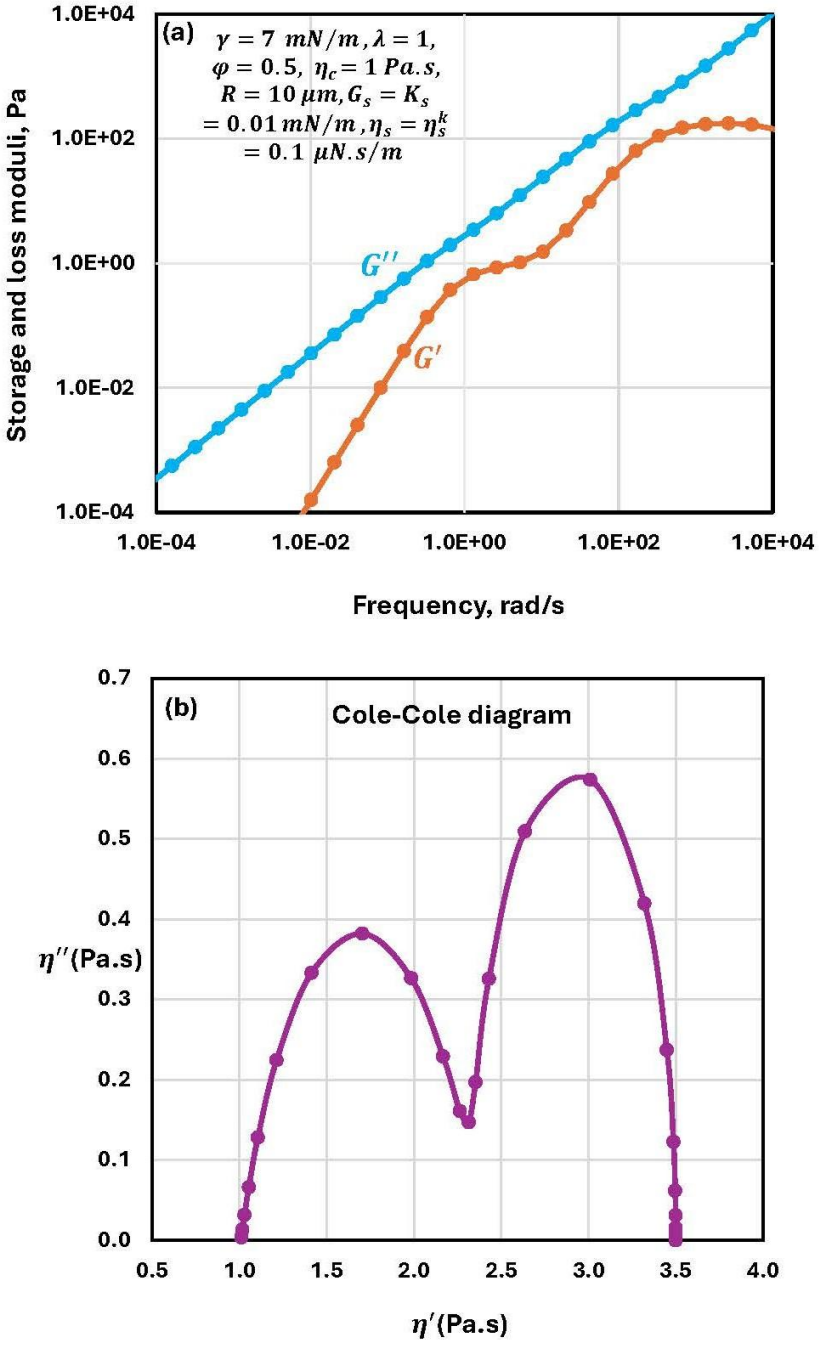

Figure 91. Dynamic rheology of emulsion with viscoelastic oil-water interfaces. The plots are generated from the generalized Palierne model.

9. Concluding Remarks

Although our current understanding of non-dilute emulsion rheology is good, there are still some serious gaps in the existing knowledge.

- Rigorous theories to model the rheological behavior of non-dilute emulsions are lacking. Only approximate techniques such as cell models, self-consistent and effective medium approaches are often utilized to model the rheology of non-dilute emulsions.
- There are hardly any experimental studies available on the effect of deformation (that is, capillary number) on the rheology of non-dilute emulsions.

 doi:10.20944/preprints202603.0830.v1

- Non-hydrodynamic forces such as electrostatic, steric, van der Waals, and Brownian forces are often ignored in the modelling of the rheology of non-dilute emulsions. Non-hydrodynamic forces are particularly important in nano emulsions.
- Experimental studies on non-dilute emulsions dominated by non-hydrodynamic forces are lacking. This is especially the case for nano emulsions.
- Experimental and theoretical studies on the influence of interfacial rheology on the steady shear and viscoelastic behaviors of non-dilute emulsions are scarce.
- The influence of additives such as surfactant micelles, adsorbing and non-adsorbing polymers, on the rheology of non-dilute emulsions has received little attention. In such emulsions, depletion and bridging flocculation of droplets can play an important role in governing the emulsion rheology.
- There is little experimental data available on the viscoelastic behavior of emulsions under the application of steady shear. For example, the generation of normal stresses in the steady shear flow of emulsions is often not considered. Emulsions can exhibit a rich viscoelastic behavior under steady shear especially when the droplet-droplet interactions are strong, attractive or repulsive.

Funding: This research was funded by NSERC Discovery grant awarded to R.P.

Data Availability Statement: The raw data supporting the conclusions of this article will be made available by the author on request.

Conflicts of Interest: The author declares no conflicts of interest.

References

1. Pal, R. Rheology of high internal phase ratio emulsions and foams. *Adv Colloid Interface Sci* **2025,** *339*,103426.
2. Taylor, G.I. The viscosity of a fluid containing small drops of another fluid. *Proc. Roy. Soc. A* **1932,** *138*, 41-48.
3. Oldroyd, J. G. The Elastic and Viscous Properties of Emulsions and Suspensions. *Proc. R. Soc. A* **1953**, *218*, 122.
4. Yaron, I.; Gal-Or, B. On Viscous Flow and Effective Viscosity of Concentrated Suspensions and Emulsions. *Rheol. Acta* **1972**, *11*,241.
5. Choi, S.J. Schowalter WR. Rheological properties of nondilute suspensions of deformable particles. *Phys Fluids* **1975**, *18*, 420–427.
6. Phan-Thien, N.; Pham, D. C. Differential Multiphase Models for Polydispersed Suspensions and Particulate Solids. *J. Non-Newtonian Fluid Mech.* **1997**, *72*, 305.
7. Pal, R. Shear viscosity behavior of emulsions of two immiscible liquids. *J. Colloid Interface Sci*. **2000**, *225*,359-366.
8. Pal, R. Viscosity-concentration equation for emulsions of nearly spherical droplets. *J. Colloid Interface Sci.* **2000**, *231*,168-175.
9. Brinkman, H. C. The Viscosity of Concentrated Suspensions and Solutions. *J. Chem. Phys.* **1952**, *20*, 571.
10. Roscoe, R. The Viscosity of Suspensions of Rigid Spheres. *Br. J. Appl. Phys.* **1952**, *3*, 267
11. Pal, R. Novel viscosity equations for emulsions of two immiscible liquids. *J. Rheol.* **2001**, *45*,509-520.
12. Mooney, M. The viscosity of a concentrated suspension of spherical particles. *J. Colloid Sci.* **1951**, *6*, 162-170.
13. Krieger, I.M; Dougherty, T.J. Mechanism for non-Newtonian flow in suspensions of rigid particles. *Trans. Soc. Rheol.* **1959**, *3*,137-152.
14. Pal, R. Single-parameter and two-parameter rheological equations of state for non-dilute emulsions. *Ind. Eng. Chem. Res.* **2001**,*40*, 5666-5674.
15. Mendoza, C.I.; Santamaria-Holek, I. The rheology of hard sphere suspensions at arbitrary volume fractions: An improved differential viscosity model. *J. Chem. Phys.* **2009**, *130*, 044904
16. Pal, R. Recent developments in the viscosity modeling of concentrated monodisperse emulsions. *Foods* **2023**, *12*, 3483.
17. Tanner, R.I. Review article: Aspects of non-colloidal suspension rheology. *Phys. Fluids* **2018**, *30*, 101301.

 doi:10.20944/preprints202603.0830.v1

18. Pal, R. Recent progress in the viscosity modeling of concentrated suspensions of unimodal hard spheres. *ChemEngineering* **2023**, *7*, 70.
19. Pal, R. New generalized viscosity model for non-colloidal suspensions and emulsions. *Fluids* **2020**, *5*,150.
20. Pal, R. Relative viscosity of non-Newtonian concentrated emulsions of noncolloidal droplets. *Ind. Eng. Chem. Res*. **2000**, *39*, 4933-4943.
21. Pal, R. Effect of droplet size on the rheology of emulsions. *AIChE J.* **1996**, *42*, 3181-3190.
22. Chen, Y., and Conrad, H., *ASME FED* **1999**, *249*, 105.
23. Ouchiyama, N.; Tanaka, T. Porosity estimation for random packings of spherical particles. *Ind. Eng. Chem. Fundam*. **1984**, *23*, 490.
24. Pal, R. Scaling of relative viscosity of emulsions. *J. Rheol.* **1997**, *41*, 141-150.
25. Graham, A. L.; Bird, R.B. Particle clusters in concentrated suspensions. 1. Experimental observations of particle clusters. *Ind. Eng. Chem. Fundam.* **1984**, *23*, 406–410.
26. Graham, A. L., Steele, R.D.; Bird, R.B. Particle clusters in concentrated suspensions. 3. Prediction of suspension viscosity.*Ind. Eng. Chem. Fundam. 23*, 420–425.
27. Pal, R. Non-Newtonian behaviour of suspensions and emulsions: Review of different mechanisms. *Adv Colloid Interface Sci* **2024**, *333*,103299.
28. Pal R. A novel method to correlate emulsion viscosity data. *Colloids and Surfaces A* **1998**, *137*, 275-286.
29. Pal, R. Rheology of Particulate Dispersions and Composites. CRC Press, Boca Raton, USA, 2007.
30. Schowalter, W.R.; Chaffey, C.E.; Brenner, H. Rheological behavior of a dilute emulsion. *J Colloid Interface Sci* **1968**, *26*, 152–160.
31. Frankel, N.A.; Acrivos, A. The constitutive equation for a dilute emulsion. *J Fluid Mech* **1970**, *44*, 65–78.
32. Barthes-Biesel, D.; Acrivos, A. The rheology of suspensions and its relation to phenomenological theories for non-Newtonian fluids. *Int J Multiph Flow* **1973**, *1*, 1–24.
33. Pal, R. Viscous behavior of concentrated emulsions of two immiscible Newtonian fluids with interfacial tension. *J. Colloid Interface Sci* **2003**, *263*, 296-305.
34. Oldroyd, J. G. The effect of interfacial stabilizing films on the elastic and viscous properties of emulsions. *Proc. R. Soc. A* **1955**, *232*, 567-577.
35. Danov, K.D. On the viscosity of dilute emulsions. *J. Colloid Int. Sci.* **2001**, *235*,144-149.
36. Pal, R. Influence of interfacial rheology on the viscosity of concentrated emulsions. *J. Colloid Interface Sci.* **2011**, *356*,118-122.
37. Pal, R. Fundamental rheology of disperse systems based on single-particle dynamics. *Fluids* **2016**, *1*,40.
38. Van der Waarden, M. Viscosity and electroviscous effect of emulsions. *J. Colloid Sci.* **1954**, *9*, 215-222.
39. Russel, W.B. The rheology of suspensions of charged rigid spheres. *J. Fluid Mech* **1978**, *85*, 209–232.
40. Russel, W.B. Bulk stresses due to deformation of the electrical double layer around a charged sphere. *J Fluid Mech* **1978**, *85*, 673–683.
41. Watterson, I.G.; White, L.R. Primary electroviscous effect in suspensions of charged spherical particles. *J Chem Soc Faraday Trans* **1981**, *77*, 1115–1128.
42. Rubio-Hernandez, F.J.; Carrique, F.; Ruiz-Reina, E. The primary electroviscous effect in colloidal suspensions. *Adv Colloid Interface Sci* **2004**, *107*, 51–60
43. Ohshima, H. Primary electroviscous effect in a dilute suspension of charged mercury drops. *Langmuir* **2006**, *22*, 2863–2869.
44. Ohshima, H. Primary electroviscous effect in a moderately concentrated suspension of charged spherical particles. *Langmuir* **2007**, *23*, 12061–12066
45. Chan, F.S.; Blachford, J.; Goring, D.A.I. The secondary electroviscous effect in a charged spherical colloid. *J Colloid Interface Sci* **1966**, *22*, 378-385.
46. Kundu, P.; Kumar, V.; Mishra, I.M. Study the electro-viscous effect on stability and rheological behavior of surfactant-stabilized emulsions. *J. Dispersion Sci Tech* **2018**, *39*, 384-394.
47. Wu, B.; Iwashita, T.; Chen, W.R. Scaling of shear rheology of concentrated charged colloidal suspensions across glass transition. *J Phys Chem B* **2022**, *126*, 922-927.
48. Krieger, I.M.; Eguiluz, M. The second electroviscous effect in polymer latices. *Trans Soc Rheol* **1976**, *20*, 29-45.

 doi:10.20944/preprints202603.0830.v1

49. Boersma, W.H.; Laven, J.; Stein, H.N. Viscoelastic Properties of Concentrated Shear-Thickening Dispersions. *J Colloid Interface Sci* **1992**, *149*,10-22.
50. Brown, E.; Forman, N.A.; Orellana, C.S.; Zhang, H.; Maynor, B.W.; Betts, D.E.; DeSimone J.M.; Jaeger, H.M. Generality of shear thickening in dense suspensions. *Nature Materials* **2010**, *9*, 220-224.
51. Pal, R. Rheology of emulsions containing polymeric liquids. In Becher, P. (ed) Encyclopedia of emulsion technology, Vol 4, Chapter 3, Marcel Dekker, New York, 1996.
52. Nommensen, P.A.; Duits, M.H.G.; Van den Ende, D.; Mellema, J. Steady shear behavior of polymerically stabilized suspensions: Experiments and lubrication based modeling. *Physical Rev E* **1999**, *59*, 3147-3154.
53. Frith, W.J.; d'Haene, P.; Buscall, R.; Mewis, J. Shear thickening in model suspensions of sterically stabilized particles. *J Rheol* **1996**, *40*, 531-548.
54. Wolf, B.; Lam, S.; Kirkland, M.; Frith, W.J. Shear thickening of an emulsion stabilized with hydrophilic silica particles. *J Rheol* **2007**, *51*, 465-478.
55. Pal, R. A Simple Model for the Viscosity of Pickering Emulsions. *Fluids* **2018**, *3:* 2.
56. Woutersen, A.T.J.M.; de Kruif, C.G. The rheology of adhesive hard sphere dispersions. *J Chem Phys 1991*, **94**, 5739-5750.
57. Russel, W.B. Review of the role of colloidal forces in the rheology of suspension. *J. Rheol.* **1980**, *24*, 287-317.
58. Wiley, S.J.; Macosco, C.W. Steady shear rheological behavior of PVC Plastisols. *J. Rheol.* **1978**, 22, 525-545.
59. Krieger, I.M. Rheology of monodisperse latices. *Adv Colloid Interface Sci* **1972**, *3*, 111-136.
60. Rodriguez, B.E.; Kaler, E.W.; Wolfe, M.S. Binary mixtures of monodisperse latex dispersions. 2. Viscosity. *Langmuir* **1992,** *8*, 2382-2389.
61. Jones, D.A.R.; Leary, B.; Boger, D.V. The rheology of a concentrated colloidal suspension of hard spheres. *J Colloid Interface Sci* **1991**, *147*, 479-495.
62. Aronson, M.P. Flocculation of emulsions by free surfactant in purified systems. *Colloids Surfaces* **1991**, *58*,195–202.
63. Pal. R. Rheological behavior of concentrated surfactant solutions and emulsions. *Colloids Surfaces* **1992**, *64*,207–215.
64. Pal, R. Rheological behavior of surfactant-flocculated water-in-oil emulsions. *Colloids Surfaces* **1993**, *71*,173–185.
65. Pal, R. Dynamics of flocculated emulsions. *Chem Eng Sci* **1997**, *52*, 1177–1187.
66. Jansen, K.M.B.; Agterof, W.G.M.; Mellema, J. Viscosity of surfactant stabilized emulsions. *J Rheol* **2001**, *45*, 1359–1371.
67. Dickinson, E.; Golding, M. Depletion flocculation of emulsions containing unadsorbed sodium caseinate. *Food Hydrocolloids* **1997**, *11*, 13-18.
68. Dickinson, E.; Golding, M. Rheology of sodium caseinate stabilized oil-in-water emulsions. *J. Colloid Interface Sci*. **1997**, *191*, 166-176.
69. Pal, R. Rheology of Blends of Suspensions and Emulsions. *Ind Eng Chem Res* **1999**, *38*,5005-5010.
70. Otsubo, Y. Dilatant flow of flocculated suspensions. *Langmuir* **1992**, *8*,2336–2340.
71. Palierne, J.F. Linear rheology of viscoelastic emulsions with interfacial tension. *Rheol. Acta* **1990**, *29*, 204-214.
72. Pal, R. A new linear viscoelastic model for emulsions and suspensions. *Polym. Eng. Sci.* **2008**, *48*, 1250-1253.
73. Pal, R. Novel shear modulus equations for concentrated emulsions of two immiscible liquids with interfacial tension. *J. Non-Newtonian Fluid Mech.* **2002**, *105*,21-33.
74. Pal, R. Complex shear modulus of concentrated suspensions of solid spherical particles. *J Colloid Interface Sci* **2002**, *245*, 171–177.